THE BULK LUNAR ELECTRICAL CONDUCTIVITY

by

Donald Lucien Leavy

B.Sc., Physics, University of Montreal
(1968)

M.Sc., Earth and Planetary Sciences
Massachusetts Institute of Technology
(1972)

SUBMITTED IN PARTIAL FULFILLMENT OF
THE REQUIREMENTS FOR THE DEGREE OF (DOCTOR OF PHILOSOPHY)
Sc.D.

at the

MASSACHUSETTS INSTITUTE OF TECHNOLOGY

January, 1975

Sugnature of Author____
Department of Earth and Planetary Sciences, January , 1975

Certified by ____
Thesis Supervisor

Accepted by____
Chairman, Departmental Committee on Graduate Students
lgren

Page 111 is missing from the original.

Abstract

The Bulk Lunar Electrical Conductivity

by

Donald Lucien Leavy

Submitted to the Department of Earth and
Planetary Sciences on January 29, 1975
in partial fulfillment of the
requirements for the degree of
(Doctor of Philosophy)
Sc.D.

We study the electrical conductivity structure of a spherically layered moon consistent with the very low frequency magnetic data ($0.0002 \leq f \leq 0.04$ Hz) collected on the lunar surface and by Explorer 35. In order to obtain good agreement with the lunar surface magnetometer observations, the inclusion of a void cavity behind the moon requires a conductivity at shallow depths higher than that of models having the solar wind impinging on all sides. By varying only the source parameters, a conductivity model can be found that yields a good fit to both the tangential response upstream and the radial response downstream. This model also satisfies the dark side tangential response in the frequency range above 0.006 Hz but the few data points presently available below this range do not seem to agree with the theory.

A common feature of models resulting from the inversion of the sunlit side data is that the electrical conductivity profiles hardly increase by one order of magnitude at depths between about 200 and 700 km. Two simple interpretations of this constraint appear mutually exclusive at this point. On one hand, the persistence of a large temperature gradient to moderate depths, in models resulting from conventional thermal history calculations, would seem to require a conduction mechanism characterized by a very low activation energy (0.09 - 0.24 ev) and moderate conductivity prefactor (10^{-3}-10^{-2}mho/m). On the other hand, the conductivity-temperature relationships usually found in silicate minerals would lead to models of temperature with very small gradients at depths greater than about 200 km.

Thesis Supervisor: T. R. Madden

Title: Professor of Geophysics

Acknowledgements

I am especially indebted to my advisor, Professor Theodore Madden, for his numerous contributions to practically all aspects of this thesis. His guidance, based on a vast reservoir of knowledge and a sound physical insight, has insured the steady progress of this investigation.

The problem was initially suggested through helpful discussions the author had with Donald Paul and Colbert Reisz.

The typewritten version of this manuscript is the work of Ms. Judith Ungermann and I am also grateful to her for innumerable improvements in the English quality of the text.

Special thanks are also due to all my friends who have provided a congenial atmosphere during my stay at M.I.T.

During his graduate years, the author has held a Kennecott Copper Fellowship and research assistantships funded by the Advanced Research Project Agency and the Office of Naval Research. The National Aeronautics and Space Administration has funded this work through Grant NGL-22-009-187.

Table of Contents

Chapter IV - Inverse Problem and Conclusion

List of Figures and Tables

Figure Page

Tables Page

Chapter I

Historical Introduction

1.1 Introduction

Two major experiments have been the turning point, in recent years, in our understanding of the moon's electromagnetic environment. On July 22, 1967, the Explorer 35 spacecraft was injected into a stable lunar orbit carrying magnetometers, energetic particle detectors, and plasma probes on board. The results of this experiment were to unravel the essential feature of the interaction of the solar wind with the moon. However, it turned out that no effect of the conductive lunar interior could be detected at the satellite orbit. Such signals were not conclusively obtained until the deployment of the Apollo 12 lunar surface magnetometer (LSM) on November 19, 1969. Since the evolution of our concept has been largely shaped by the data obtained in these two experiments, they provide a natural division in the short history of the subject.

1.2 The Pre-Explorer 35 Period

In order to develop a quantitative theory of the interaction of the solar wind with a planet, it is essential to know the magnitude of the steady, global magnetic field this planet might possess. At the earth's orbit, this field needed only to be of the order of 50 gammas in order to balance the dynamic pressure of the solar wind and thus form a bow shock on the sunlit side of the moon (Willis, 1971).

The results of the early spacecrafts sent to the moon were not entirely conclusive on this question. The Luna 2 probe (Dolginov, 1961) did not observe any perturbation of the interplanetary field at 50 km above the sunlit lunar surface, when the moon was in the magnetosheath. The accuracy of the instrument was about 100 γ, so this experiment did put a fairly accurate upper limit on the global magnetic field that might be present on the lunar surface. However, the possibility that a shock existed was not completely ruled out. A steady dipolar field of about 50 γ presumably would be compressed to within a few plasma skin depths ($\simeq$ 2 km) of the lunar surface and thus be hardly observable at an altitude of 50 km.

The interaction of the solar wind with an electrically conductive lunar interior might also build up the required 50 γ for a shock. Two modes of interaction are possible. In the poloidal H mode, eddy currents are generated inside the moon by the time-varying interplanetary magnetic field. If we consider an homogeneous lunar model, these currents confine the interplanetary magnetic field fluctuation to within a skin depth,

$$\delta = (\frac{2}{\omega\mu_o\sigma})^{1/2}$$

of the lunar surface. Moreover, since the solar wind presumably shields itself from the magnetic field generated by these currents, through confining current flowing within a few plasma skin depths from the lunar surface, an interplanetary fluctuation associated with a lunar skin depth much smaller than the radius of the moon would be amplified roughly by a factor R_M/δ on the lunar surface. If we assume that a shock is produced by the sector structure fluctuation of the interplanetary magnetic field, $B \simeq 5\gamma$, period ≃ 10 days, (Schatten, 1971), then we require a near surface lunar conductivity higher than a few mhos/m ($\delta \lesssim 0.1\ R_M$).

Such high conductivity, typical of sea water on earth, was considered by Gold (1966) in a qualitative analysis of the interaction of the solar wind with the moon. Tozer et al. (1967) quickly pointed out, however, that if water is not present inside the moon, the bulk lunar conductivity is likely to be determined by the temperature and composition at a given depth. Using a temperature model proposed by Urey (1962) and the conductivity-temperature relationship for an olivine with 10% fayalite, they showed that a conductivity of a few mhos/M is likely to be reached only deep inside the moon ($R \simeq 800$ km). They thus dismissed the possibility for the poloidal H mode to produce a detached bow shock in front of the moon. However, apparently omitting the possibility for the magnetic field line to slip around the core, Tozer et al. concluded that the field lines will accrete in front of the core and thus produce an attached hydromagnetic shock near the limb of the optical shadow.

The toroidal H interaction was investigated by Sonett et al. (1967). In the rest frame of the moon, the interplanetary magnetic field, B_{SW}, is seen to be accompanied by an electric field given by

$$\vec{E} = -\vec{V}_{SW} \times \vec{B}_{SW} \tag{1.2.1}$$

An exact determination of the solar wind velocity, $\vec{V}_{SW}$, involves not only the streaming speed of the solar wind ($\simeq 350$ km/sec), but also the various motions of the moon. However, even the most important of these motions, the rotation around the sun together with the earth ($\simeq 29.8$ km/sec), has a magnitude much smaller than the bulk solar wind velocity. Thus these motions will be neglected in the following discussion.

Let us approximate the moon by a cylinder with axis parallel to the $\vec{E}$ field, with radius equal to the moon radius and with length twice this value. The potential across the cylinder is then given by

$$\phi = 2R_M E = 2R_M V_{SW} B_{SW} \tag{1.2.2}$$

where we have assumed the solar wind magnetic field to be perpendicular to the solar wind velocity. Equation (1.2.2) also assumes that the electric conductivity of the solar wind is very high so that no electric field is seen in the rest frame of the wind. By Ohm's Law, we have

$$I = \frac{\phi}{Re} = \frac{\pi R_M}{2} \sigma \phi \tag{1.2.3}$$

where I is the current and Re the resistance along the cylinder axis and σ is the cylinder conductivity. From Ampere's Law, and combining Equations (1.2.2) and (1.2.3) we obtain

$$B_{\text{toroidal}} = \frac{\mu_o I}{2\pi R_M} = \alpha \mu_o \sigma R_M V_{SW} B_{SW} \tag{1.2.4}$$

where for a homogeneous cylinder $\alpha = 0.5$.

We note that, for field fluctuations associated with an interplanetary wavelength and lunar skin depth much larger than the radius of the moon, the toroidal H induction field is independent of frequency. Moreover, if the conductivity is about 3 x 10^{-5} mho/m, the toroidal H field at the lunar surface is nearly ten times the solar wind magnetic field. In that case, a shock might be formed on the sunlit side of the moon. However, even if the interior conductivity of the moon is higher than 10^{-5} mho/m but is covered by an insulating layer, the toroidal H field may become much smaller than the solar wind field. Let us assume our cylinder to be capped by layers of thicknesses Δ and neglect the internal resistance compared to the one at the surface (the resistance to the current flow added in series). Then, the toroidal H field is still given approximately by Equation (1.2.4) but with $\alpha = 0.5\ R_M/\Delta$ and σ equal to the crustal conductivity. A 17 km crust with conductivity 3 x 10^{-7} mho/m still gives a surface field ten times higher than the solar wind field. However, if the conductivity-thickness ratio of the surface layer is a hundred times smaller than 2 x 10^{-8} mho/m-km, then the toroidal H field becomes only one tenth of the solar wind field, at the surface of the moon.

In situ, measurement of rock conductivity at the surface of the earth has not revealed conductivity much lower than 10^{-5} mho/m. But this is due mainly to the presence of water in the earth crust (Madden, 1971, and Brace, 1971). Laboratory measurement on dry rocks have shown, however, that conductivity lower than 10^{-8} mho/m can easily be reached at room temperature (see, for example, Fensler, 1962). Because of the relatively large range of conductivity one might assume for the surface of a planet, predicting the importance of the toroidal H mode will probably remain difficult.

During a month in 1966, the Luna 10 spacecraft was placed in lunar orbit and sent back to earth additional data on the magnetic field around the moon. A very regular field of 23 to 40 γ was observed (Dolginov et al. 1966). This field did not vary much either along an orbit of the satellite around the moon (periselene: 1.2 R_M; aposelene: 1.7 R_M) or along the orbit of the moon around the earth. Though the regular behavior of the field rendered the measurement somewhat suspect, Dolginov et al. (1967) proposed a possible interpretation in terms of the interaction of the solar wind with a conductive lunar interior.

1.3 From Explorer 35 to Apollo 12

Explorer 35 has a stable orbit of period 11.5 hours, aposelene = 5.4 R_M, and periselene = 1.4 R_M. The preliminary results sent back to earth by this spacecraft

(Ness et al., 1967, and Lyon et al., 1967) were to be confirmed by subsequent instruments sent to the moon.

Contrary to what was observed by Luna 10, no steady lunar magnetic field, of magnitude several times the average solar wind field, was found. Behannon (1968) by examining the Explorer 35 data, obtained when the moon traversed the neutral sheet of the geomagnetic tail, was able to distinguish the magnetic field of a possible permanent lunar dipole from the one induced by a bulk lunar permeability. He was thus able to establish an upper limit of 4 γ on the permanent dipole field at the lunar surface and an upper limit of 1.8 for the bulk relative magnetic permeability of the moon.

No bow shock wave was observed. As we have seen above, a possible explanation for the absence of a toroidal H mode-induced shock is the presence of a surface layer of conductivity thickness ratio smaller than 2×10^{-8} mho/m - km. The fact that the time variation of the interplanetary magnetic field associated with its sector structure does not produce a poloidal H type of shock tends to imply that the conductivity in the top 200 km of the moon is smaller than a few mhos/m.

When the moon is in the solar wind and the satellite passes through a cylinder approximately defined by the optical shadow, several effects of the interaction of the solar wind with the moon were observed. The plasma flux (50 < Ep < 2850 ev) decreased by several orders of magnitude consistent with the hypothesis that the particles in the solar wind were absorbed on the sunlit surface of the moon, leaving a void on its downstream side. The magnetic field was also perturbed (Figure 1.1). Near the boundary of the optical shadow a small decrease in the field magnitude is followed by a gradual increase in the plasma umbra (Colburn _et al._, 1967, and Taylor _et al._, 1968). Several theoretical attempts were made to explain these characteristics. Spreiter _et al._, (1970), using the equations of magnetohydrodynamics, examined the case where the interplanetary magnetic field is aligned with the flow direction. This particular field configuration was reported by Ness _et al._ (1968), and their results agree qualitatively with the observations. They found that the small decrease can be understood in terms of the approximate conservation of the ratio of magnetic field to particle density along a streamline. The solar wind particles initially tend to fill the void thus decreasing particle density, pressure and magnetic field along a streamline. These gradients are accompanied by current that increases the field of the plasma umbra. An equilibrium void/plasma boundary is reached when the umbral magnetic pressure balances the particle and magnetic pressure of the solar wind. Whang (1970), noting that the scale length associated with the observed field gradient is generally larger than the proton gyroradius (≃ 100 km), used the guiding center approximation to calculate the field and particle distribution. His treatment included the effect of anisotropic propagation of the magnetosonic wave in addition to the more general field configuration.

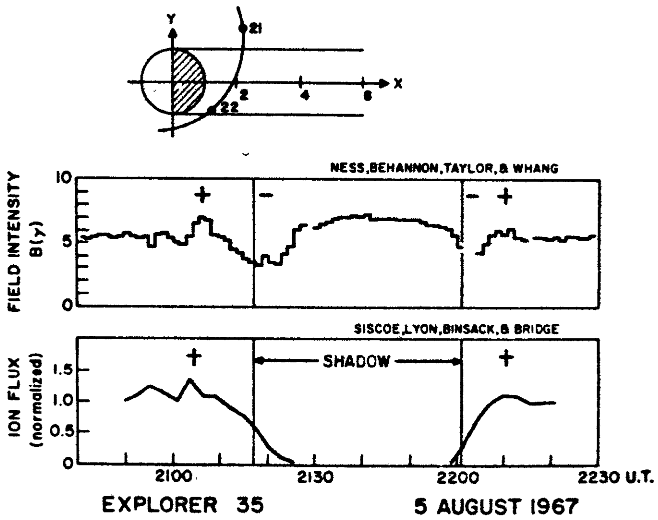

Figure 1.1

Simultaneous measurements of field and plasma obtained on August 5, 1967, from lunar orbit on the Explorer-35 spacecraft. The trajectory of the spacecraft is shown projected on the ecliptic plane and positionally correlated with the data through UT annotation. The *x* axis is parallel to the sun-moon line.

A fundamental aspect of the interaction is the fact that the Alfven and sound speed ($\simeq$ 30 km/sec) are much lower than the bulk solar wind velocity. Consequently, a given position in the solar wind, on the downstream side of the moon, will be influenced by the disturbed condition at the plasma-vacuum boundary only if it is within the Mach forecones originating at the terminator (the limb for solar wind flow). The existence of such Mach cone received some experimental support by Whang et al. (1970). Also, Ogilvie et al. (1970) showed that the amplitude of the umbral increase and penumbral decrease tend to grow in proportion to the ratio of particle to magnetic pressure. However, since, to date, only a subset of the parameter that influences the field characteristics have been compared to the theory, its detailed confirmation must still be considered incomplete.

In addition to the two characteristics just mentioned, a small increase of the magnetic field was often observed on the interplanetary side of the penumbral decrease. This feature was shown to correlate with a small enhancement in particle density (Figure 1.1). (See Siscoe, 1969). Hollweg (1968) suggested that if ice is present near the surface of the moon a significant toroidal H field, might be induced. The interaction of the solar wind with this field would presumably produce the small external increase. However, chemical analysis of lunar samples brought back to earth in the Apollo 11 mission did not show any evidence of hydrous phases in lunar rocks (see, for example, Charles et al., 1971). Schwartz et al., (1969), pointed out, though, that a dry moon, with a hot interior, might also produce a significant toroidal H field, depending on its near-surface conductivity. But Ness (1972), in a review of the subject, argued against this possibility on the basis that the small peak is often observed when the interplanetary magnetic field is aligned with the solar wind flow velocity. According to Equation (1.2.1), no motional electric field should exist in that case.

In view of the absence of bow shock and in anticipation of the lunar surface magnetometer experiment, the response of the moon to time varying magnetic fluctuation was also re-evaluated theoretically by several workers (Blank et al., 1969, Schubert et al., 1969, Schwartz et al., 1960, Sill et al., 1970). They showed that the expected frequency dependence of the poloidal H lunar response might enable us to distinguish between several possible lunar conductivity profiles, in particular between a hot and cold moon based on the conductivity models proposed by England et al. (1968).

The concept that the solar wind interaction with the moon does not perturb regions outside the Mach cones on the downstream side of the moon was found to break down for frequencies higher than approximately 0.1 Hz (Ness et al., 1969). High frequency fluctuations seemed to originate at the plasma vacuum interface and to propagate, outside the plasma umbra, along the time average magnetic field lines threading the lunar wake. A higher level in the power spectral density above about 0.1 Hz was seen to be maintained in a region within approximately one lunar radius of the plasma/void interface. A tentative explanation for this phenomenon was given by Krall et al. (1968) in terms of an electron ballistic effect. They argue that the solar wind electrons (thermal-speed $\simeq$ 2000 km/sec, gyroradius $\simeq$ 2 km), upon reflection at the solar wind/void interface, will carry a memory of the perturbed condition at this boundary. This memory, which manifests itself as a fluctuating magnetic field associated with current produced by a perturbation of the electron distribution function, will eventually fade away by phase mixing as the electrons travel away from the boundary.

1.4 From Apollo 12 to Recent Years

Several magnetometers were flown to the moon during the Apollo missions. One highlight of these experiments was the discovery of local remanent magnetic fields at most Apollo sites (see Table 1.1 from Dyal et al., 1972, 1973 a, b).

Table 1.1

Site	Location	Steady Magnetic Field (γ)
Apollo 12	Oceanus Procellarum (3.2°S 23.4°W)	38±3
Apollo 14	Fra Mauro (3.7°S 17.5°S)	103±5
	(two sites 1.1 km apart)	43±6
Apollo 15	Hadly-Apennines (26.1°N 3.7°E)	6±4
Apollo 16	Descartes (8.9°S 15.5°E)	327
	(five sites separated by 0.5 to 7.1 km)	232
		189
		113
		113

In addition to these instruments, two subsatellites, with magnetometers on board, were launched during the Apollo 15 and 16 missions along orbit near the surface of the moon ($\simeq 100$ km). Data from these subsatellites were used to map the lunar remanent field (Coleman et al., 1972) and also to place an upper limit of 3.6×10^{18} gauss-cm^{3} on the permanent magnetic dipole moment of the moon (Russell et al., 1973). Thus, the permanent lunar magnetic moment is at most 4.5×10^{-8} times as strong as the one of the earth and can only produce a surface field smaller than 0.2 γ. A review of the magnetic properties of lunar rocks can be found in Fuller (1974).

New bounds on the bulk relative magnetic permeability of the moon ($\frac{\mu}{\mu_o}$ = 1.03±0.02) were established by Parkin et al. (1973) by considering the data from Explorer 35 and the lunar surface magnetometers when the moon was in the geomagnetic tail.

No significant toroidal H field was found on the surface of the moon. However, the discovery of a large remanent magnetic field leads to the suggestion by Barnes et al. (1971) that when such a field is present near the terminator, it might interact with the solar wind to produce the observed small limb compression. A preliminary check of this hypothesis was made by Lichtenstein et al. (1974) with the data from the Apollo 15 subsatellite. They found that the occurrence rates of limb compression are roughly proportional to the amplitudes of the remanent fields observed at satellite altitude.

Large amplification of the tangential components of the magnetic field at the lunar surface was observed by comparing the magnetic fluctuations at Explorer 35 to the one at a LSM when both instruments were on the sunlit side of the moon and outside the geomagnetic tail (see, for example, Sonett et al.,1971 a). Detailed power spectral density of each component of the field was evaluated at the LSM (P^L_{LSM}) and Explorer 35 (P^L_{EXP}) when the latter instrument was on the upstream side of the moon. If, at an LSM site, we define a mutually orthogonal set of unit vectors $\vec{x}$, $\vec{y}$, $\vec{z}$ (vertical, eastward and northward, respectively), then the data can be expressed in the form of an amplification factor A_L (L = x, y, z) were

$$A_L = (P^L_{LSM}/P^L_{EXP})^{1/2}$$

The coordinate system used to evaluate the power spectral density from Explorer 35 is made to correspond to the one used at the LSM site. The data is presented in Figures 1.2, 1.3, and 1.4. These power spectra were evaluated when the moon was either in the free streaming solar wind or in the earth's magnetosheath. Figure 1.2 represents data obtained at the Apollo 12 site when the LSM was on the sunlit side of the moon. The data in Figure 1.3 were also obtained at the Apollo 12 site but the LSM was on the night side of the moon, within 45° from the antisolar point. Figure 1.4 represents data obtained at the Apollo 15 site when the LSM was on the

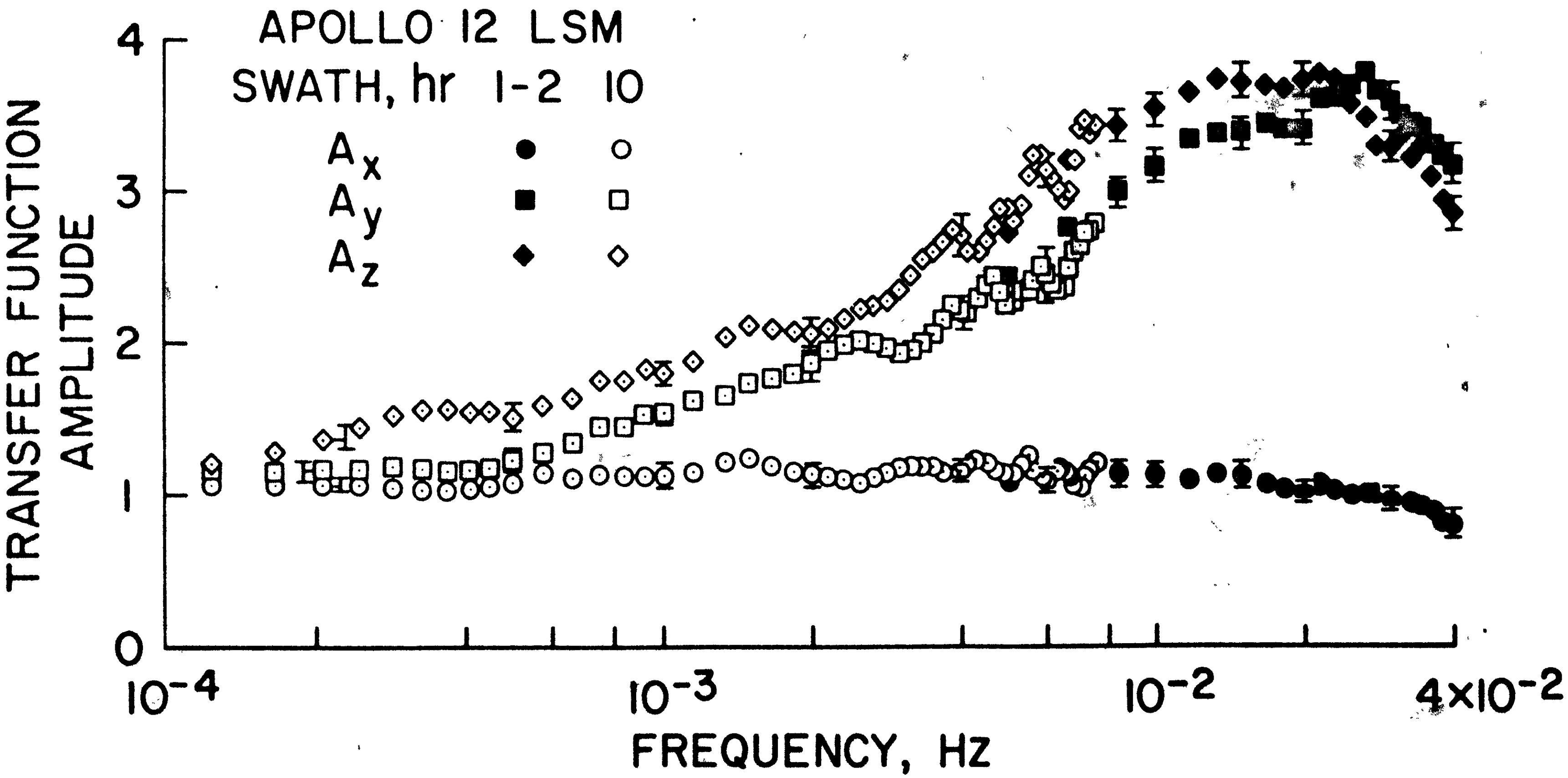
APOLLO 12 LSM
SWATH, hr 1-2 10
A_x ● ○
A_y ■ □
A_z ◆ ◇
TRANSFER FUNCTION AMPLITUDE
0
1
2
3
4
10^{-4}
10^{-3}
10^{-2}
4×10^{-2}
FREQUENCY, HZ

Figure 1.2

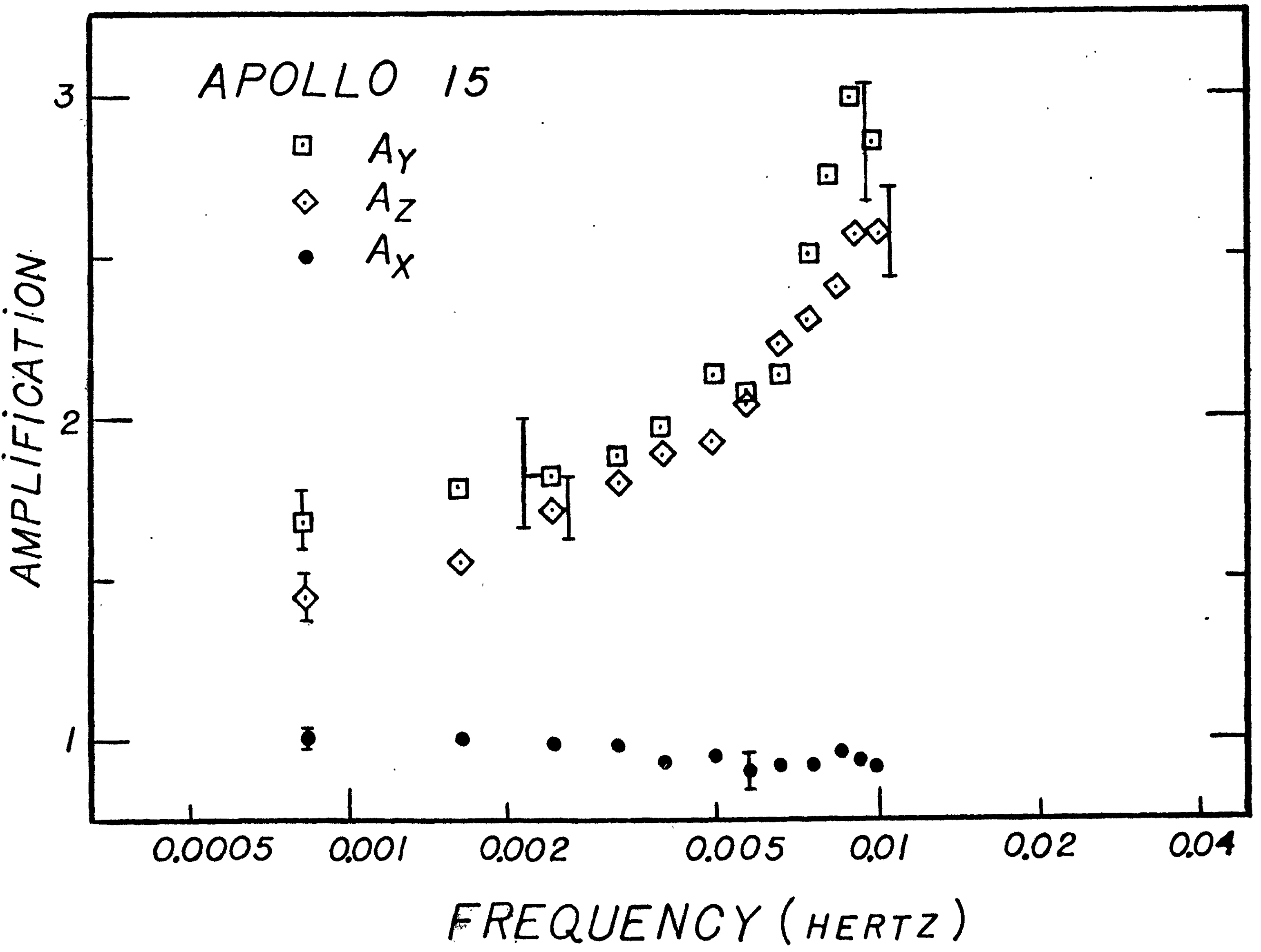
APOLLO 15
A_Y
A_Z
A_X
AMPLIFICATION
3
2
1
0.0005
0.001
0.002
0.005
0.01
0.02
0.04
FREQUENCY (HERTZ)

Figure 1.3

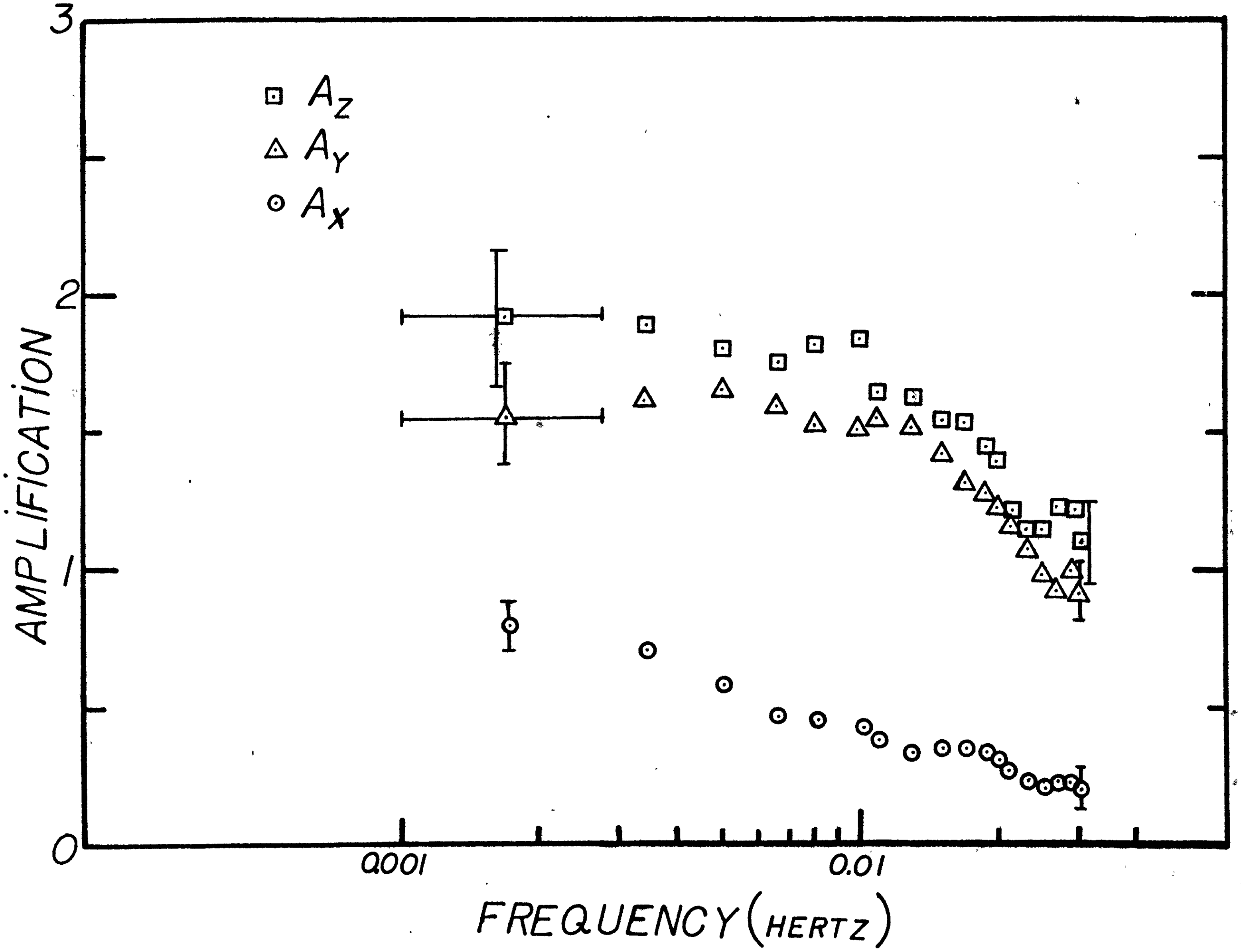

Figure 1.4

sunlit side of the moon, within 45° from the terminator. The data in Figures 1.2 and 1.3 are from Smith et al. (1973), whereas those in Figure 1.4 are from Schubert et al. (1973). The technique used to evaluate these spectra has been discussed by Sonett et al. (1971 b). Recently, Schubert et al. (1974 b) have published the amplification factors obtained when the moon was in the plasma sheet of the geomagnetic tail. These latter data will not be used in this thesis.

In the initial inversion of the sunlit side data, Sonett et al. (1971 c) assume the solar wind plasma to be radially incident on the moon. They obtain a conductivity profile characterized by a relatively large spike at a depth of approximately 250 km. But conductivity profiles with this peaked behavior were soon recognized to be only part of a larger set of models, many of which smoothly varying, that fit equally well the frontside data. (See, for example, Kuckes, 1971 and Sonett, 1972.)

The night side data were initially interpreted by Dyal et al. (1973b), who investigated the passage of large magnetic field discontinuities in the solar wind. They assumed the moon to be surrounded by a vacuum and inverted the time domain response of the moon to these discontinuities. They found that, in addition to a constant conductivity layer of 3 x 10^{-4} mho/m in the upper 700 km of the moon (except for a thin -- ≃ 40 km -- non-conducting crust), they also require a core of conductivity 10^{-2} mho/m at depth greater than 700 km in order to fit the decay time of the vertical magnetic field component of the discontinuity. Schubert et al. (1973 a), however, showed that, using the vacuum approximation, the radial amplification factor in Figure 3 poorly resolves the conductivity of the bottom layer. Moreover, they showed that the tangential amplification factors on the night side cannot be inverted within a model that assumed the moon to be embedded in a vacuum. This is due to the neglect of confining current on the frontside of the moon and at the plasma vacuum boundary. The effect of these currents is to amplify the tangential surface magnetic field to a value higher than can possibly be reached by any conductivity model within the vacuum approximation.

The radially incident plasma model also suffers from its neglect of the plasma void behind the moon. One aim of this study is to incorporate in a single model the dayside-nightside asymmetry in the plasma environment of the moon. Concurrent with our effort, Schubert et al. (1973, b, c), Schwartz et al. (1973) and Smith et al.

(1973) have recently published initial results of a theory which account for the day-nightside asymmetry. We shall discuss some of their results as we go along in the next chapters.

1.5 Thesis Outline

Chapter II contains the field solution in the different regions around the moon, together with a discussion of the boundary conditions used in the analysis.

In Chapter III we discuss the numerical method used to solve the forward problem together with the properties of the solution for various lunar conductivity models and solar wind parameters.

In Chapter IV we solve the inverse problem for particular sets of parameters of the source field and discuss the resolvable feature of the conductivity structure together with the information distribution among the observations. Also, we subject the moon to various temperature models and discuss inferences that can be made on the parameters of a semi-conductor satisfying both the thermal and magnetic constraints.

Chapter II

Analysis of the Field

2.1 Introduction

We will consider only the period of the lunar month when the moon is either in the earth's magnetosheath or in the free streaming solar wind. During this period we can distinguish three regions in the moon's electromagnetic environment: the solar wind, the void cavity behind the moon, and the interior of the moon. In the following sections we discuss the field representation in each of these regions and their coupling through the boundary conditions.

The different coordinate systems used to represent the field are shown in Figure 2.1. Their origins should all coincide with the center of the moon but for clarity they have been translated parallel to the solar wind velocity. We will follow Morse *et al.* (1953) for the definition and notation of the various functions used in the text.

Since we expect the lunar response to be somewhere between the one expected for a spherically symmetric plasma and a vacuum environment, it is instructive to compare some of their characteristics before attempting to incorporate the various regions around the moon into a

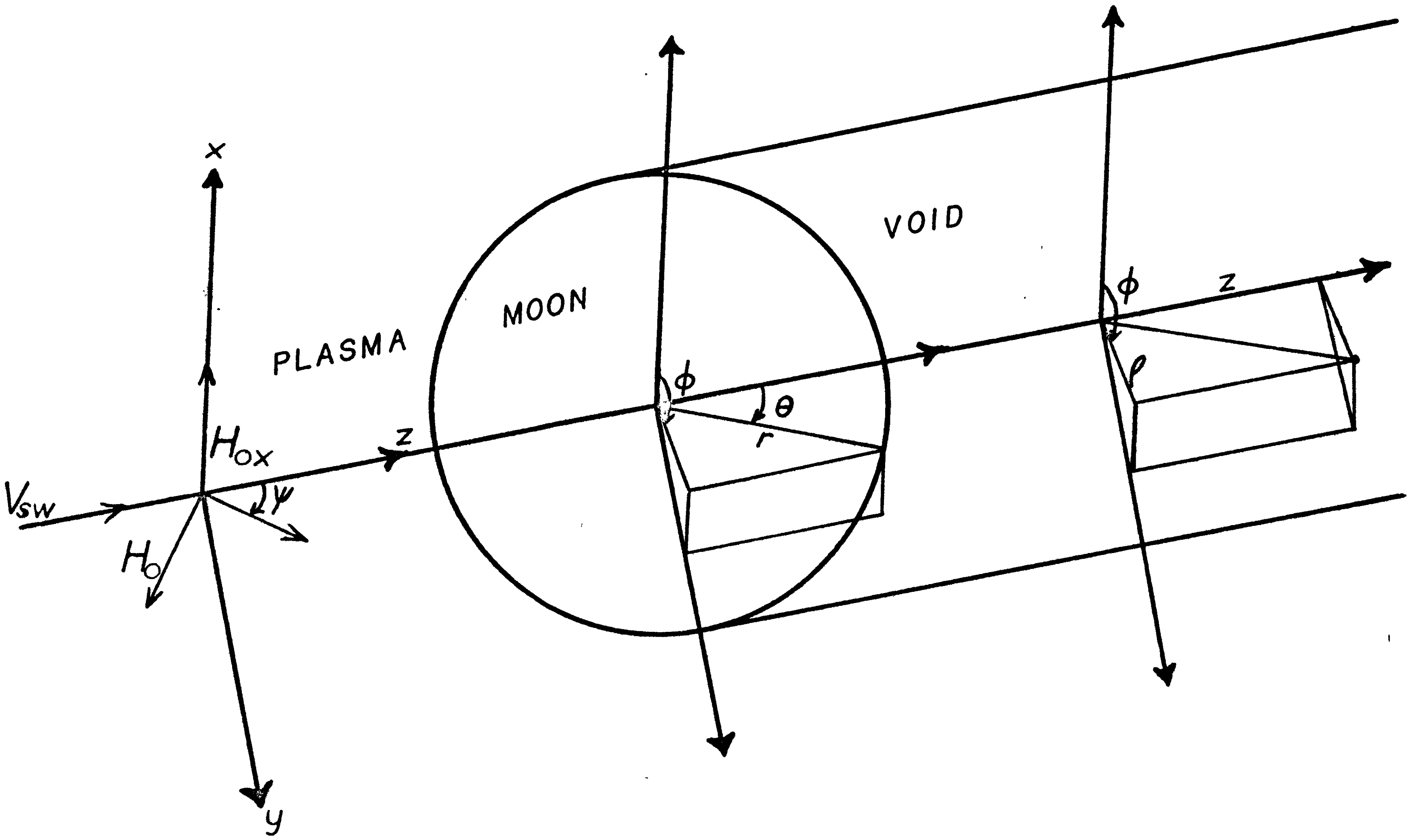

Figure 2.1

more comprehensive model. This is especially true in our case since the solution of the more realistic model can be reached only through a numerical method which lacks, to some extent, the insight provided by a simple close-form formula.

To avoid any of the complications arising from the structure of the source field, we shall assume the incident field to be spacially homogeneous and given (see Figure 2.1) by:

$$\vec{H}^{inc} = H_o\vec{a}_y = H_o(\vec{a}_r\sin\theta\sin\phi+\vec{a}_\theta\cos\theta\sin\phi+\vec{a}_\phi\cos\phi) \qquad (2.1.1)$$

In the vacuum approximation, we allow the induced field to expand into a void outside the moon We can express the total field in the void as the sum of the incident field and the field of a dipole, i.e.:

$$\vec{H}^{vac} = \vec{H}^{inc} + \nabla \times \nabla \times b \ \frac{R_M^3}{r} \sin\theta\sin\phi\vec{a}_r \qquad (2.1.2)$$

where r is the distance to the center of the moon and b is a constant to be determined by the boundary condition.

In order to gain some insight into the amplitude of the response, let us assume that the moon is formed of two layers, the top one an insulator and the bottom one a perfect conductor. The field in the insulating shell is given by

$$\vec{H}^{\mathrm{moon}} = \nabla \times \nabla \times \left(c\,\frac{R_M^3}{r} + dr^2\right) \sin\theta \sin\phi\,\vec{a}_r \qquad (2.1.3)$$

In both models, the magnetic field inside the moon must have a vanishing normal component at the surface of the perfect conductor of radius a. In the vacuum approximation, the three components of the magnetic field must be continuous at the lunar surface. In the symmetric plasma assumption, however, since we assume the induced field to be confined by a thin current layer above the surface of the moon, it is only necessary to equate, at the lunar surface, the normal component of the magnetic field inside the moon to the one of the incident field, as given in Equation (2.1.1). If we apply these boundary conditions and extract from the result the ratio of the tangential component of the magnetic field at the lunar surface to the one contained in the incident field, we obtain

$$A^{\mathrm{vac}} = 1 + \frac{a^3}{2R_M^3} \qquad (2.1.4)$$

$$A^{\mathrm{plasma}} = 1 + \frac{\frac{3}{2}\,a^3}{R_M^3 - a^3} \qquad (2.1.5)$$

These responses are plotted in Figure 2.2. We note first that the vacuum response can only reach an upper

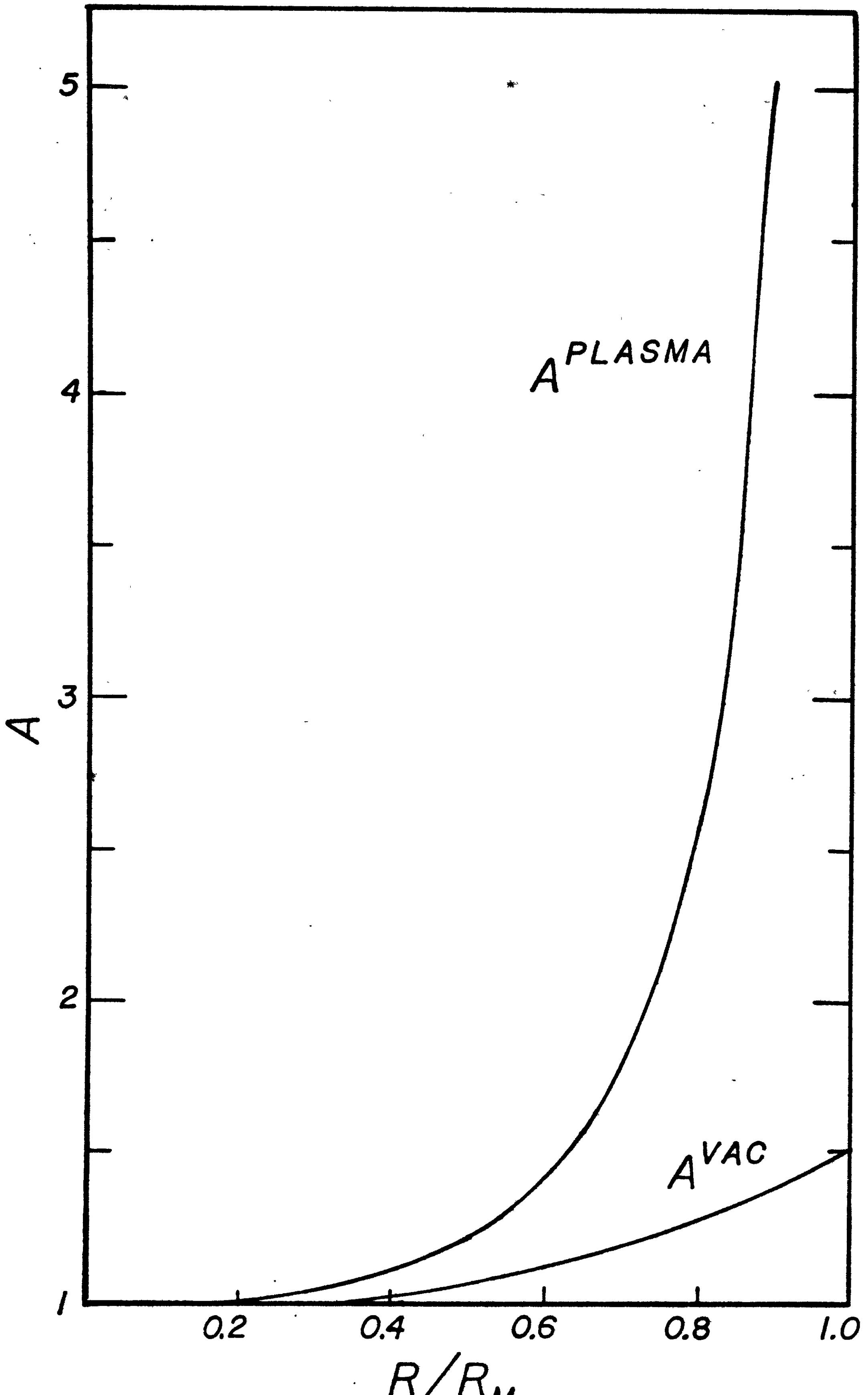

Figure 2.2

limit of 1.5. Since the data of Figure 1.3 exhibits measured value higher than this when the LSM is near the antisolar point, one can readily infer that the vacuum approximation is inadequate to interpret the tangential amplification factor in the more realistic geometry. Another point of interest is the detectability of conductivity deep in the lunar interior. For example, if we assume the data to have a 10% relative error due to noise, we note that even a perfect conductor of radius lying between about 700 km ($a \simeq 0.4R_M$) and 1000 km ($a \simeq 0.6\ R_M$), would yield a response only of the order of the uncertainties in the data.

A similar treatment can be given for the toroidal H magnetic field but since these results are completely worked out in Sill (1970) and are similar to our derivation in a simpler geometry given in Section 1.2, we omit them here and proceed directly to the task of representing the field in the various regions of the lunar environment.

2.2 Representation of the Field in the Solar Wind

In addition to its quasi-stationary sector structure, the interplanetary magnetic field is usually permeated by various magnetohydrodynamic shocks, discontinuities and waves. (For a review of the first two types of disturbance, see Burlaga, 1972). Belcher et al. (1971) have found substantial evidence that the power spectral density of the interplanetary magnetic field, in the frequency range where lunar induction has been measured (Figure 1.2), is dominated at least fifty percent of the time by large amplitude Alfven waves, propagating outward from the sun. Sari et al. (1969) have proposed an alternative model to explain these micro-scale (< 0.01 au) fluctuations. They suggest that the interplanetary magnetic field has a spaghetti-like filamentary structure, with bundles of lines-of-force separated from one another by tangential discontinuities and essentially static in the rest frame of the solar wind. Though the physics involved in these two models differs markedly, these differences are of little consequence for our application. A common characteristic that must be retained, however, is that the interplanetary magnetic fluctuations, as seen in the rest frame of the moon, are essentially convected at the solar wind speed. This approximation seems appropriate for the free streaming solar wind but the increase in the plasma pressure in the magnetosheath might produce wave velocities which are a substantial fraction of the solar wind velocity. Unfortunately, the data presented in Chapter I did not differentiate between these two lunar environments, so some caution should be used in their interpretation. We should note here that for waves propagating nearly perpendicular to the solar wind velocity, their phase velocity plays an important role in determining their spatial structure. Since such waves probably represent only a small fraction of the power density spectrum of the fluctuation, their contribution to the response shall not be considered any further.

We shall assume that we can represent the fluctuation as a superposition of plane waves convected as a constant solar wind velocity, $\vec{V}_{SW}$. In the first of these hypotheses, we assume that the magnetic fluctuations are not generated near the moon and thus have little sphericity in their structures. In the second assumption we ignore perturbation such as large solar-flare-associated shocks which significantly modify the solar wind velocity A change of 100 km/sec in the bulk speed within a minute's interval can occur during such events (Chao, 1970).

Let us choose the y-axis in Figure 2.1 such that the wave normal to a given fluctuation is in the y-z plane and subtends an angle ψ with respect to the solar wind velocity. If we assume ψ to be positive if the wave normal has a component along the +y direction, we can express the field as follows:

$$\vec{H} = H_o(\vec{a}_y\cos\psi-\vec{a}_z\sin\psi)e^{ik(z\cos\psi+y\sin\psi)}$$
$$+ H_{ox}\vec{a}_x e^{ik(z\cos\psi+y\sin\psi)}$$

where

$$k\cos\psi \equiv k_{//} = \frac{\omega}{V_{SW}} \qquad (2.2.1)$$

$$k\sin\psi \equiv k_{\perp} = \frac{\omega}{V_{SW}}\tan\psi$$

and

$$\vec{E} = -\mu_o\vec{V}_{SW} \times \vec{H}$$

A time factor, $e^{-i\omega t}$, is implicitly used here, as in all similar equations of this chapter, and $\underline{\omega}$ stands for the angular frequency measured in the rest frame of the moon. In the solar wind rest frame, however, a fluctuation with phase speed V_{ph} and propagating parallel to the solar wind velocity is seen with an angular frequency equal to $\frac{\omega V_{ph}}{V_{SW}+V_{ph}}$.

For example, an Alfven wave, at the highest angular frequency for which the lunar response has been measured, 0.25 rad./sec. (Figure 1.2), has an angular frequency of 0.02 - 0.05 rad./sec. in the solar wind frame. This is still about an order of magnitude smaller than the nominal proton gyrofrequency in the solar wind (0.5 rad./sec). Also for the case of an Alfven wave, we have neglected the electric field in the rest frame of the wind. Equation (2.2.1) should still give a good first order approximation, however, since this electric field is smaller than the one associated with the motion of the solar wind by the factor:

$$\frac{V_{SW}}{V_A} \simeq (5 - 10).$$

2.3 The Field Inside the Moon

We assume the moon to consist of spherical layers of constant thicknesses and homogeneous conductivities. Such a structure is in harmony with a lunar model where the conductivity is mainly determined by the composition and temperature and where both can be assumed to vary only along the radius. If thermal conduction is the main heat transfer process inside the moon, this would seem to be a reasonable assumption for the temperature distribution. However, if solid state convection plays an important role in heat transfer, Turcotte et al. (1972) have suggested that a significant asymmetry in the temperature distribution could be introduced at depth where convection occurs.

Also, if extensive lateral inhomogeneities in a global radially-varying moon structure are located near a given magnetometer, they might significantly influence the signal observed at this instrument, especially at the higher frequencies. Even though power spectral data have been published from only the Apollo 12 and 15 site magnetometers, already there is substantial evidence that a regional signature is detected at the latter site. Schubert et al. (1974c), by examining the power density spectrum at different angles in a plane tangent to the surface at the Apollo 15 site, found that the distribution of power is strongly peaked along the northwest-southeast line at frequencies above approximately 5 mHz. This direction of polarization seems to be observed consistently and is independent of the directional character of the solar wind power spectrum and of the position of the magnetometer in the asymmetric plasma environment. A likely expalantion for the anisotropic character of the response is that some regional inhomogeneities influence the data at the site. Maxima in the power spectrum of the tangential magnetic field components were also observed at the Apollo 12 site. But since between approximately 0.001 and 0.02 Hz, the peak tends to align along a line parallel to the tangential component of the remanent field at this site (≃ 64° south of east), it was tentatively attributed to a modulation of this field by fluctuations in the dynamic pressure of the solar wind (Sonett et al., 1972). We examine briefly this suggestion in Appendix I, but it should be pointed out here that anisotropy in the power spectrum of the tangential magnetic field component is also observed by the Apollo 12 magnetometer when this instrument is on the dark hemisphere of the moon. Its detailed properties have not yet been presented in the literature, but its existence can be inferred from Figure 1.4. So a regional influence on the data might also accompany the noise due to the remanent field at this site.

Thus, even if the bulk of the moon can be modelled approximately by a radially-varying structure, we nevertheless face the problem of extracting its global induction signal from data contaminated by noise and regional inhomogeneities. A first empirical step in that direction was made by Sonett et al. (1972) who estimated the values of the tangential amplification factor at the Apollo 12 site, along a direction such that this quantity is minimal (e.g., between 0.001 and 0.02, along a line parallel to ≈E25°N, i.e., orthogonal to the direction of the tangential remanent field). We show these data, A_{min}, in Figure 2.3, together with the data of Figure 1.4 (and a data point from Figure 1.2). We note that the Apollo 15 data, though probably influenced by the cause of the peak along the northwest-

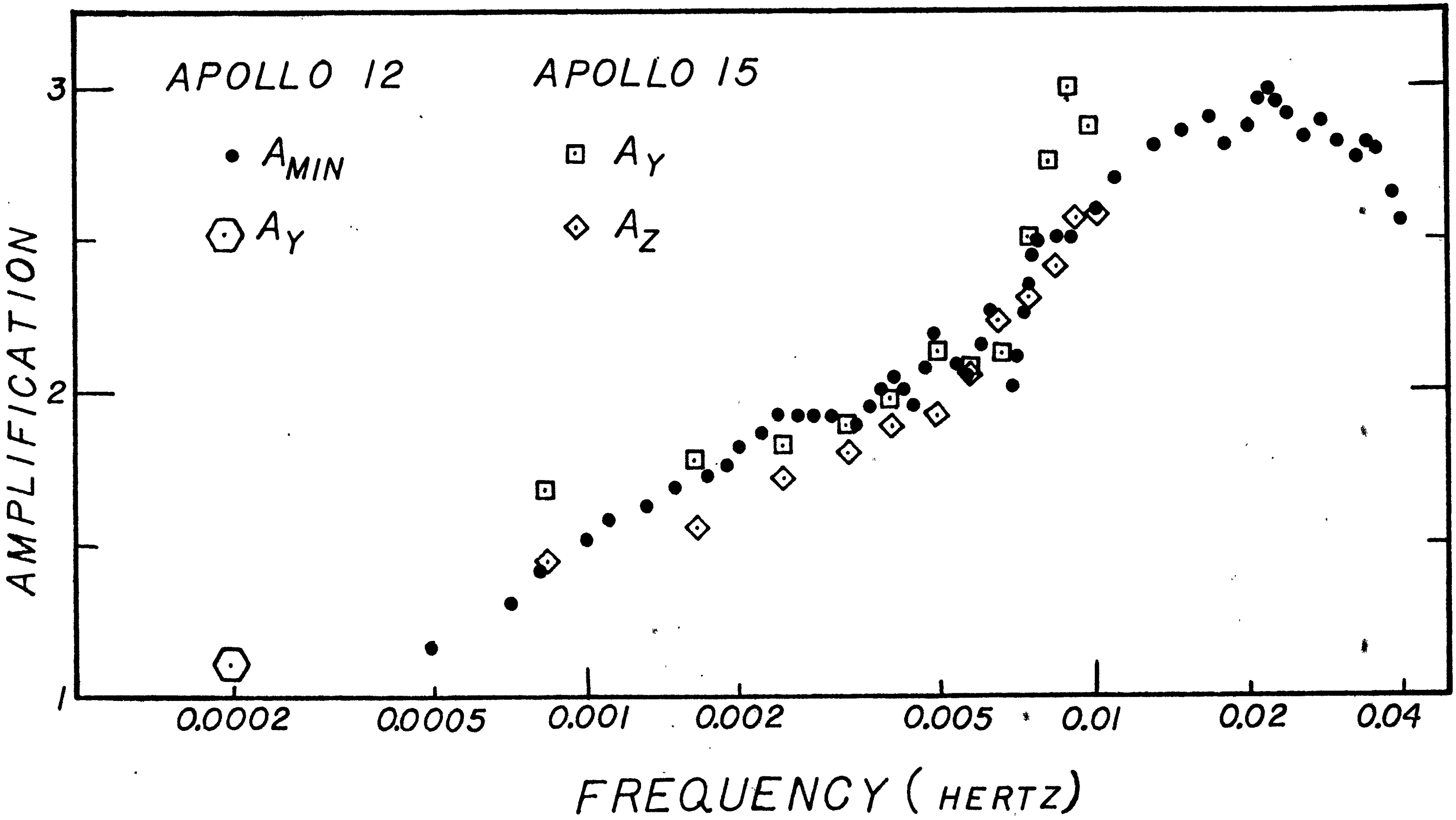
APOLLO 12
● A_{MIN}
⬡ A_Y
APOLLO 15
□ A_Y
◇ A_Z
AMPLIFICATION
1
2
3
0.0002
0.0005
0.001
0.002
0.005
0.01
0.02
0.04
FREQUENCY (HERTZ)

Figure 2.3

southeast line, agree fairly well with these A_{min} values. This set of data thus probably represents a good first approximation of the global response of the moon. But, of course, in order to qualify this inference, a more detailed data analysis is required, in conjunction with theories that account for the possible regional influences and other sources of noise.

We now turn to the solution of the Maxwell equation inside a layered sphere. These solutions are well known so we shall only summarize some of the main results here.

The continuity of the tangential components of the $\vec{E}$ and $\vec{H}$ fields* can be applied to each of the two electromagnetic modes independently at an internal boundary of the sphere. This permits us to determine, for each harmonic of each mode, the ratio of electric to magnetic field at the lunar surface. Instead of dealing with impedances, however, we found it convenient to define, in Appendix II, some related quantities, L_n and T_n, which permit us to write the field as follows:

---

*Here we assume the moon to have a constant permeability equal to the free space value.

$$\vec{H} = \sum_{n,m} \vec{a}_r \, n(n+1) a^{\sigma}_{nm} P^{m}_{n}(\cos\theta) \left\{\begin{matrix}\sin\\ \cos\end{matrix}\right\} m\phi$$

$$+ \vec{a}_\theta \Big[a^{\sigma}_{nm} L_n \frac{\partial P^{m}_{n}(\cos\theta)}{\partial\theta} \left\{\begin{matrix}\sin\\ \cos\end{matrix}\right\} m\phi$$

$$\pm \frac{m b^{\sigma}_{nm} T_n P^{n}_{n}(\cos\theta)}{ik_{//} R_M \sin\theta} \left\{\begin{matrix}\cos\\ \sin\end{matrix}\right\} m\phi \Big]$$

$$+ \vec{a}_\phi \Big[\pm m a^{\sigma}_{nm} L_n \frac{P^{m}_{n}(\cos\theta)}{\sin\theta} \left\{\begin{matrix}\cos\\ \sin\end{matrix}\right\} m\phi$$

$$- \frac{b^{\sigma}_{nm} T_n \partial P^{m}_{n}(\cos\theta)}{ik_{//} R_M \partial\theta} \left\{\begin{matrix}\sin\\ \cos\end{matrix}\right\} m\phi \Big]$$

and

$$\vec{E} = \mu_o V_{SW} \Big[\sum_{n,m} \vec{a}_r \, n(n+1) b^{\sigma}_{nm} \frac{T_n}{(k_s R_M)^2} P^{m}_{n}(\cos\theta) \left\{\begin{matrix}\sin\\ \cos\end{matrix}\right\} m\phi \qquad (2.3.1)$$

$$+ \vec{a}_\theta \Big[\pm m i k_{//} R_M a^{\sigma}_{nm} \frac{P^{m}_{n}(\cos\theta)}{\sin\theta} \left\{\begin{matrix}\cos\\ \sin\end{matrix}\right\} m\phi$$

$$+ b^{\sigma}_{nm} \frac{\partial P^{m}_{n}(\cos\theta)}{\partial\theta} \left\{\begin{matrix}\sin\\ \cos\end{matrix}\right\} m\phi \Big]$$

$$+ \vec{a}_\phi \Big[-a^{\sigma}_{nm} i k_{//} R_M a^{\sigma}_{nm} \frac{\partial P^{n}_{n}(\cos\ )}{\partial\theta} \left\{\begin{matrix}\sin\\ \cos\end{matrix}\right\} m\phi$$

$$\pm m b^{\sigma}_{nm} \frac{P^{m}_{n}(\cos\theta)}{\sin\theta} \left\{\begin{matrix}\cos\\ \sin\end{matrix}\right\} m\phi \Big] \Big]$$

where $k_s^2 = i\omega\mu_o\sigma_s$, ($\sigma_s$ is the conductivity of the surface layer) and $k_{//}$ is defined in Equation (2.2.1).

The coefficients a_{nm}^{σ} and b_{nm}^{σ} are the coefficients of the poloidal and toroidal H mode, respectively, and are to be determined by applying the boundary conditions at the lunar surface.

2.4 The Field in the Void Region on the Downstream Side of the Moon

In order to obtain a tractable representation of the field in the void region on the dark side of the moon, some assumptions must be made on the parameters of the solar wind. We shall adopt the following three hypotheses:

1. We can treat the solar wind as a cold plasma. In other words, we shall neglect any effect of the thermal pressure compared to the magnetic pressure.

2. We assume that the ratio of the solar wind bulk speed to hydromagnetic wave speed can be considered infinite.

3. We assume the solar wind velocity to be time- and space-independent both in magnitude and direction.

We hasten to point out, however, that the solar wind β is on average equal to about 1, and finite β effects are readily observable in terms of penumbral decrease and umbral increase of the magnetic field (Ogilvie et al., 1969). Moreover, a finite, but high, Mach number effect has been observed by Whang et al. (1970), who measured a Mach cone angle of 8°. But, unfortunately, it is difficult to relax these assumptions or to calculate their probable influence on the data, in the frequency range where lunar induction is important, since (i) simultaneous data of all relevant solar wind parameters are generally not available, and (ii) we lack a proper theory that accounts for these effects. (To date, even steady state theory predicts some parameter dependence of the magnetic field that has no counterpart in the observation (see, for example, Ogilvie et al., 1969).

We shall content ourselves in this thesis to check that a theory that incorporates these assumptions does in fact reproduce some of the major frequency-dependent characteristics of the field observed around the moon. This procedure is somewhat unsatisfactory, however, since the agreement comes largely as the result of a successful search for a conductivity profile that satisfies the observations within the framework of the approximation theory. But the very fact that such a model can be found that agrees reasonably well with both front and backside data, does give some measure of confidence in the approximation theory used. This trust is further improved by the fact that the theory can reproduce at this stage, at least qualitatively, some of the major frequency characteristics of the field observed in the void region, sufficiently far downstream so that it is uninfluenced by the moon.

In order to discuss this last point, let us examine some of the consequences of the hypothesis we made.

First, the geometry of the vacuum region can be modelled by a semi-infinite circular cylinder with its radius equal to the lunar radius. Moreover, the boundary conditions on the electromagnetic field can be most easily obtained since the boundary layer between the void and the undisturbed solar wind can be considered infinitesimally thin. This permits us to match, at the boundary of the cylinder, the normal component of the solar wind magnetic field and its wavelength parallel to the axis of the cylinder to a solution of Maxwell's equations inside the void. This solution can be given in terms of a cylindrical TE mode that also satisfies the continuity of the tangential electric field components across the plasma-vacuum boundary layer. The normal component of $\vec{H}$ of the solar wind field, at the boundary of the cylinder, can be evaluated from Equation (2.2.1) and the resulting field inside the void can be expressed as follows:

$$\vec{H} = \frac{\nabla \times \vec{E}}{i\omega\mu_o}$$

$$\vec{E} = \sum_{m,\sigma} \nabla \times \psi_m^\sigma \vec{a}_z$$

where

$$\psi_m^\sigma = g_m^\sigma I_m(k_{//}\rho) e^{ik_{//} z} \left\{ \begin{matrix} \sin \\ \cos \end{matrix} \right\} m\phi$$

$$(2.4.1)$$

$$g_m^1 = \gamma_m^o f_m + \gamma_m^e ih_m$$

$$g_m^2 = \gamma_m^e if_m + \gamma_m^o h_m$$

$$f_m = \frac{H_o \omega\mu_o \cos\psi \, J_m(k_\perp R_M)}{k_{//}^2 I_m'(k_{//} R_M) \varepsilon_m}$$

$$h_m = \frac{H_{ox} \omega\mu_o \, 2m \, J_m(k_\perp R_M)}{k_{//}^2 I_m'(k_{//} R_M) \, k_\perp R_M}$$

where

ε_m = Neuman factor = 1 when $m = 0$ and
= 2 when $m > 0$

and where here and in the following development, we use the following definition :

$$\gamma^{o}_{mni\ldots} = 1 \qquad \text{if } m + n + i + \ldots \text{ is odd}$$
$$= 0 \qquad \text{if } m + n + i + \ldots \text{ is even}$$

and

$$\gamma^{e}_{mni\ldots} = 0 \qquad \text{if } m + n + i + \ldots \text{ is odd}$$
$$= 1 \qquad \text{if } m + n + i + \ldots \text{ is even}$$

The prime stand for the derivative with respect to the argument and J_m, I_m are the Bessel and hyperbolic Bessel functions in their usual notation.

This field is not sufficient, however, to match the boundary conditions on the surface of the moon. To accomplish this, we must add an "end effect field" that will be discussed shortly. But before doing this, let us digress a little to examine some of the properties of Equation (2.4.1).

We note first that for very low frequencies, $k_{//}R_M << 1$, the field is homogeneous and has the same value as the unperturbed solar wind field. Thus, due to our idealization of the plasma parameters, we do not reproduce the penumbral decrease nor umbral decrease observed behind the moon (Figure 1.1). On the other hand, for frequencies such that $k_{//}R_M >> 1$, Equation (2.4.1) shows that the power spectral density in the void should be at a much lower level than what is observed in the unperturbed solar wind. The ratio of the power spectral densities in that frequency range and on the axis of the cylinder, is approximately given by $e^{-2k_{//}R_M}$. This characteristic of the field inside the void is due to the surface wave nature of the TE mode. The solution of the vector Laplace equation, propagating along the axis of the cylinder, decays approximately exponentially away from the boundary of the cylinder when $k_{//}R_M >> 1$. In harmony with this result, a sharp drop in the power spectral density of the magnetic field in the void was observed by Ness _et al._ (1969), at frequencies above about 0.1 Hz ($k_{//}R_M \simeq 3$). But a detailed quantitative comparison is hindered by our lack of knowledge of the exact position of the satellite (in particular its distance from the axis of the cylinder) during these observations.

Another type of observation that incorporates both of these limiting features is the response of the void cavity to large discontinuities in the interplanetary magnetic field. One such event, recorded when Explorer 35 was near the axis of the cylinder, is shown in Figure 2.4*.

---

*The data in Figure 2.4 and the calculation in Figure AP-III are presented in a right-handed geocentric solar ecliptic coordinate system with +X toward the sun and +Z toward the ecliptic north.

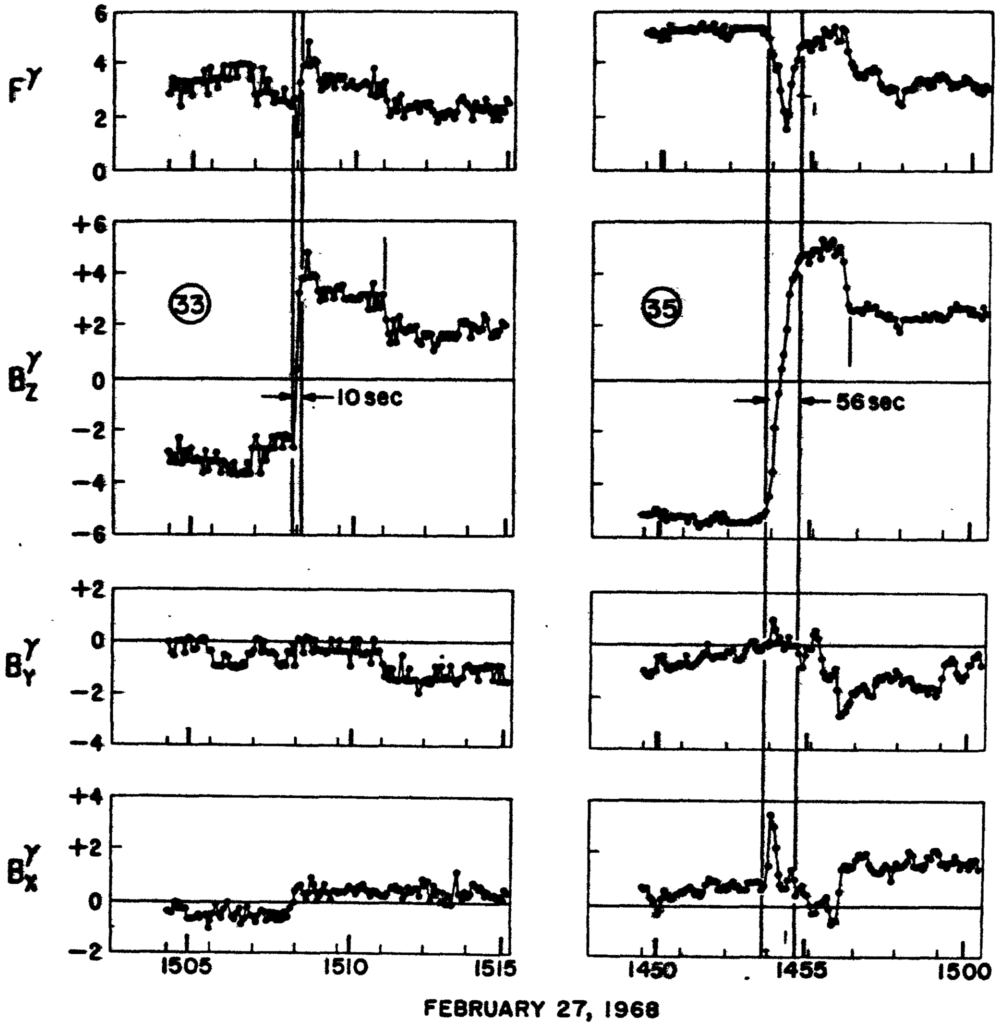

The identical transient at Explorer 33 and 35 using the GSFC magnetometer (5-Hz bandwidth).

SATELLITES LOCATION
IN GEOCENTRIC SOLAR ECLIPTIC COORDINATE SYSTEM

UNIT: EARTH RADII 1 R_E

	X	Y	Z
EXPLORER 33	37.2	-56.3	-23.3
EXPLORER 35	59.5	- 8.4	- 4.1

With Respect to the Center of the Moon:

UNIT: 1 R_M

EXPLORER 35	-1.71	- 0.04	0.26

Figure 2.4

Also shown is the observation of the same event by Explorer 33 about fifteen minutes later, while this satellite, orbiting around the earth, was outside the bow shock.

The difference in the jump in the Z components probably arises due to the finite β of the solar wind. An interpretation of the other two characteristic differences, namely the dilatation in the rise time of the Z component and the small peak in the X component, in terms of a signature of a conductive lunar interior was ruled out by Sonett et al. (1971d). Instead they suggested that since the two satellites are widely separated ($\simeq 53\ R_E$), the signal difference might be attributed to a natural difference in the solar wind field at their locations. Though such solar wind field differences might exist, we examine the possibility in Appendix III that these characteristics are caused by the surface wave nature of the field in the void region. We find good qualitative agreement with the data using values predicted by Equation (2.4.1).

We now return to our derivation of the field and proceed to complete our representation by discussing the "end effect" field.

At the vacuum plasma interface, the field must have a vanishing normal component of its magnetic field and tangential component of its electric field. This comes about because we assume the solar wind to be unperturbed outside an infinitesimally thin boundary layer at the cylinder boundary. The void region is thus similar to a hollow pipe with perfectly conducting wall. A possible solution of the Maxwell equations in that geometry can be given in terms of the cylindrical waveguide modes (see, for example, Stratton, 1941). That is:

$$\vec{H} = \frac{\nabla \times \vec{E}}{i\omega\mu_o}$$

$$\vec{E} = \sum_{\ell,m,\sigma} \nabla \times \psi^{\sigma}_{\ell m} \vec{a}_z + \nabla \times \nabla \times \Phi^{\sigma}_{\ell m} \vec{a}_z$$

where

$$\psi^{\sigma}_{\ell m} = A^{\sigma}_{\ell m}\, i\omega\mu_o J_m(\beta_{\ell m}\rho/R_M)\, e^{-\beta_{\ell m} z/R_M} \left\{\begin{matrix}\sin\\ \cos\end{matrix}\right\} m\phi$$

$$\Phi^{\sigma}_{\ell m} = B^{\sigma}_{\ell m} J_m(\alpha_{\ell m}\rho/R_M)\, e^{-\alpha_{\ell m} z/R_M} \left\{\begin{matrix}\sin\\ \cos\end{matrix}\right\} m\phi \qquad (2.4.2)$$

where $\beta_{\ell m}$ and $\alpha_{\ell m}$, $\ell = 1, 2, \ldots$ are the roots of $J'_m(z)$ and $J_m(z)$ respectively and where $A^{\sigma}_{\ell m}$ and $B^{\sigma}_{\ell m}$ are the coefficients of the cylindrical TE and TM modes respectively.

Equation (2.4.2) is valid when the frequency is well below the cut-off frequency for mode propagation.

The smallest cut-off frequency for either the TE or TM modes is $\frac{c\,\beta_{11}}{2\pi R_M} \simeq 50$ Hz, where c is the speed of light. Since we are interested in frequencies much lower than this, the approximation is justified.

The mode representation given by Equation (2.4.2) should be sufficiently accurate downstream of the antisolar point but extension of its validity to the lunar surface involves the so-called Rayleigh hypothesis (Millar, 1973). Indeed, in the vacuum region bounded by the lunar surface and a plane perpendicular to the axis of the cylinder and containing the antisolar point there is no physical reason to impose the condition that the modes are decaying downstream. To illustrate this point, let us assume there is a magnetic dipole on the axis of the cylinder half-way between the center of the moon and the antisolar point. Furthermore, let us assume that the sphere is inside an infinite cylinder. Solution of this problem involves the Green function associated with a magnetic dipole inside a cylinder (see, for example, Smythe, 1968). This Green function is expressed in cylindrical TE and TM modes that are decaying upstream for $z < R_M/2$ and downstream for $z > R_M/2$. Though, in that case, the field can be represented by both upstream and downstream decaying modes it does not necessarily follow that in the region $z > 0$ and $(z^2 + \rho^2)^{1/2} > R_M$ we cannot express the field with only modes decaying downstream. Indeed, this is usually not the case. We recall that the potential field outside a sphere of radius R_M, caused by a distribution of charge and currents inside it can always be represented by a series of electric and magnetic multipoles situated at its center. For example, for the problem above, we can find an equivalent distribution of magnetic multipoles at the center of the sphere, and then use the Green function associated with each multipole to represent the total field outside the sphere. Since the equivalent multipoles are situated at the center of the sphere, only +z decaying modes are required in $z > 0$; but, on the other hand, the expression is valid in general only in $(z^2 + \rho^2)^{1/2} > R_M$.

Let us formalize this concept for the case of the moon. We assume that the field in the downstream cylinder caused by the currents and charges inside the moon and on its sunlit surface can be represented by a series of electric and magnetic multipoles situated at its center. This partial field is the elementary solution of Maxwell's equations and can be found in most text books on electromagnetic theory. To the field of each multipole we can add a series of spherical TE and TM modes, regular at the origin and such that the total field at the boundary of the cylinder has a vanishing tangential electric field component and normal magnetic field component. This field can be found through the use of a dual Fourier-Bessel series, as shown in Appendix IV. The result, in a spherical coordinate system, is as follows:

$$\vec{H} = \frac{\nabla \times \vec{E}}{i\omega\mu_o}$$

$$\vec{E} = \sum_{n,m} i\omega\mu_o R_M^2 \, t^\sigma_{nm} [\nabla \times \psi^\sigma_{nm} \, \vec{a}_r + \nabla \times \nabla \times \Phi^\sigma_{nm} \, \vec{a}_r]$$

$$+ R_M^2 \, d^\sigma_{nm} \, \nabla \times \nabla \times \Lambda^\sigma_{nm} \, \vec{a}_r \qquad (2.4.3)$$

where

$$\psi^\sigma_{nm} = [(\frac{R_M}{r})^n P_n^m(\cos\theta) + \sum_{p=m}^{\infty} c_{nm\rho}(\frac{r}{R_M})^{p+1} P_p^m(\cos\theta)]\left\{\begin{matrix}\sin\\ \cos\end{matrix}\right\}m\phi$$

$$\Phi^\sigma_{nm} = \sum_{p=m}^{\infty} \pm m \, f_{nmp} R_M (\frac{r}{R_M})^{p+1} P_p^m \, (\cos\theta)\left\{\begin{matrix}\cos\\ \sin\end{matrix}\right\}m\phi$$

$$\Lambda^\sigma_{nm} = [(\frac{R_M}{r})^n P_n^m(\cos\theta) + \sum_{p=m}^{\infty} g_{nmp}(\frac{r}{R_M})^{p+1} P_p^m(\cos\,\theta) \, \left\{\begin{matrix}\sin\\ \cos\end{matrix}\right\}m\phi$$

$$c_{nmp} = -(\gamma^e_{nm}\gamma^e_{mp} + \gamma^o_{mn}\gamma^o_{mp}) \, h_{nmp} N_m(n+p)$$

$$f_{nmp} = (\gamma^e_{nm}\gamma^o_{mp} + \gamma^o_{nm}\gamma^o_{mp}) \, q_{nmp}[M_m(n+p-1) - \frac{n}{p} N_m(n+p-1)]$$

$$g_{nmp} = (\gamma^e_{nm}\gamma^e_{mp} + \gamma^o_{mn}\gamma^o_{mp}) h_{nmp} M_m(n+p)$$

$$h_{nmp} = \frac{n i^{p-n}}{(n-m)! \, (p+m)! \, (n+p+1)(p+1)} \, (\frac{n+p}{2})! \, (\frac{n+p}{2})!$$

$$q_{nmp} = \frac{i^{p-n-1}}{(n-m)! \, (p+m)! \, (n+p)(p+1)} \, (\frac{n+p-1}{2})! \, (\frac{n+p-1}{2})!$$

where the constant $N_m(2\ell)$ and $M_m(2\ell)$ are defined in Appendix V.

Following Watson (1930), we can show that the potentials ψ^σ_{nm}, Φ^σ_{nm} and Λ^σ_{nm} are absolutely convergent provided $r < 2R_M$. If we are interested in the field farther downstream, we can transform our multipole representation into a series of cylindrical waveguide modes. The algebra necessary to accomplish this transformation is outlined in Appendix IV and the result is as follows:

$$\begin{aligned} \vec{H} &= \frac{\nabla \times \vec{E}}{i\omega\mu_o} \\ \vec{E} &= \nabla \times \psi^\sigma_{nm}\vec{a}_z + \nabla \times \nabla \times \Phi^\sigma_{nm}\vec{a}_z + \nabla \times \nabla \times \Lambda^\sigma_{nm}\vec{a}_z \end{aligned} \tag{2.4.4}$$

where

$$\psi^\sigma_{nm} = i\omega\mu_o \sum_{m,\ell,\sigma} A^\sigma_{m\ell} J_m(\beta_{m\ell}\rho/R_M) e^{-\beta_{m\ell}z/R_M} \left\{ \begin{matrix} \sin \\ \cos \end{matrix} \right\} m\phi$$

$$\Phi^\sigma_{nm} = -i\omega\mu_o R_M \sum_{m,\ell,\sigma} \pm\, mB^\sigma_{m\ell} J_m(\alpha_{m\ell}\rho/R_M) e^{-\alpha_{m\ell}z/R_M} \left\{ \begin{matrix} \cos \\ \sin \end{matrix} \right\} m\phi$$

$$\Lambda^\sigma_{nm} = \sum_{m,\ell,\sigma} C_{m\ell}\, J_m(\alpha_{m\ell}\rho/R_M) e^{-z\alpha_{m\ell}/R_M} \left\{ \begin{matrix} \sin \\ \cos \end{matrix} \right\} m\phi$$

$$A^\sigma_{m\ell} = \sum_n \frac{2nt^\sigma_{nm}R_M^2(\beta_{m\ell})^n}{(n-m)!\,(\beta^2_{m\ell} - m^2)\,J^2_m(\beta_{m\ell})}$$

$$B^{\sigma}_{m\ell} = \sum_{n} \frac{2t^{\sigma}_{nm} R^2_M (\alpha_{m\ell})^{n-3}}{(n-m)!\, J^2_{m-1}(\alpha_{m\ell})}$$

$$C_{m\ell} = \sum_{n} \frac{2nR^2_M d^{\sigma}_{nm} (\alpha_{m\ell})^{n-2}}{(n-m)!\, J^2_{m-1}(\alpha_{m\ell})}$$

where t^{σ}_{nm} and d^{σ}_{nm} are the multipole coefficients given by Equation (2.4.3) and which must be found by applying the boundary conditions at the lunar surface.

We should point out that in this expression, a formal interchange of the order of summation between n and ℓ was made. However, for a given n, if the ℓ summation is made first, the cylindrical waveguide mode expression for the field of a given multipole is poorly convergent for small values of z and, in fact, usually diverges for z = 0. Thus it is difficult to justify theoretically the use of Equation (2.4.2) to express the end effect field in the void. This difficulty can, however, be countered by checking how well our boundary conditions are matched on the back side of the moon and, if a good match occurs, appeal to the uniqueness of the solution for Maxwell's equations to ascertain the validity of the representation. Both the representation given by Equation (2.4.2) and Equation (2.4.3) were used to match the boundary conditions behind the moon and in both cases a good fit was found.

Schwartz et al. (1973) also used the cylindrical waveguide mode to represent the "end effect" field and they also found a good match in the boundary conditions (private communication from Schubert).

2.5 The Boundary Conditions on the Lunar Surface

On the downstream side of the moon, all the components of the magnetic field and the two tangential components of the electric field must be continuous at the void/moon boundary. In addition, the normal component of the electric field must be zero just inside the moon since we assume the conductivity of the void to be exactly zero. But it should be noted that inside the void, on the lunar surface, a normal component of the electric field can exist due to a distribution of electric charge on the surface of the moon.

On the upstream hemisphere of the moon, the tangential electric and normal magnetic field components must be, as usual, continuous. Moreover, in the frequency range where lunar induction has been measured the hydromagnetic disturbance cannot propagate upstream in the solar wind. Thus, the above components of the field must assume essentially their unperturbed incident solar wind values on the sunlit surface of the moon. A partial check of these latter boundary conditions can be inferred from Figures 1.2 and 1.4 where we note that the amplification of the normal magnetic field component is indeed nearly equal to one on the upstream hemisphere of the moon. Another partial test of these boundary conditions is provided by comparing the data obtained from the Apollo 15 subsatellite to the one of Explorer 35 when both instruments were on the upstream side of the moon (Schubert, 1974a). Inherent in the above boundary conditions is the assumption that a surface current exists within a thin boundary layer above the lunar surface which shield the solar wind from any upstream influence of the moon. The Apollo 15 subsatellite magnetometer measurement, at an altitude of 100 km above the lunar surface did track rather well the unperturbed magnetic field observed at Explorer 35, but the tracking was not perfect. The level of the high frequency fluctuations ($f \gtrsim 0.01$ Hz) was often seen to be somewhat higher at the subsatellite than at Explorer 35. However, differences in the characteristics of each magnetometer could also account for some of the differences in the magnetic records. We should noted that an imperfect confinement of the induced field can also be surmised from the tendency of the amplification of the normal component of the magnetic field to fall slightly below unity in the high frequency range (Figure 1.2). The tracking of the field measured by the two satellites was often very poor when the subsatellite was near the terminator. But confinement near the terminator cannot be expected to be perfect since the dynamic pressure of the solar wind is nearly tangential to the surface in that region. We do not know yet to what extent the concept of perfect confinement should be relaxed in order to account for these observations. Nevertheless, this concept provides a good first-order approximation of the real boundary conditions.

Chapter III

Numerical Solution
Methods and Results

3.1 Introduction

The theory exposed in the last chapter can be applied whether or not the toroidal H field is an important contributor to the total magnetic field. However, when the toroidal H magnetic field can be neglected compared to the poloidal H magnetic field, the evaluation of the magnetic induction is simplified substantially. In the next section, we examine the feasibility of ignoring the toroidal field component in our calculations. We then proceed to describe in detail the numerical method we used to compute the magnetic field and to discuss some of the numerical error resulting from the truncation of our various series representations of the field. In the last section, some of the main characteristics of the computed response, as a function of the parameters of the source field, conductivity models and LSM position, are examined in some detail and compared with the data.

3.2 The Boundary Conditions and the Toroidal H Field

In Section 2.5, we mentioned six boundary conditions that the electromagnetic field must satisfy on the dark side of the moon and three more on the upstream side. However, classical theorems in electromagnetic theory (e.g., Müller, 1969) show that it is sufficient to impose the continuity of the two tangential components of the magnetic and electric field on the downstream side of the moon together with the continuity of the tangential E components on the sunlit side in order to fully determine the electric and magnetic field in each region of the lunar environment. Instead of embarking into a program that tries to systematically use these boundary conditions to compute the field, we examine their properties in some detail since they turned out not to be very convenient for the problem at hand. This will lead us to a more proper set of boundary conditions together with a somewhat simpler method of solution.

We first note that, due to the asymmetric plasma environment of the moon, we cannot extract from the boundary conditions at the lunar surface a subset pertaining to each electromagnetic mode, as was the case at the boundary of each internal layer inside the moon. Instead, they provide a coupling between these modes. However, this coupling might turn out to be poorly represented if the continuity of the tangential E and H components are used to find a numerical solution of the field. To illustrate this point, let us consider the continuity of the two tangential components of the magnetic field on the downstream side of the moon. In order to simplify the algebra, let us assume that the incident field has its normal parallel to the axis of the cylinder ($\psi = 0$ and say $H_{ox} = 0$, $H_o = 1$ in Equation (2.2.1). For $0 \le \theta \le \pi/2$ and supressing the common ϕ dependence, these boundary conditions can be written as follows:

a) Continuity of H_ϕ

$$\sum_n \left[a^1_{nl} L_n \frac{P^1_n(\cos\theta)}{\sin\theta} - \frac{b^2_{nl} T_n}{ik_{//} R_M} \frac{\partial P^1_n(\cos\theta)}{\partial \theta} \right]$$

$$+ \sum_\ell A^1_{\ell 1} \frac{J_1(\beta_{\ell 1} R_M \sin\theta)}{\beta_{\ell 1} R_M \sin\theta} e^{-\beta_{\ell 1} R_M \cos\theta}$$

$$= \left[\frac{I_o(k_{//} R_M \sin\theta) - I_2(k_{//} R_M \sin\theta)}{I_o(k_{//} R_M) + I_2(k_{//} R_M)} \right] e^{ik_{//} R_M \cos\theta}$$

b) Continuity of H_θ

$$\sum_n \left[a^1_{nl} L_n \frac{\partial P^1_n(\cos\theta)}{\partial \theta} - \frac{b^2_{nl} T_n P^1_n(\cos\theta)}{k_{//} R_M \sin\theta} \right]$$

$$+ \sum_\ell A^1_{\ell 1} \left\{ \frac{\cos\theta}{2} \left[J_o(\beta_{\ell 1} R_M \sin\theta) + J_2(\beta_{\ell 1} R_M \sin\theta) \right] \right.$$

$$\left. + \sin\theta J_1(\beta_{\ell 1} R_M \sin\theta) \right\} e^{-\beta_{\ell 1} R_M \cos\theta}$$

$$= \left\{ \frac{\cos\theta [I_o(k_{//} R_M \sin\theta) + I_2(k_{//} R_M \sin\theta)] - 2i\sin I_1(k_{//} R_M \sin\theta)}{I_o(k_{//} R_M) + I_2(k_{//} R_M)} \right\} e^{ik_{//} R_M \cos\theta}$$

In these equations we have used the cylindrical waveguide modes representation of the end effect field but the multipole expansion would not alter the following argument.

We note that if these two conditions were met exactly, we could operate on both sides of the first equation with $\frac{\partial \sin\theta}{\partial \theta}\cdot$ and subtract the second equation to obtain

For $0 \lesssim \theta \lesssim \pi/2$

$$\sum_n \frac{(n)(n+1)T_n P_n^1(\cos\theta)}{ik_{//} R_M} \sin\theta = 0$$

This last equaton is equivalent to imposing the constraint that the normal component of the electric field associate with the toroidal H mode is zero on the dark side of the moon. Thus we infer that the continuity of the two tangential magnetic field components inherently implies this condition. However, in practice, we can only satisfy these boundary conditions approximately, so the validity of this inference needs to be investigated from the numerical point of view. Let us consider the order of magnitude of the various terms in our two equations. The poloidal H and cylindrical TE field are either of the order of the incident field or of the order of the toroidal H field, depending on the one that dominates. An estimate of the toroidal field can be based on the data of Figure 1.2 which shows that the solar wind magnetic field is perturbed only slightly on the lunar surface at low frequencies. Because the amplitude of the toroidal H response should be maximum at low frequencies (see, for example, Sill , 1970), we infer that this field must be much smaller than the incident field over the whole frequency range. This last inference is given strength by the fact that the low frequency disturbance can also be attributed to either a small poloidal H signal or to noise which seems to indicate very low near-surface conductivity*. If the

---

*In our discussion, we have assumed that the relaxation time associated with charge diffusion ($\simeq \varepsilon_0/\sigma$) is much smaller than the period of interest. For example, at T=25 sec, we must have $\sigma >> 4 \times 10^{-14}$ mho/m. Strangway (1968) has suggested, however, that near surface conductivity on the moon might be as low as 10^{-13}-10^{-16} mho/m. In that case displacement current would dominate over the conduction current and not only the expression for the toroidal H field would have to be revised but also its associated boundary conditions.

toroidal H magnetic field is very small compared to the poloidal magnetic field we can not devise easily a numerical algorithm to match our four boundary conditions and at the same time conserve their independence. However, if we are interested in calculating only the magnetic field and are willing to accept an error in doing so of the order of the toroidal H magnetic field, we can simply drop the toroidal contribution from the continuity condition on the tangential magnetic field components. Then, using the tangential components in conjunction with the boundary conditions on the normal component of the magnetic field we can determine the magnetic field completely. This then seems to be the proper set of boundary conditions to use since solving simultaneously for the electric and magnetic field would only provide a correction of the order of the neglected toroidal H magnetic field which is likely to be small if not negligible.

3.3 Numerical Method and Precision of the Solution

As mentioned in the preceding section, the magnetic field can be completely described by matching only the boundary conditions associated with its tangential and normal components, neglecting terms involving the toiroidal H field. In order to obtain this solution numerically, we note first that, for each value of θ, each component of the field can be expressed in a Fourier series in the ϕ coordinate. The Equations (2.3.1), (2.4.1), and (2.4.2 or 2.4.3) are already in that form and we show in Appendix VI how the normal component of the incident solar wind magnetic field can also be expanded in such a series. Because of the orthogonality of these different harmonics, the partial field associated with a given pair (m,σ) in one region of the lunar environment needed only to be matched with the partial field associated with the same pair in another region. Consequently, the ϕ dependence can be suppressed from our boundary condition and we are left with the task of matching only their polar angle dependence, which we can do by writing down our boundary conditions at K different values of θ both on the sunlit and dark side of the moon and then use only a finite number of parameters to represent the poloidal H and "end effect" field associated with the pair (m,σ). The resulting system of equations can then be solved by the method of least squares. This process can be summarized by the following matrix equation:

$$C_{m\sigma}X_{m\sigma} = S_{m\sigma} \tag{3.3.1}$$

where, for reasons to be discussed shortly, the elements are distributed as follows:

1. The top J elements of the column of parameters $X_{m\sigma}$ are filled with the unknown coefficients of the end effect field $A^{\sigma}_{\ell m}$ (or t^{σ}_{nm}) and are followed by the coefficients of the poloidal H field (a^{σ}_{nm}).

2. The top 3K lines of $C_{m\sigma}$ are used to represent the difference between the end effect and poloidal H field of the three magnetic field components on the dark side of the lunar surface whereas we reserve the last K lines to represent the normal component of the poloidal H magnetic field on the sunlit side. We note that, though in theory we need to use only one component of tangential magnetic field, we found that in practice, a more uniform distribution of the truncation errors result when both components are used. (The case m = 0 is somewhat special since there is no H_{ϕ} component associated with this value of m, so only the continuity of H_{θ} and H_{r} are used in this case).

3. Our boundary conditions require that the top 3K elements of the column $S_{m\sigma}$ be filled by the matching values of the surface wave field whereas its last K elements are reserved to express the normal component of the incident solar wind magnetic field at the same K values of θ used on the left hand side.

By using a series of Householder transformation to solve Equation (3.3.1) by the method of least squares (see, for example, Golub, 1965), we realize a substantial economy in the computation when we exploit the following three properties of the elements of the first J column of $C_{m\sigma}$ (associated with the end effect field).

a) Each of these elements are real as compared to the generally complex value of the elements associated with the poloidal H mode.

b) The last K elements of each of these columns are filled with zeros since the sunlit side magnetic field does not involve the end effect field.

c) These elements are independent of both the frequency and the conductivity model used [as can be seen from Equation (2.4.2) or (2.4.3)].

This last property is especially useful when we need to evaluate the field at different frequencies and for different conductivity models since the Householder transformation associated with the first K columns may be saved and then used repeatedly in each of these cases.

Before investigating some properties of the field, we need to specify the numerical error associated with the various truncations in our series representation of the field and by our choice of a finite number of points to match its boundary conditions. With regard to this last point, we found that the field obtained by matching the boundary conditions at five degree intervals in the θ coordinate did not differ by more than 1% from the one computed if three degree intervals were used. Thus, the former choice was judged sufficient for our purposes. We therefore restrict our discussion to the error arising from the following two main types of truncation:

1. A truncation in the number of Fourier harmonics ($m = 0, 1, \ldots, M$). We discuss the criteria used to effect this truncation in Appendix VI and show that a relative error of less than a few percent should result.

2. For each Fourier harmonic specified by a pair (m,σ) we need to truncate the series representations of the poloidal H and end effect field.

Before proceeding to discuss this last point, we should mention that various other types of truncation are generally required to evaluate each element of the matrices $C_{m\sigma}$ and $S_{m\sigma}$ (e.g., truncation in the series representation of a given function). Their associated error, however, can be rendered negligible compared to the ones above by using sufficiently accurate algorithms.

Let us define the following two measures of the relative mismatch in the boundary conditions arising from our choice of a finite number of unknowns to represent the poloidal H and "end effect" field.

$$R_{1i}^{m\sigma}(\theta) = \frac{\left| a_i^{m\sigma} - b_i^{m\sigma} \right|}{\left| a_i^{m\sigma} \right|}$$

$$R_{2i}^{m\sigma}(\theta) = \frac{\left| \left| a_i^{m\sigma} \right| - \left| b_i^{m\sigma} \right| \right|}{\left| a_i^{m\sigma} \right|}$$

where $a_i^{m\sigma}(\theta)$ = the i component of the poloidal H field on the lunar surface ($i = r, \theta, \phi$) associated with the (m, σ) harmonic

$b_i^{m\sigma}(\theta)$ = 1) On the dark side: the i component of the surface wave plus end effect field on the lunar surface associated with the (m,σ) harmonic

2) On the sunlit side: the i component of the incident solar wind magnetic field on the lunar surface associated with the (m,σ) harmonic.

Using the triangle inequality, we can show easily that $R_{1i}^{m\sigma}(\theta) \geq R_{2i}^{m\sigma}(\theta)$.

To illustrate the resulting mismatch in the boundary condition we shall concentrate on the case when the incident field has its normal parallel to the axis of the cylinder (and, say, $H_{ox} = 0$). This source field involves only the pair $(m,\sigma) = (1,1)$, but the results are typical of those obtained for other values of m. We shall show shortly that, for a given number of field parameters to represent the field, the mismatch tends to increase with frequency. Thus, we shall examine in detail only the high frequency case, $f = 0.04$ Hz, thereby setting an upper bound to the error we might expect. The mismatch also depends to some extent on the conductivity model used. The results discussed below are typical of models that give good fits to the data but other models used in the text generally will agree with this error estimate to within a factor of 2.

We illustrate in Figure 3.1 the result obtained when the poloidal H and end effect field are represented by 10 unknowns each. The H_ϕ component on the dark side is shown together with the two measures of the mismatch defined above (dot for $\log R^{11}_{2\phi}$). We note that either measure is indicative of a relative error of less than 1%. The mismatch in the H_θ component is examined in Figure 3.2. This time, however, both measures of the mismatch are $\log R^{11}_{1\theta}$ but the dot displays the relative error obtained when 15 parameters are used to represent each field (instead of 10 for the square). Though this increase in the number of parameters reduces the relative error by about

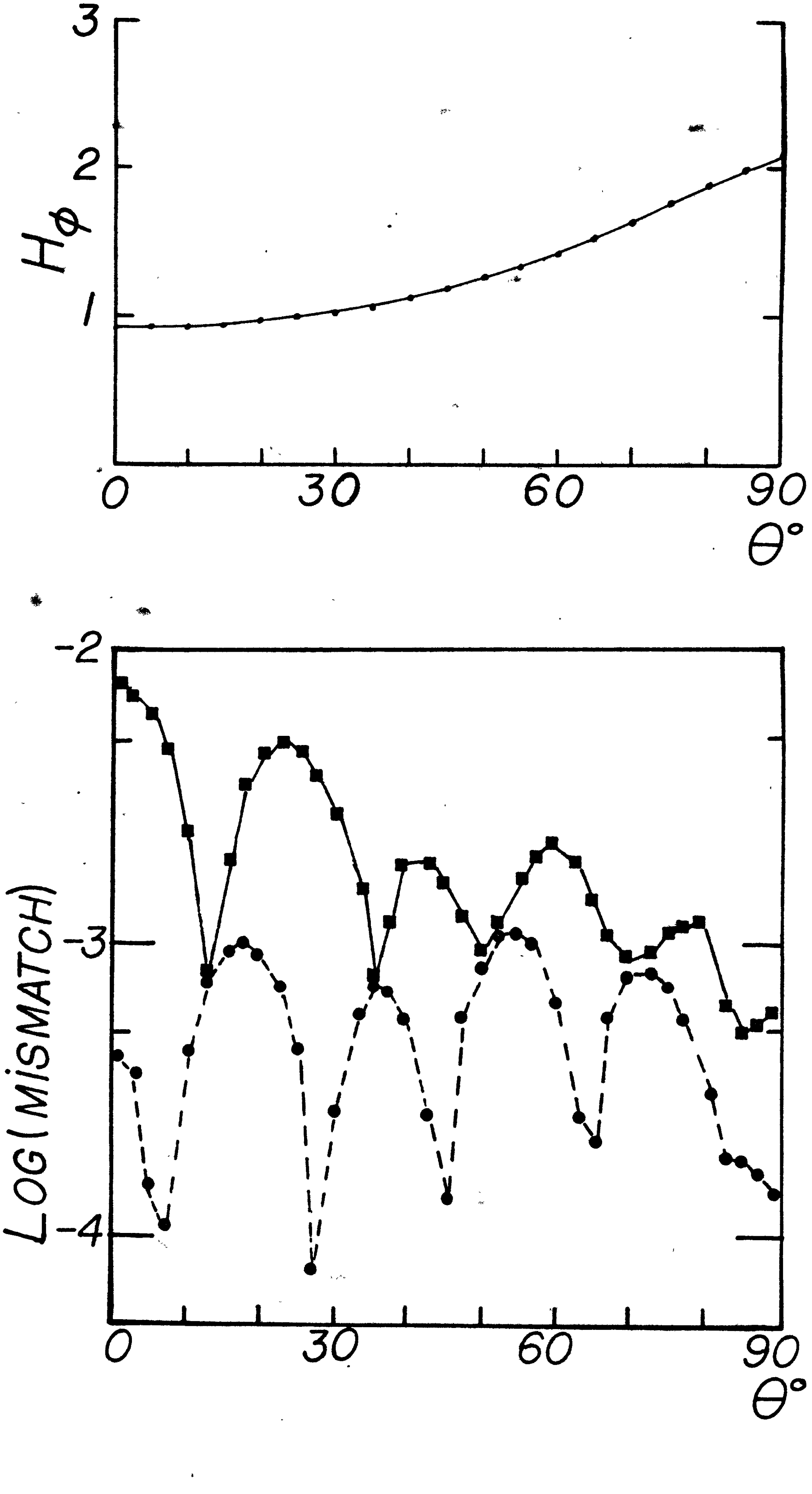

Figure 3.1

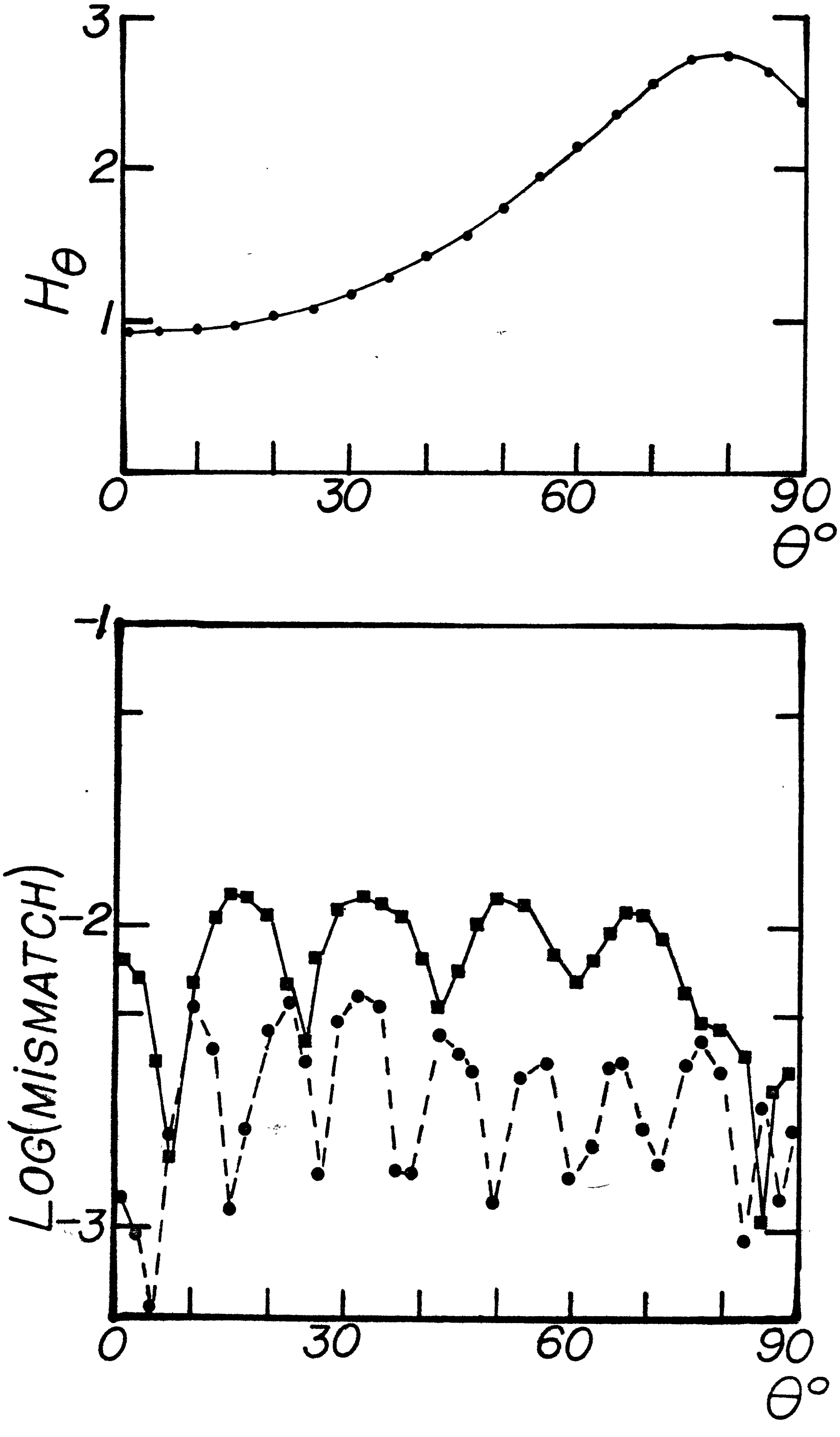
3
2
1
H_θ
0
30
60
90
θ°
-1
-2
-3
LOG(MISMATCH)
0
30
60
90
θ°

Figure 3.2

a factor of 2, the 1% accuracy obtained with the smaller number of parameters was considered sufficient for our purpose.

We have not distinguished above which of our two "end effect" field representation was used. The reason for this is made plain in Figure 3.3 where we illustrate the results obtained from both expressions. In each case, ten parameters were used to express the "end effect" and poloidal H field and the measure of the mismatch shown is R_{2r}^{11} . The relative error using the multipole expression [Equation (2.4.3)] is represented by the dots whereas the triangles exhibit the one obtained when the cylindrical waveguides mode [Equation (2.4.2)] are used. Not only is the error in both cases nearly identical, but also the computed field does not differ by more than 1% (approximately the radius of the dot in the upper figure). Moreover, similar results were obtained for the other components of the field. These results suggest two conclusions. First, though in our argument in the last chapter we suggest that the multipole representation is theoretically more adequate for the problem at hand, the numerical results do not support this contention. Indeed, the closeness of the computed field using either mode of expression hinted that they are merely equivalent

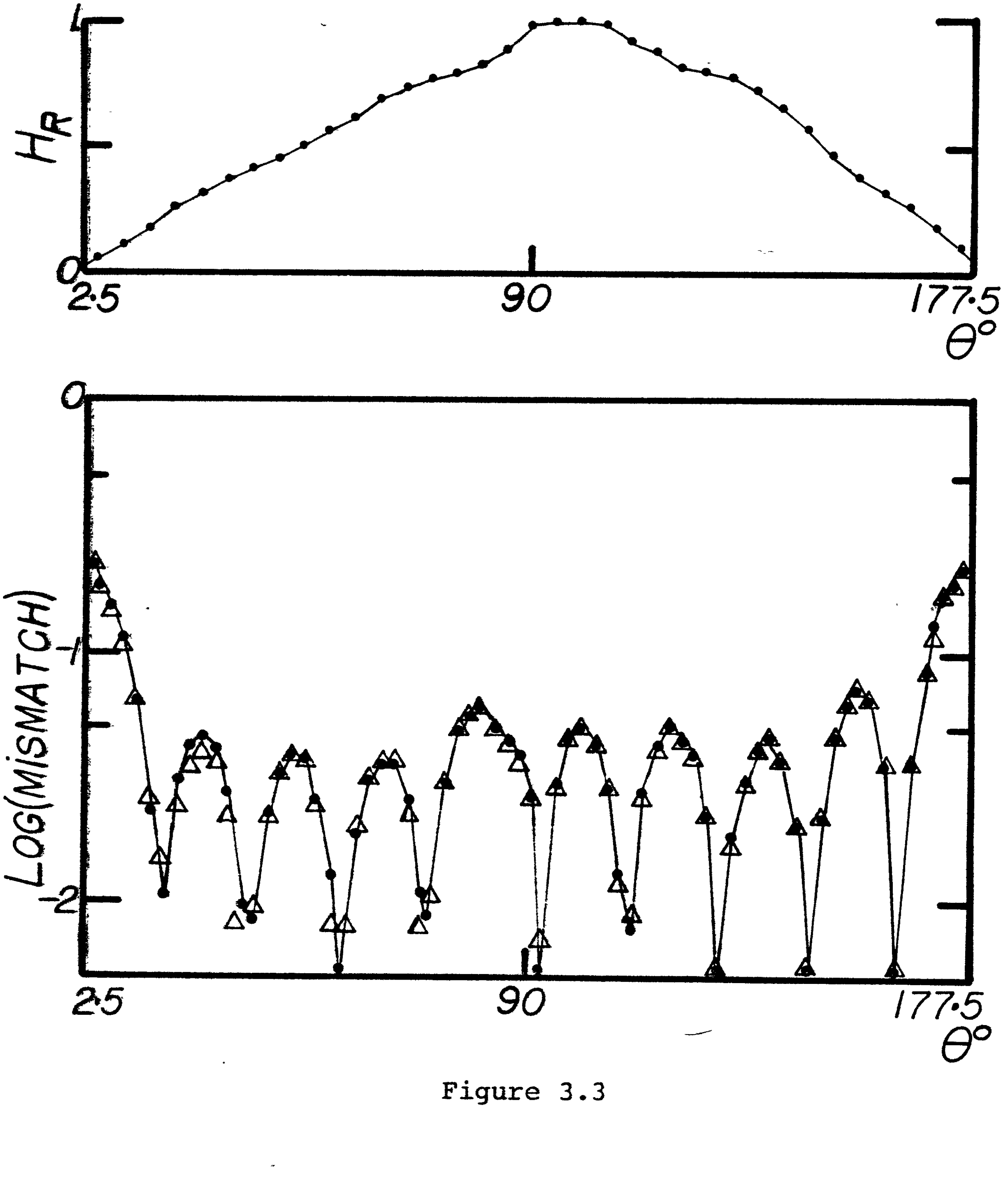

Figure 3.3

ways of expressing the field and that the Rayleigh assumption embodied in the cylindrical waveguide mode expression is justified. Secondly, the closeness of the relative error to each representation in addition to the fact that their amplitudes are approximately the same on the sunlit and dark side of the moon suggest that the truncation in the poloidal H expansion is the more important contributor to the mismatch. In other words, for a given number of parameters, the error can probably be reduced by using more parameters in the poloidal H field representation than in the "end effect" field representation. This could have been anticipated on the basis of the important role the day/night asymmetry ought to play in the computed response.

Since the 5% relative error in the radial component relative error in the radial component shown in Figure 3.3 has little consequence on our future results, all the calculation in this work (except one to be mentioned in the next section) were done using ten parameters to represent the end effect and poloidal H field. We should keep in mind that the relative error illustrated in the preceding three figures are upper bounds on what we can expect in the frequency range of interest. We show in Table 3.1 typical results obtained at lower frequencies for the same number of parameters as quoted above.

Table 3.1

Relative Error

f (hertz)	$R^{11}_{2\phi}$ %	$R^{11}_{2\theta}$ %	R^{11}_{2r} %
0.0002	0.005	0.05	0.05
0.002	0.05	0.5	0.7
0.02	0.1	0.8	3

Though we can deduce from this table that, at low frequencies, an acceptable precision can be reached with a substantially lesser number of parameters to represent the field, we did not use this option in the work.

3.4 Properties of the Field

The data presented in the first chapter (and in Section 2.3), depend not only on the internal electrical conductivity of the moon but also on:

1. The detailed characteristics of the source field,
2. The exact position of the magnetometer measuring the field on the lunar surface,
3. The presence of noise associated with processes not accounted for by the theory.

Unfortunately, the data are averages over an unknown distribution of these parameters. In addition, an empirical correction was applied on the sunlit side of Apollo 12 data to account for what appears to be a noise associated with the presence of a substantial remanent at this site although a theoretical foundation for this correction is still lacking. Therefore we proceed to illustrate to what extent the measured and computed response are sensitive to these various parameters and noises in order to gain insight into the correctness and limitation of the assumptions we shall use in the inversion process

Figure 3.4: We show here the A_{min} value discussed in Section 2.3 and A_z data (from Figure 1.2) foth of which were collected at the Apollo 12 site when the LSM was on the sunlit side of the moon. Also shown is the computed field at the subsolar point using the symmetric plasma assumption (dot) and our more accurate calculation involving the asymmetric plasma environment (◇).

In both cases the three-layer model given below was used.

Radius (km)	σ (mho/m)
0 - 1206	1.9×10^{-3}
1206 - 1527	5.12×10^{-4}
1527 - surface	1.0×10^{-11}

This model was obtained by Sonett *et al.* (1972) as

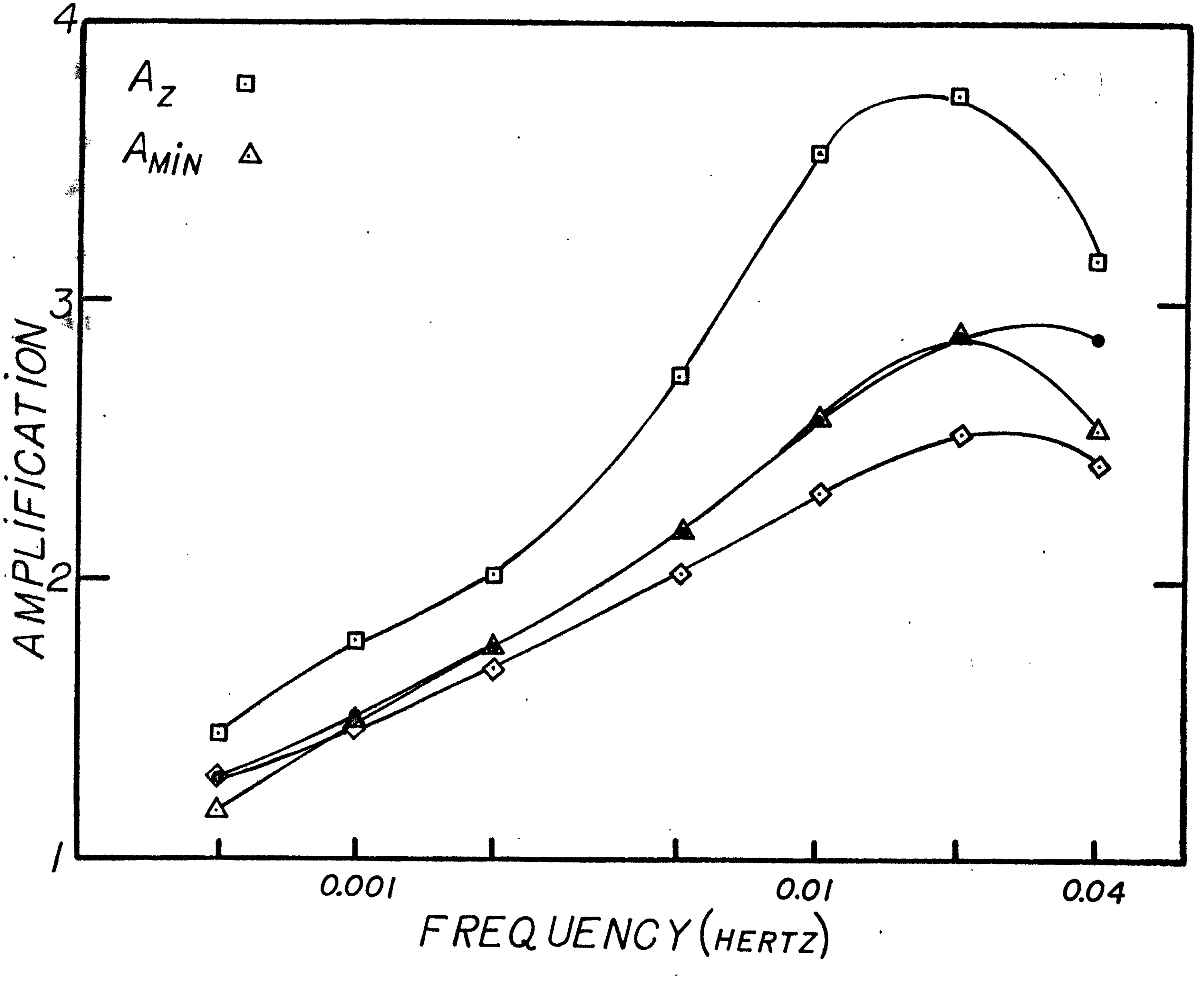

Figure 3.4

a member of a set giving a good fit to the A_{min} value when using the symmetric plasma assumption to invert the data. The source field used is impinging normal at the subsolar point (i.e., $\psi = 0$), and the solar wind velocity used was 400 km/sec.

We note that the inclusion of the void region behind the moon substantially lessens the predicted lunar response on the sunlit side, especially at the shorter period. This effect occurs mainly because the confinement current on the boundary of the cylinder is less efficient than the one inherent in the symmetric plasma model in amplifying the front side response. In order to build up the response to the A_{min} values, a higher conductivity distribution is required near the lunar surface. However, we also note that the extraction of the A_{min} values from the sunlit side data involve a relative correction much larger than the correction associated with the introduction of the void region behind the moon. Thus, though our theoretical refinement does permit unification in a single framework of both the sunlit and dark side responses, its ultimate superiority over the symmetric plasma theory in obtaining an accurate lunar conductivity model is largely dependent on the accuracy of the correction made to obtain the A_{min} values.

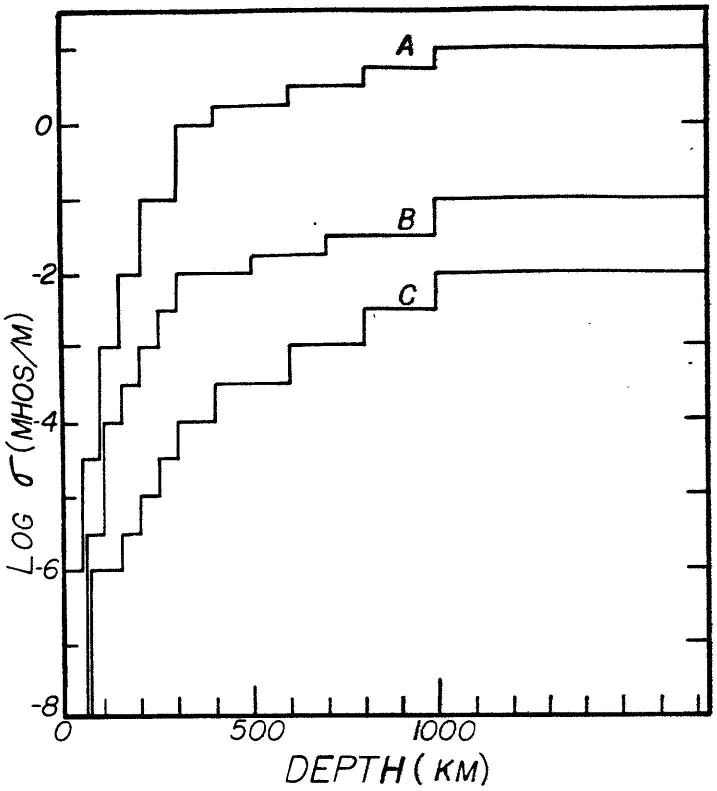

Figure 3.5: This is a plot of three models proposed by Ward (1969) as a guide for the range of conductivity expected inside the moon. He bases his estimate of the model labelled "B" on a lunar temperature model proposed by Fricker et al. (1967) and assigns a conductivity at a given depth consistent with the value realized in the earth's mantle at the temperature characteristic of this depth. Due to various uncertainties associated with this correlation, Ward proposed models A and C as reasonable error bounds. Actually these bounds are wide enough to embrace not only all the models giving a good fit to the electromagnetic data but also practically all the models based on the various lunar temperature distribution, composition, and conductivity-temperature relationship proposed in the literature. Thus,

Ward's models formed a good starting point to investigate the sensitivity of the data to the conductivity distribution.

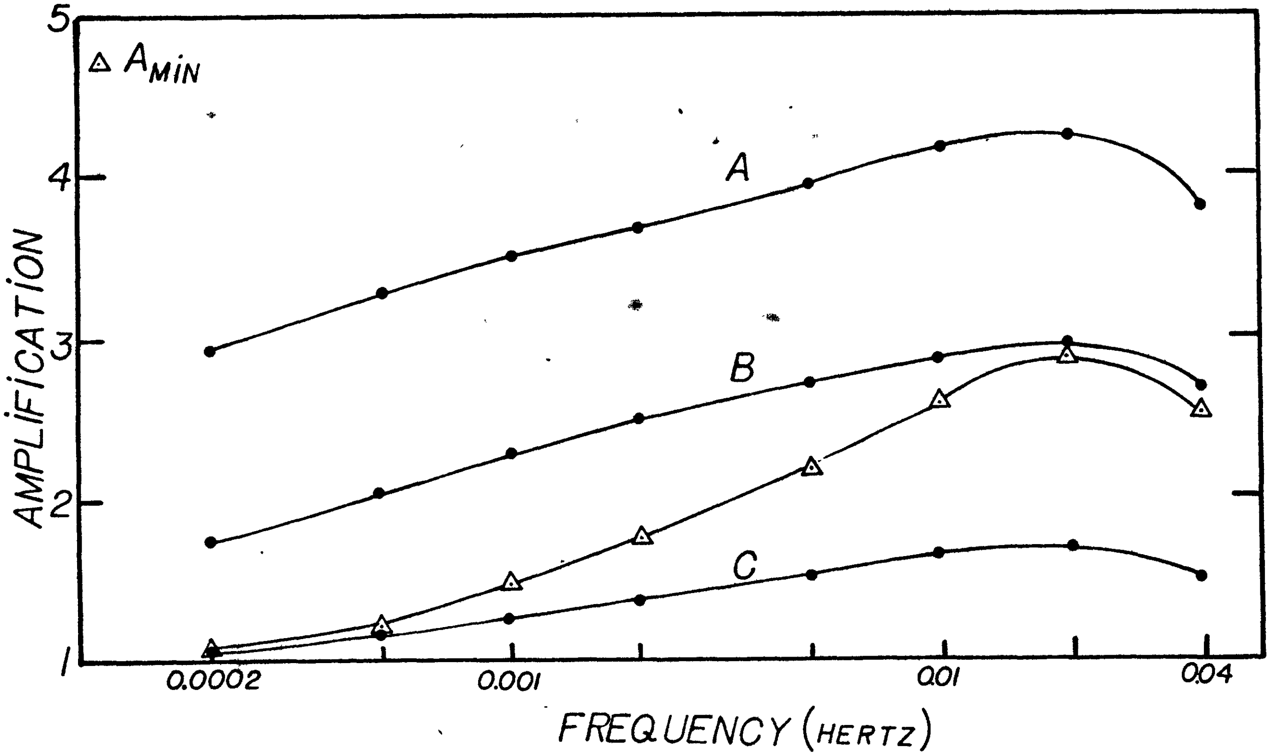

Figure 3.6: We show the subsolar point response of the preceding three models as a function of frequency, when the source field parameters are $\psi = 0$ and $V_{SW} = 300$ km/sec. Also plotted are the A_{min} values*.

---

*In all the following plots of amplification vs. frequency, the frequency scale is logarithmic and the response was computed at the frequencies specified by the ticks on the bottom scale. These are: 0.0002, 0.0005, 0.001, 0.002, 0.005, 0.01, 0.02, 0.04 Hz. In some graphs, the lowest frequency is omitted.

The low frequency response is indicative of a deep lunar conductivity similar to that of model C, whereas the high frequency response is indicative of a conductivity structure at shallow depths similar to that of model B. Thus, we infer a moon of fairly homogeneous conductivity between about 10^{-4} to 10^{-2} mho/m below approximately 100 km covered by a fairly resistive layer. A more explicit description of the conductivity structure will be found in the next chapter.

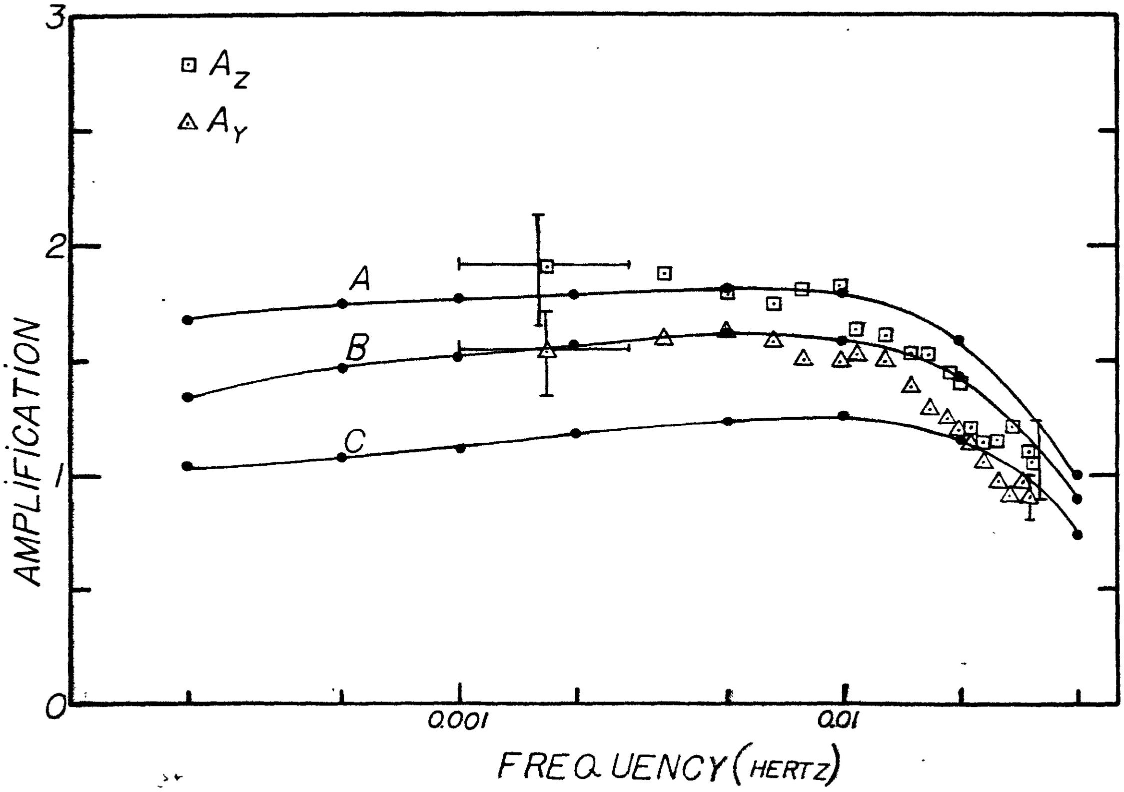

Figure 3.7: The same source parameters and three conductivity models discussed above are used here to compute the antisolar point tangential response.

Clearly, the large errors associated with these data and their limited low frequency coverage range render them far less useful than the more extensive sunlit side data in discriminating between conductivity models. To make matters even worse, as we shall see shortly that the high frequency data (above approximately 0.005 Hz) is very sensitive to the parameters of the source field and LSM position. Nevertheless, the two data points at the lowest frequency might be symptomatic of a difficulty associated either with the theory or a source of noise unaccounted for by it. We note that, from this and the preceding figure, the computed antisolar point response is distinctly smaller than the one at the subsolar point (by a factor of about 1.6 at this frequency for model B). Yet the two data points at 0.0017 Hz do not seem to bear this out. Indeed, the A_y value is only about 1.1 times smaller than the A_{min} value at this frequency, whereas the A_z value is actually 1.1 times greater. However, due to the large uncertainties associated with these measurements, we refrain from drawing definitive conclusions as to their consequences.

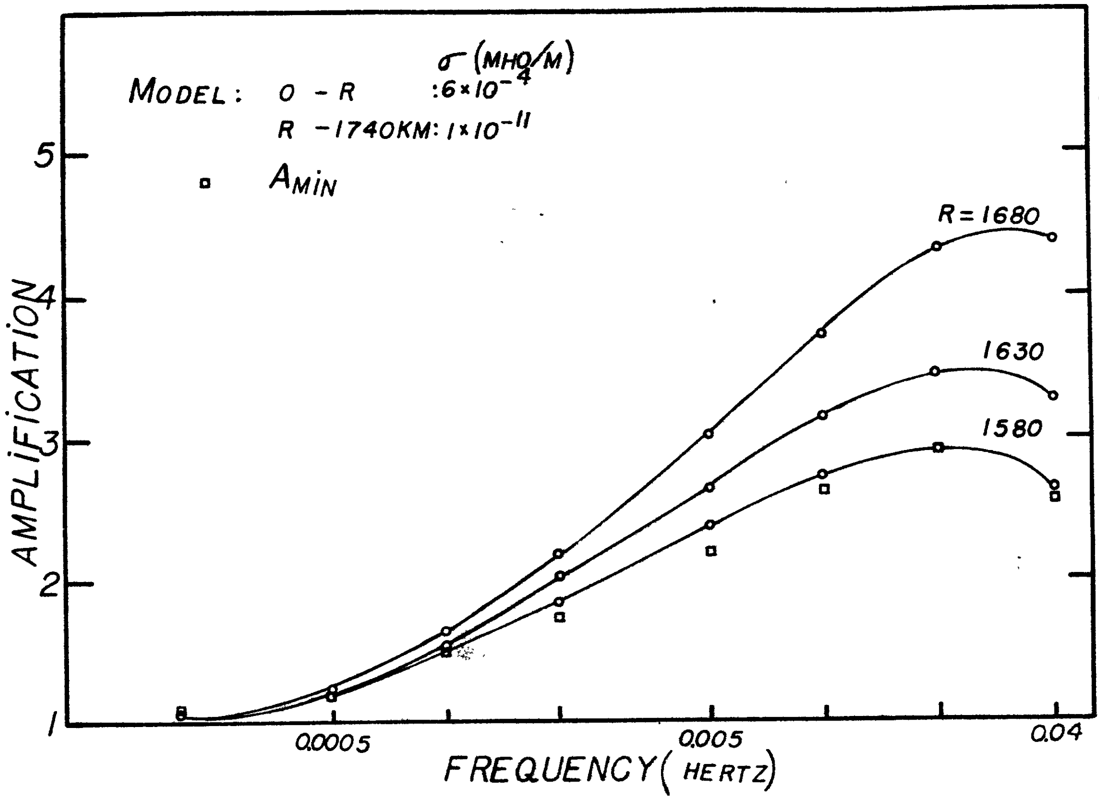

Figure 3.8: We illustrate here the great sensitivity of the subsolar point response to the shallow depth conductivity structure. The source field was again specified by $\psi = 0$ and $V_{SW} = 300$ km/sec and the three conductivity models used are detailed in the figure. We note that the model exhibiting a conductivity region to about nine-tenths of the lunar radius (1580 km) agrees fairly well with the A_{min} values. Actually, this model was proposed by Kuckes (1971) in an attempt to fit the sunlit side A_z and A_y data using the symmetric plasma theory. Although the asymmetric theory lessens the computed response obtained through the symmetric theory, the A_{min} data are also lesser than the A_z and A_y data,

thus leading in each case to a similar conductivity model.

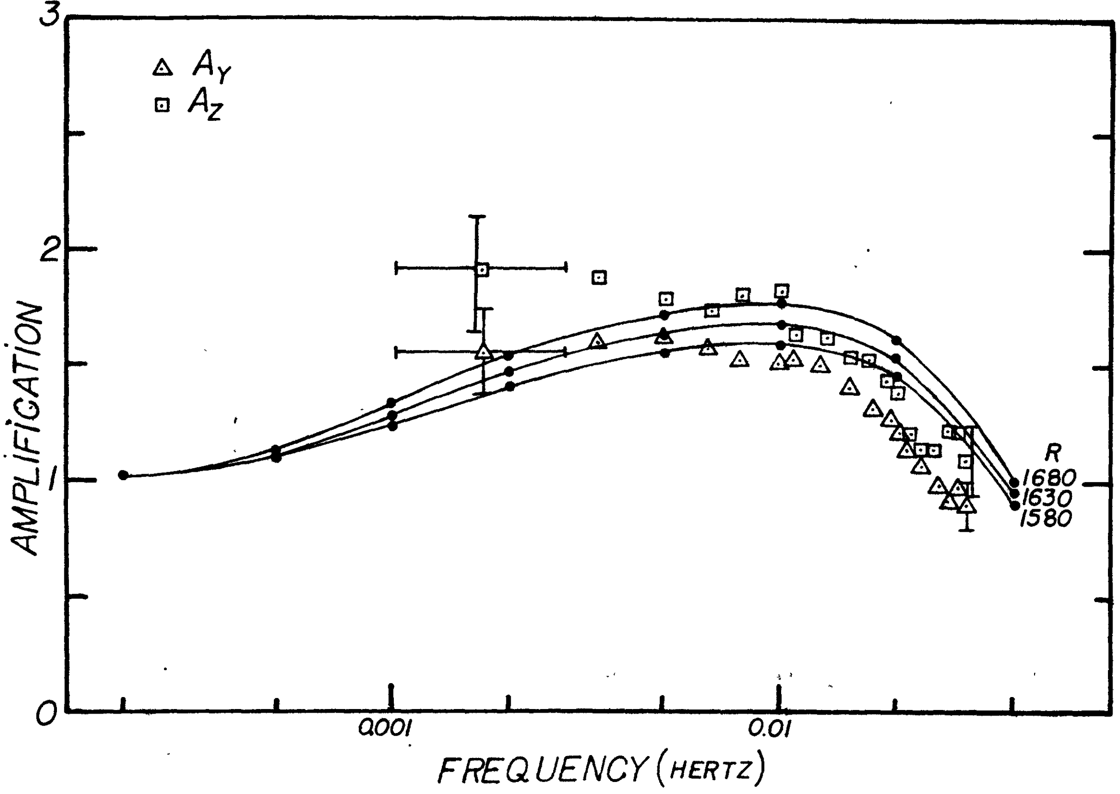

Figure 3.9: This is a plot of the antisolar point response for the source parameters and model described in the preceding figure. The large uncertainties associated with the measurements render them practically useless to discriminate between these three different conductivity models.

Before going any further, let me interject a few general remarks.

Since the LSM at the Apollo 12 site is situated at 2.95° S latitude in selenographic coordinates, negligible errors result if we assume it to be in the equatorial plane. An immediate consequence of this location is that the north-south, east-west, and vertical data values (A_z, A_y, A_x) correspond respectively to the computed A_ϕ, A_θ, and A_R amplification factors. However, it should be pointed out that since the computed A_ϕ, A_θ, and A_R can depend on the angle ϕ, the equality will be met, in general, only when the wave normal is in the equatorial plane. We did not differentiate in the preceding plot which angle ϕ and which component A_θ or A_ϕ was used. This is because when the incident field has its normal parallel to the axis of the cylinder, one can easily show that the amplification is isotropic at the subsolar and antisolar point. As a matter of fact, we can also show that, for this source field, the three amplification factors are independent of the angle ϕ for a general value of θ, though the two tangential amplification factors need not be isotropic in that case.

In the remaining graphs in this chapter, we shall try to illustrate some aspects of the dependence of the computed response on the parameters of the source and LSM position. Though these results also depend on the particular conductivity models used, a very good general idea can be gained by considering only one structure. In order that the results remain relevant for future work, we have chosen the model detailed in Table 3.2. This model turns out to give our best fit to the A_{min} value at the subsolar point, when the source field is specified by $\psi = 0$ and $V_{SW} = 300$ km/sec.

Table 3.2

Conductivity Model

Lunar Radius (km)	σ (mho/m)
1020	0.11×10^{-2}
1220	0.81×10^{-3}
1320	0.15×10^{-3}
1420	0.92×10^{-3}
1520	0.51×10^{-3}
1570	0.23×10^{-3}
1620	0.11×10^{-3}
1670	0.42×10^{-4}
1730*	0.1×10^{-10}

*1730 km was used instead of 1738 km but this has little consequence.

We shall also concentrate our attention only on the response obtained in the plane formed by the wave normal and the axis of this cylinder. This distinction is irrelevant when $\psi = 0$ but in other cases I shall call this plane the plane of incidence. By symmetry, the H_ϕ field in that plane depends only on the polarization specified by H_{ox} in Equation (2.2.1) whereas the H_θ component depends only on the H_o polarization. For convenience, we shall assume both polarities to have unit amplitude (i.e., $H_o = H_{ox} = 1$).

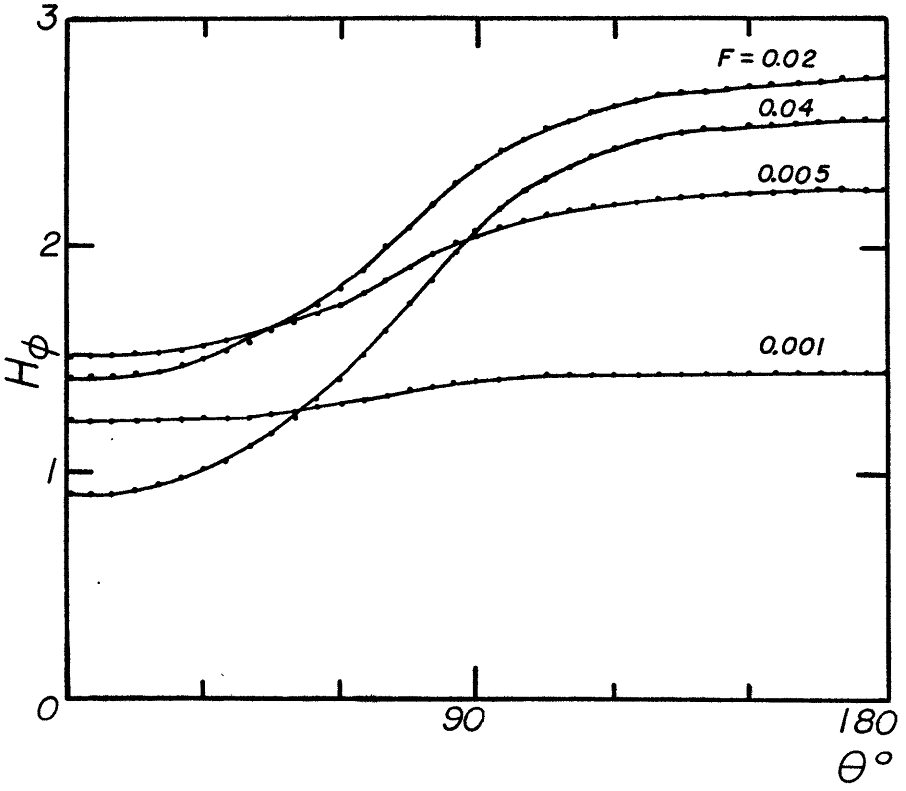

Figure 3.10: This is a plot of the absolute value of the ϕ component of the magnetic field vs. the polar angle θ ($\theta = 0$; antisolar point), for different frequencies. The source field is specified by $\psi = 0$ and $V_{SW} = 300$ km/sec. Because of our previous assumption, the power in the ϕ component of the source field is unity in the plane of incidence so the H_ϕ component is also directly the A_ϕ amplification factor.

The day-night asymmetry in the calculated response is clearly evident in this figure. However, we note that the transition between the two responses is fairly sharp but occurring mainly on the dark side of the moon. Thus we are left with a fairly extensive region near the subsolar point where the response is practically independent of position.

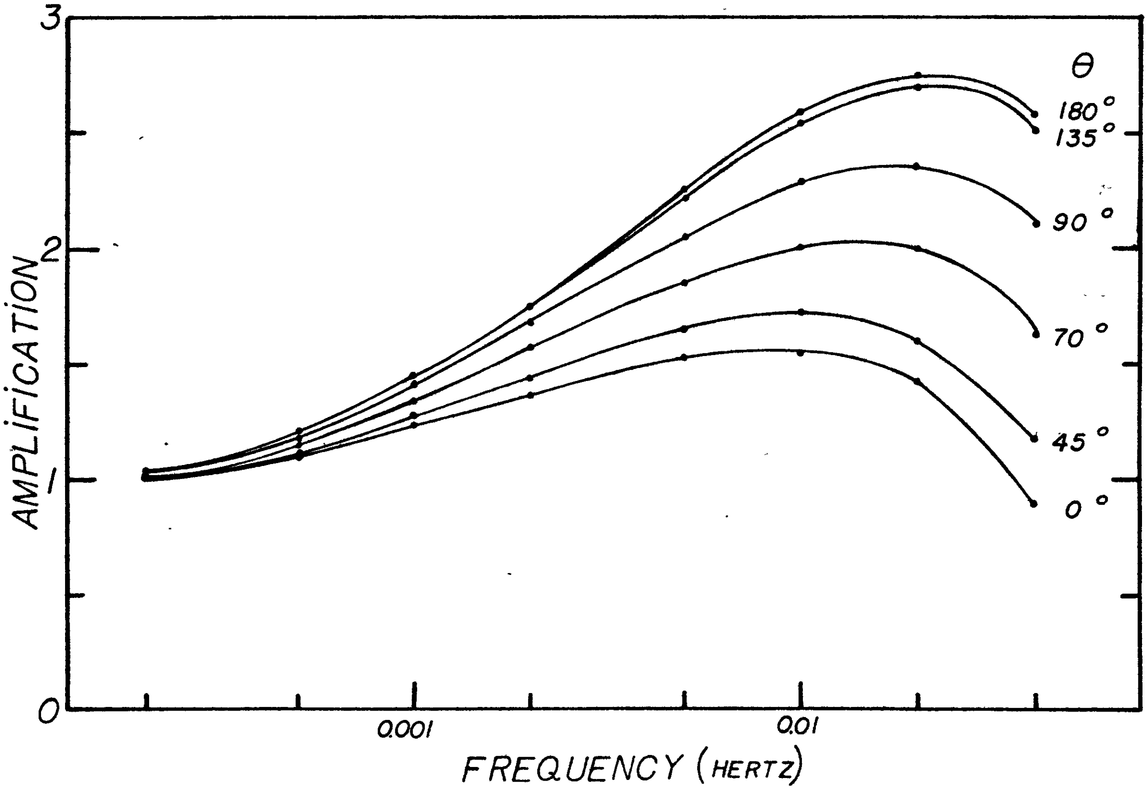

Figure 3.11: This is a plot of the same A_ϕ as the preceding figure but this time as a function of frequency and for selected values of θ. Note that within 45° from the subsolar point the amplification does not differ by more than a few percent. However, at 0.04 hertz and at 45° from

the antisolar point the response can reach a value of 25% higher than the response at the antisolar point. highest frequency.

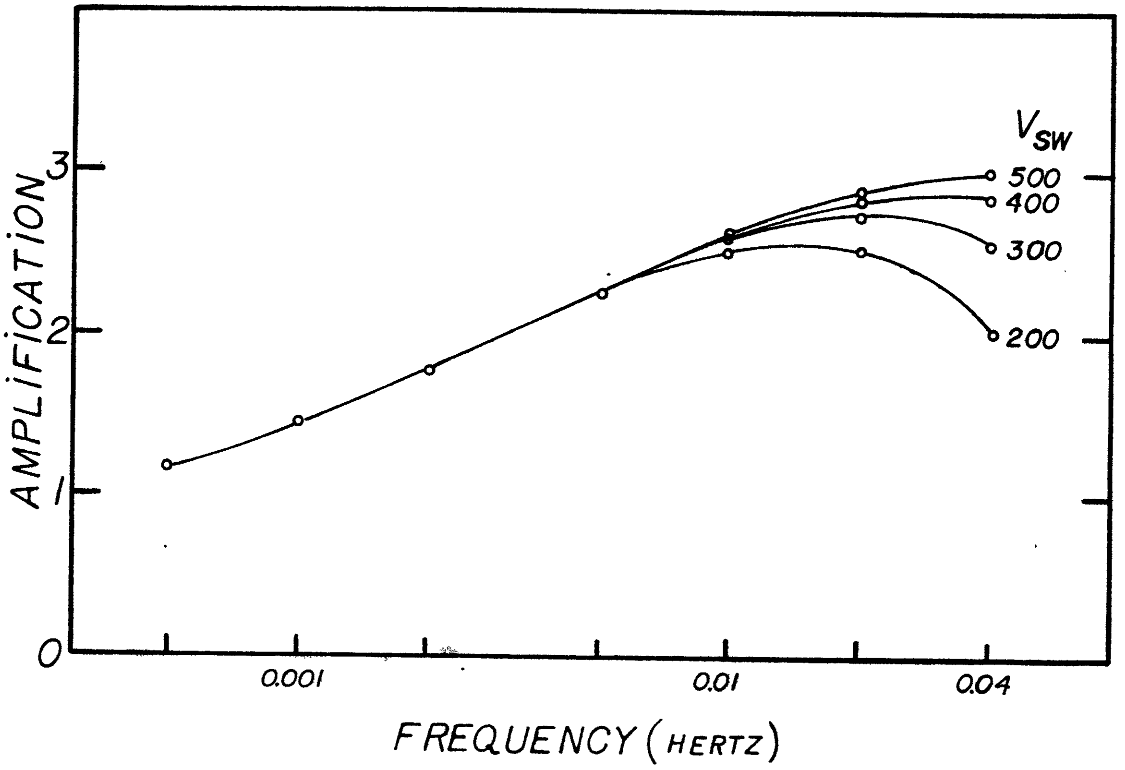

Figure 3.12: This is a plot of A_ϕ at the subsolar point for $\psi = 0$ and various solar wind velocities A decrease in solar wind velocity tends to depress the high frequency response.

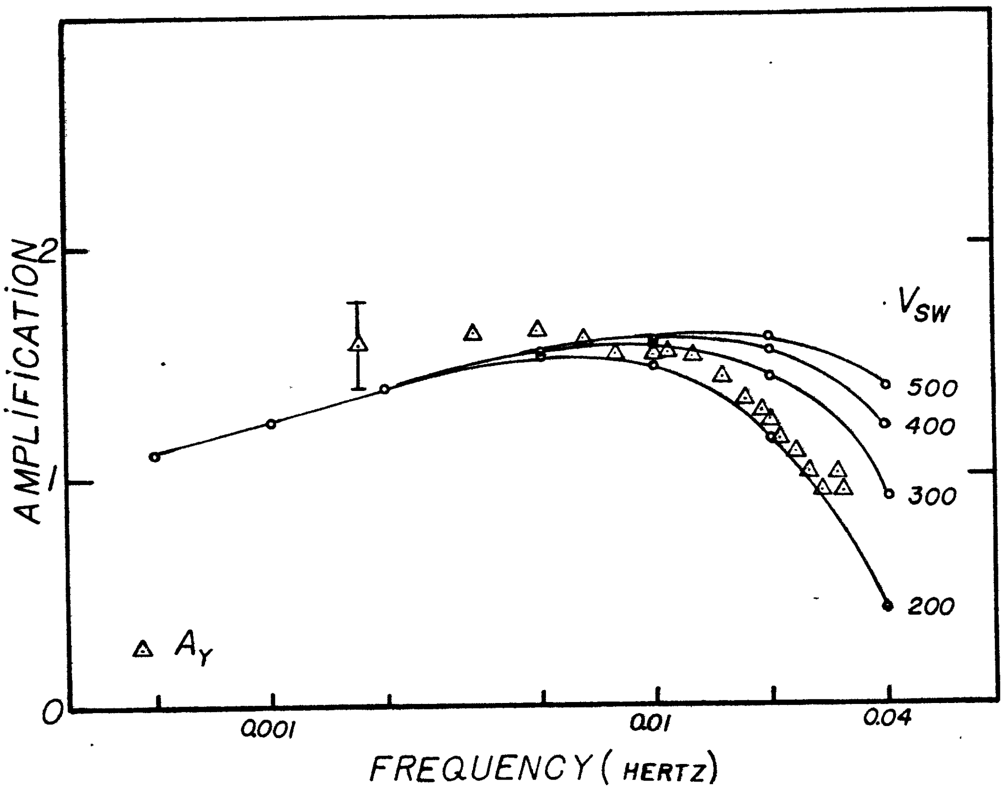

Figure 3.14: The antisolar point A_ϕ response is illustrated here for different solar wind velocities but for an angle of incidence specified by $\psi = 0$. If we compare the high frequency response to the response presented in Figures 3.7 and 3.8, we note that the solar wind velocity can be a more important factor than the conductivity in controlling the high frequency response.

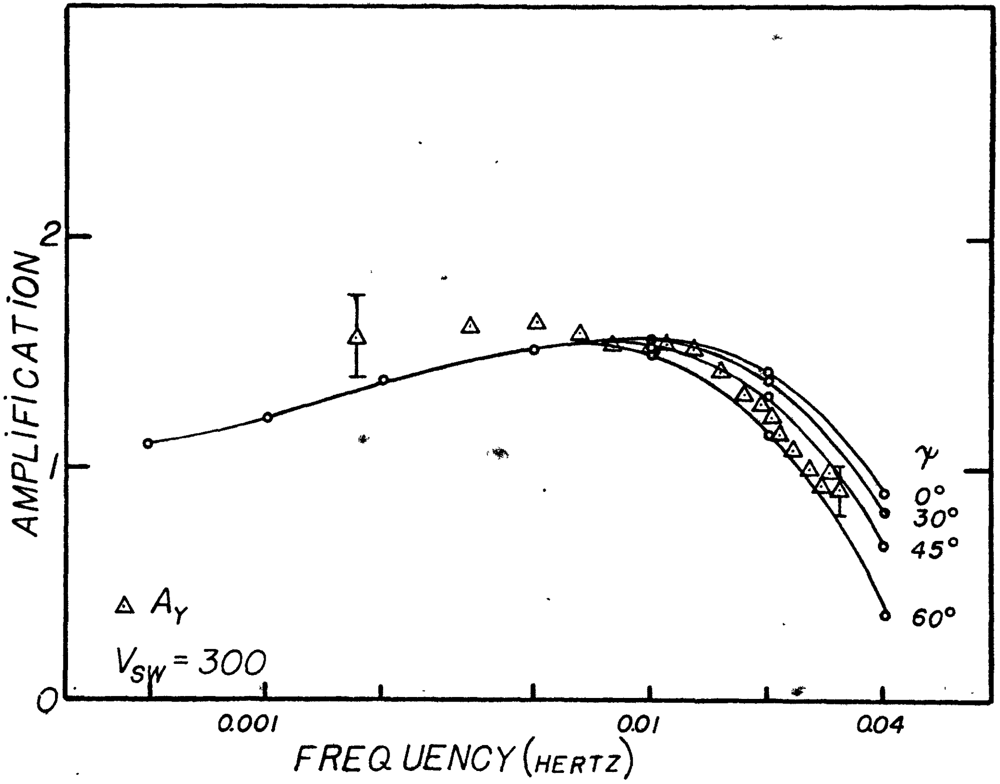

Figure 3.15: This is a plot of the antisolar point A_ϕ response for a solar wind velocity of 300 km/sec and various angles of incidence. Again we note that an increase in the angle of incidence tends to produce a similar effect to that of a decrease in the solar wind velocity.

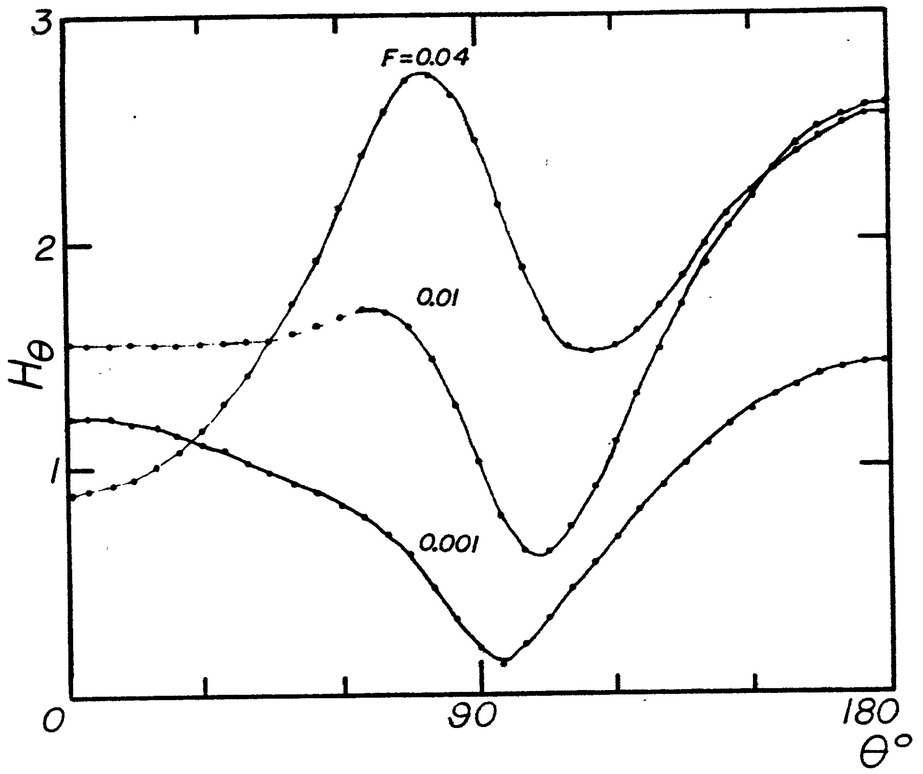

Figure 3.16: This is a plot of the absolute value of the θ component of the magnetic field vs. the polar angle. The incident field is characterized by $\psi = 0$ and $V_{SW} = 300$ km/sec.

The peak that developed near the terminator ($\theta = 90°$) at high frequencies is due in part to the distortion of the incident field by the surface wave. A component along the axis of the cylinder is associated with the surface wave even though the incident field has no component in that direction. This component becomes an important contributor to the total field at high frequencies especially near the boundary of the cylinder.

The H_θ component of the field is not directly the A_θ amplification since the power of the incident field has a $\sin^2\theta$ dependence on the polar angle. Consequently one must divide H_θ by $\sin\theta$ to obtain the θ amplification factor. But this involves a division by 0 and a resulting infinite amplification at the terminator. However, this problem is somewhat artificial since it arises solely because we assume the incident field to have no power along a given direction. In an actual situation the incident field has power in every direction though its distribution can be highly anisotropic (see Belcher *et al.* for a discussion of this point). In order to counter this difficulty to some extent, we shall henceforth consider only tangential amplification at least 45° from the assumed direction of zero power in the incident field. We think this procedure provides us with a fairly accurate picture of the actual amplification though we have not proven rigorously this assertion

Before going to the next figure, we recall that when the source has its normal parallel to the axis of the cylinder, the amplification is isotropic at the subsolar and antisolar point. Consequently, no change results if, in Figures 3.12 and 3.14 the A_ϕ amplification factor is replaced by A_θ.

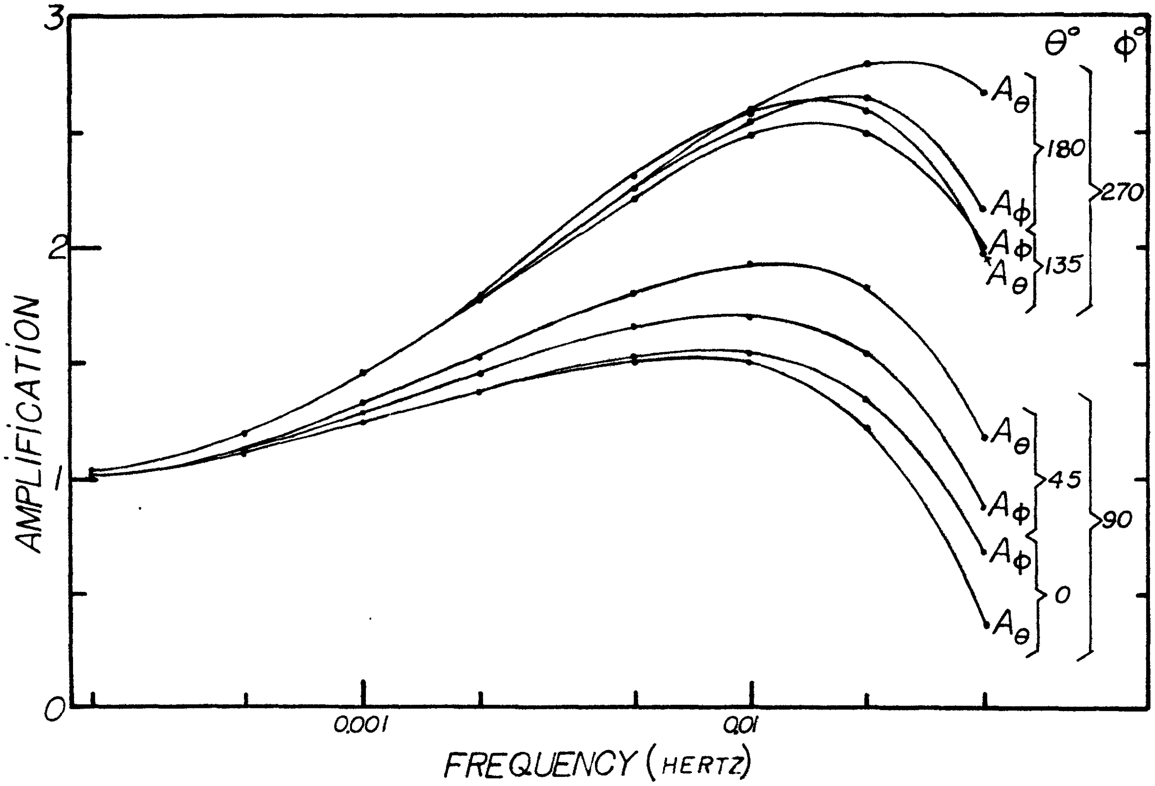

Figure 3.17: In this plot, the source field is specified by ψ = 45° and V_{SW} = 300 km/sec.

Let us consider first the curves representing the sunlit side response. If we compare the above A_θ response at the subsolar point with the subsolar point response for $\psi = 0$

(from Figure 3.12), we notice about a 5% increase in the computed response at high frequencies. Thus, in contrast to the A_ϕ response, an increase in the angle of incidence tends to increase somewhat the subsolar point A_θ response. When $\psi = 45°$, the response is anisotropic at the subsolar point with the A_θ response somewhat larger than the A_ϕ response at high frequencies. There is still a small anisotropy at 45° from the subsolar point ($\theta = 135°$) but it does not amount to more than about 5% though it is still A_θ that generally dominates the A_ϕ response. Based on these preliminary results, we would expect anisotropy to be observed on the sunlit side with A_θ generally larger than A_ϕ. However, if we examine the data of Figure 1.2, we see that A_z (i.e., A_ϕ) is generally higher than A_y (i.e., A_θ) except at high frequencies. However, at low frequencies, the remanent field seems to play an important role in determining the anisotropy. Thus we cannot conclude at this point that our preliminary calculations are contradicted by the observations.

By comparing Figures 3.15 and 3.17, we note that at the antisolar point, A_θ, like A_ϕ, tends to decrease with an increase in the angle of incidence. When $\psi = 45°$, the computed response at the anitsolar point and at 45^0 from it has a somewhat mixed character, at the antisolar point A_ϕ dominates while at 45^0 from the antisolar point A_θ is the larger of the two components. Due to the order of magnitude of the differences involved, however, we would suspect that A_θ is generally the larger response for data taken within the first 45^0 from the antisolar point. On the other hand, the data of Figure 1.3 exhibits values of A_z larger than A_y, contrary to our expectations, and we cannot here involve the remnant field to explain this divergence. But since the mean square errors associated with the average value of the measurements overlap each other, these uncertainties preclude any definite conclusion at this stage.

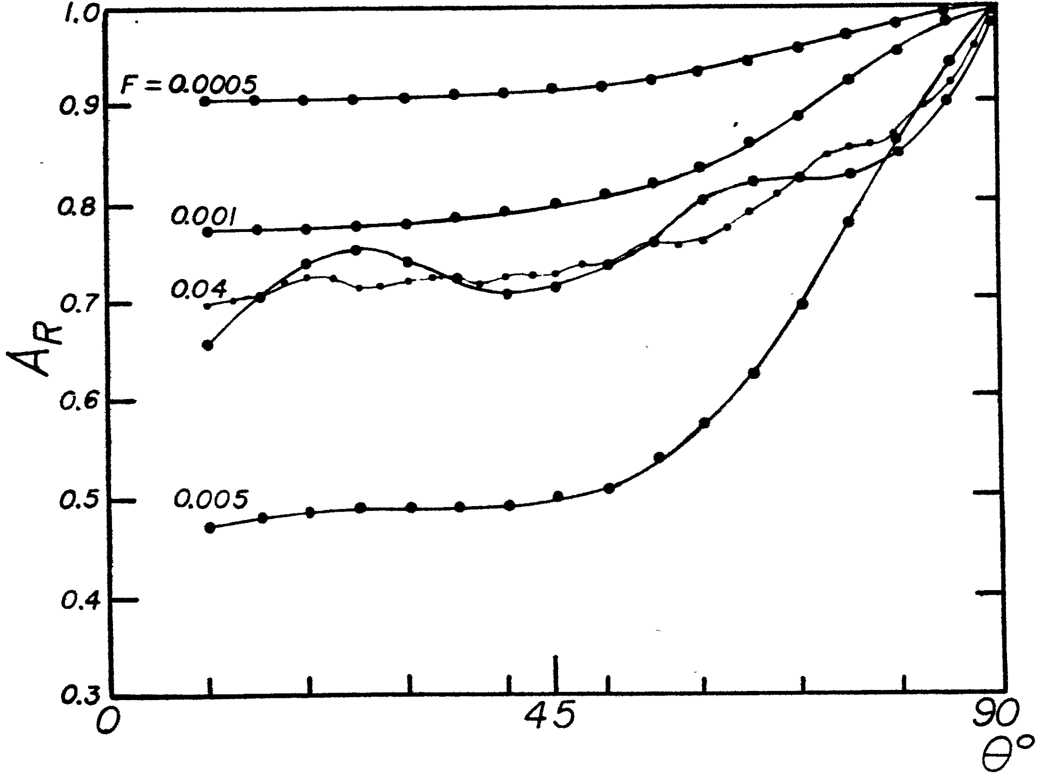

3.18: This is a plot of the radial amplification factor as a function of position on the dark side when the source field is specified by $\psi = 0$ and $V_{SW} = 300$ km/sec. The values shown start at 10° from the antisolar point in order to avoid the difficulty associated with the fact that the incident field has no power along the radial component at the antisolar point. At the frequency 0.04 Hz, we have plotted the response computed using 10 (heavy dot) and 15 parameters in our representation of the poloidal H and of the end effect field. Though the latter case smoothes out the response, the relative amplitude of the oscillation still present in the former case does not reach more than 5% of the total field. Note that the radial response is characterized by a broad minimum with practically constant value within 45° from the antisolar point. Thus variation of the response with position is not very important in that region.

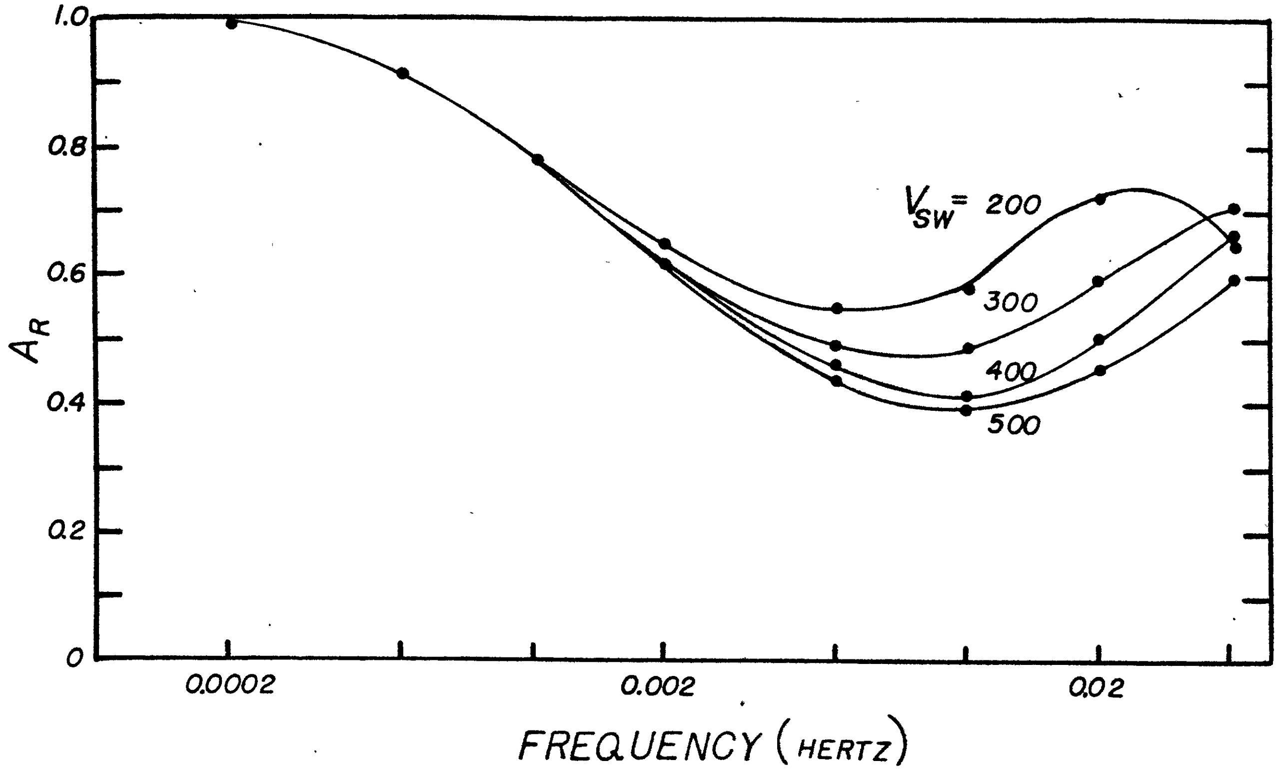

Figure 3.19: This is a plot of the radial amplification using a source field specified by $\psi = 0$ but with different solar wind velocities. The amplification values shown were calculated at 25^0 from the antisolar point and are average at high frequency to minimize the effect of the oscillation shown in the preceding figure. We note that the response decreases from unity at low frequencies, reaches a minima, and then starts to increase at high frequencies. At still higher frequencies, the response reaches a maximum and then decreases monotomically to 0. This behavior is typical only of low angle of

incidence source fields and is related to the distortion of the incident field by the surface wave. However, such behavior is probably not typical of what is observed near the antisolar point, as shown in the next figure.

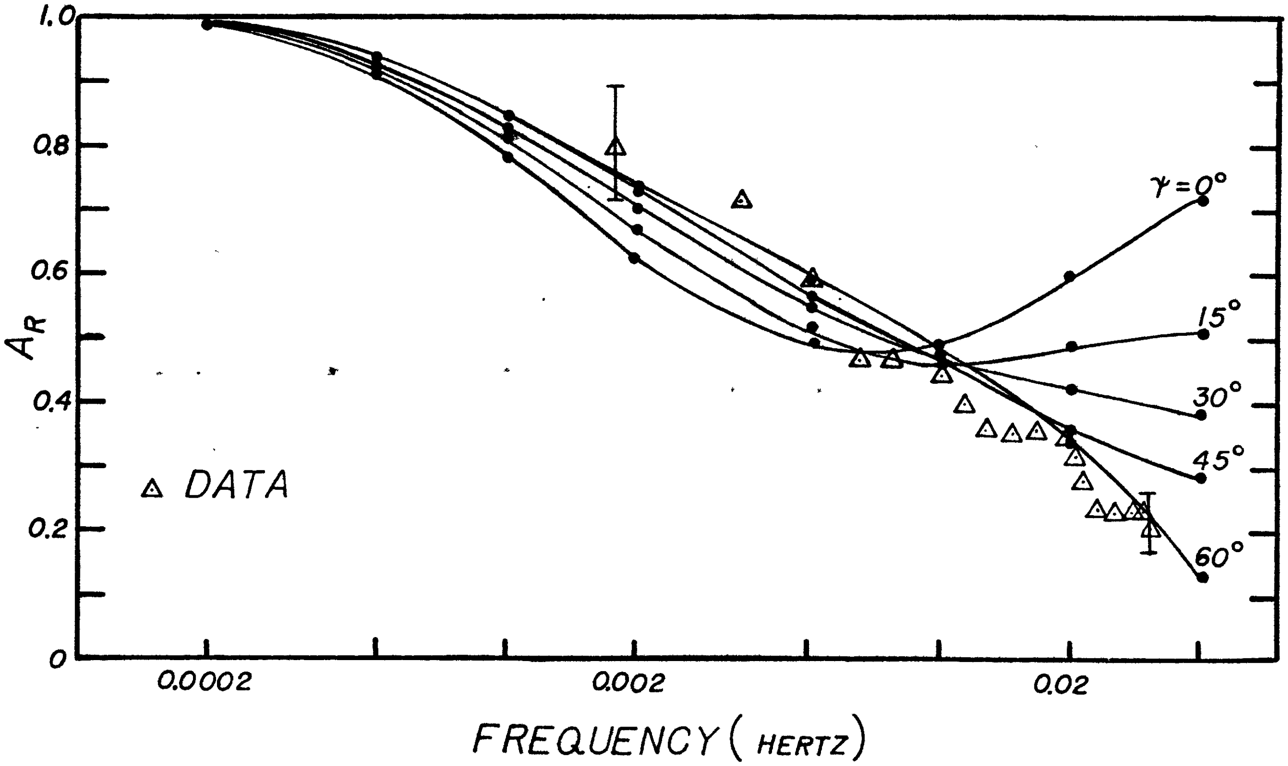

Figure 3.20: This is a plot of the A_R response for various angles of incidence but constant solar wind velocity: V_{SW} = 300 km/sec. The position of the LSM was assumed to

be at 25^0 from the antisolar point along the curve $\phi = 270^0$. The computed response at any polar angle in the range $\theta = 0 - 45^0$ is typically within 5% of the radial amplification factors exhibit in Figure 3.20. (The only noteworthy exception is the case $\psi = 60^0$ at 0.04 Hz where the response varies from 0.13 to 0.20 in the polar range $\theta = 0 - 45^0$).

We note that the computed response is very sensitive on the angle of incidence and thus the data hardly can be inverted without some information about the distribution of this quantity in the incident field. The fact that the data tend to agree with curves of the computed responses characterized by large angles of incidence probably comes about because near the antisolar point the power in the radial component is heavily biased toward such angles since they are associated with relatively large magnetic field components along the axes of the cylinder.

Before proceeding to the inverse problem let me summarize the result of this section.

Let us consider first the dark side data. For the radial amplification we just showed that a reasonable fit to these data can be obtained by using a model fitting the A_{min} value on the front side and choosing relatively large angles of incidence for the source field. However, due to the large sensitivity of this response to the angle of incidence, a proper inversion of the dark side radial amplification data must await additional information on the source field. This need for additional information on the source field parameters is also true for the tangential amplification on the back side, especially above 0.005 Hz. A proper interpretation of these data is further compounded by our ignorance of the exact position of the LSM when these data were taken. For frequencies smaller than 0.005 Hz, this latter dependence seems to be the most important parameter affecting the response (apart from the conductivity model). We noted that though the radial data and high frequency tangential dark side data tend to confirm the soundness of the asymmetric theory, the same cannot be said of the low frequency tangential dark side data. The measured tangential response on the dark side is almost equal to the one measured on the sunlit side whereas the theory predicts that it should be substantially less than the sunlit side response. We might also point out that additional data on the dependence of the response with position were published recently by Smith _et al._ (1973). But there again, the measurement at 0.0017 Hz did not exhibit clearly a smaller response on the dark side than on the sunlit side. However, the large uncertainties associated with these data preclude any definite conclusion at this stage. Needless to say, complete confidence in the asymmetric theory can only be gained by its confirmation over the whole frequency range of interest. Therefore we feel that additional measurements of the dark side response should be carried on, especially in the low frequency range and that noise possibly arising from drift current at the plasma vacuum interface should be accurately assessed in the future.

The front side data are indicative of a much smaller relative dependence on the source parameters and LSM positions and also a much greater sensitivity to the conductivity model, especially at shallow depths. A major drawback, however, is the noise associated with the remanent field at the Apollo 12 site. We correct empirically for this source of noise by calculating the A_{min} values but this process also removes some of the natural anisotropy we might expect between the two tangential responses. However, the fact that the Apollo 12 A_{min} values agree with the Apollo 15 data adds to our confidence in their use.

Chapter IV

Inverse Problem and Conclusion

4.1 Introduction

A substantial effort to remove some of the anthropomorphic character associated with the inversion of geophysical data recently has appeared in the literature. In the next section, we shall describe the formalism we used for our problem. Our analysis followed substantially the treatment given in Wiggins (1973).

Two studies of the resolution of the lunar conductivity structure provided by the magnetic data have already appeared in the literature (Hobbs, 1973 and Phillips, 1972). However, they both assume a symmetric plasma theory and an infinite value for the solar wind velocity. Moreover, since these studies appeared, the frequency range of the available data has been extended and the effect of the remanent field has at least been empirically removed. Thus we shall endeavor here to bring the subject up to date.

The third section shall be devoted to a description of the results obtained when the lunar conductivity structure is modelled as a conventional layered sphere. In the fourth section, we shall constrain our conductivity model by assuming a given temperature distribution inside the moon. The object then will be to understand to what extent the conductivity model constrained the conductivity-temperature relationship of the material likely to form the bulk of the moon. In the last section, we shall summarize our results, pointing out various directions that can be followed to improve them, and examine some of the geophysical constraints the results seem to imply.

4.2 Specialized Solution of the Forward and Inverse Problem

As we pointed out in the last chapter we shall try to match the data by assuming the magnetometer to be at the subsolar point and the incident field to have its normal parallel to the axis of the cylinder. In that case, only the harmonics specified by m = 1 are involved in the computation of the field. Moreover, since the response is isotropic at the subsolar point for the assumed source field, we can conveniently specialize its characteristic to the case $H_{ox} = 0$ and $H_o = 1$ [see, for example, Equation (2.2.2)], which in turn involves only the harmonics specified by $\sigma = 1$. The theoretical tangential amplification factor is then simply given by

$$A = (H_\phi \bar{H}_\phi)^{1/2} \Big| \; \phi = 0°, \; \theta = 180° \qquad (4.2.1)$$

where the bar stands for the complex conjugate and where

$$H_\phi\Big|_{\phi=0^\circ,\theta=180^\circ} = \sum_n \frac{a^1_{n1} L_n P^1_n(\cos\theta)}{\sin\theta}\Bigg|_{\theta=180^\circ}$$

From Equation (3.3.1), the coefficient a^1_{n1} are found by solving the matrix equation

$$C_{11}X_{11} = S_{11} \tag{4.2.2}$$

It is interesting to point out that even for an arbitrary incident field, the tangential amplification factor at the subsolar and antisolar points involves only the evaluation of the partial field associated with the harmonics specified by $m = 1$ and $\sigma = 1,2$. This comes about because, in our chosen coordinate system, the partial field associated with each Fourier harmonic in the ϕ coordinate can be solved separately and also because the terms of the form $\frac{P^m_n(\cos\theta)}{\sin\theta}$ and $\frac{\partial P^m_n(\cos\theta)}{\partial\theta}$ in our general expression of the lunar surface magnetic field [see Equation (2.3.1)] are equal to zero at $\theta = 0°$ and $180°$ if $m \neq 1$. A similar result holds for the radial amplification factor at the subsolar and antisolar point but this time, only the harmonic specified by $m = 0$ needs to be considered.

For most of the following results, a search was made for a parameterization of the conductivity structure yielding a good fit to the response at eight frequencies approximately equidistant on a logarithmic scale. These were 0.0002, 0.0005, 0.001, 0.002, 0.005, 0.01, 0.02 and 0.04 Hz, corresponding to periods of 25 sec to about 1.4 hour. Also, eight layers with fixed thicknesses generally were used to model the conductivity structure.

A logarithmic correction to an initial parameterization can be found through the matrix equation

$$By = p \tag{4.2.4}$$

where

$$B_{ij} = \frac{\partial \ln A(f_i)}{\partial \ln \sigma_j}$$

$$y_i = \Delta \ln \sigma_i$$

and

$$p_i = \ln \left[\frac{A(f_i)\text{measured}}{A(f_i)\text{computed}}\right]$$

From Equation (4.2.2), we note that there are two main steps involved in calculating the partial derivatives implied in Equation (4.2.4). First, the partial derivative of the L_n factors with respect to each conductivity parameter must be evaluated. An analytical expression for these derivatives can be worked out easily from our expression for the L_n in Appendix II, and the numerical computation can be most conveniently performed together with the evaluation of the L_n factors. We also require the partial derivative of each coefficient a^1_{nl} with respect to each conductivity parameter. These derivatives can be obtained by taking the partial derivative of Equation (4.2.3) and noting that S_{11} is independent of the conductivity, we obtain:

$$C_{11} \frac{\partial X_{11}}{\partial \sigma_i} = - \frac{\partial C_{11}}{\partial \sigma_i} X_{11} \tag{4.2.5}$$

Once Equation (4.2.3) is solved and the partial derivative of the L_n factors are computed, the right-hand side of Equation (4.2.5) is completely determined. Moreover, since the left-hand side of Equations (4.2.3) and (4.2.5) involves the same matrix C_{11}, the set of Householder transformations used to find the least square solution of Equation (4.2.3) can be conserved and then used repeatedly to solve Equation (4.2.5) for the partial derivative terms.

In order to gradually reduce the effect of small eigen-values associated with Equation (4.2.4), the generalized inverse operator

$$(B^T B + \varepsilon^2 I)^{-1} B^T$$

was used to find a solution (Madden, class notes). A practical way of finding the solution through this operator is to follow the method suggested by Golub (1965) which consists of applying a series of Householder transformations to the modified matrix equation

$$\begin{bmatrix} B \\ \cdots \\ \varepsilon I \end{bmatrix} y = \begin{bmatrix} P \\ \cdots \\ 0 \end{bmatrix} \qquad (4.2.6)$$

The choice of ε was made by a trial and error search for a number giving a stable iteration and yielding models giving a good fit to the data. We found that, if this value was chosen to be between 0.05 and 0.1, which usually corresponds to allowing from 2 to 3 linear combinations of parameters to participate in the solution, both a good fit and a stable iteration were realized.

Once Equation (4.2.6) is solved, the new model parameter can be found through

$$\sigma_i^{new} = \sigma_i^{old} e^{y_i} \qquad (4.2.7)$$

The probable presence of systematic errors in the data ruled out a rigorous discussion of the trade-off between the resolution of the parameter correction and the standard deviations associated with uncertainties in the data. However, since a quantitative basis for a discussion of parameter resolution is most naturally provided by this trade-off, we shall assume the observational error at each frequency to be uncorrelated and to have a relative standard deviation of 5%. This value corresponds roughly to the standard deviation attributed by Sonett (1974) to the A_z and A_y values resulting from his data analysis. However, this estimate seems clearly optimistic in view of the relatively large correction that was applied to these data to account for the presence of the remnant field (see Figure 3.4). To alleviate some of this uncertainty, we shall use several versions of the data as given by the A_{min}, A_z and A_y values.

It is well known (Lanczos, 1961) that the matrix B can be decomposed as follows:

$$B = U \begin{vmatrix} \lambda_1 & & 0 \\ & \lambda_2 & \\ & & \cdot \\ 0 & & \cdot \end{vmatrix} V^T \qquad (4.2.8)$$

where the elements of the diagonal matrix of eigenvalues can be conveniently ordered such that $\lambda_i \geq \lambda_{i+1}$ and where U and V are the matrix of eigenvectors of BB^T and B^TB respectively.

The resolution matrix of the parameter correction associated with the k largest eigenvalues of B is defined as

$$R_K = V_K V_K^T \tag{4.2.9}$$

where the K columns of V_K are the first k columns of V.

The standard deviation of the parameter correction associated with the uncertainties in the data is then given by

$$(\text{STD. DEV.})_{kj} = 0.05 \left(\sum_{i=1}^{k} V_{ji}^2/\lambda_i^2 \right)^{1/2} \tag{4.2.10}$$

Similarly, we can define a resolution matrix of the observations by

$$D_k = U_k U_k^T \tag{4.2.11}$$

where the k columns of U_k are the first k columns of U. Examination of each row of D_k permits us to determine to what extent the information contained in a given observation is used to estimate the k linear combinations of the parameter correction implied by R_K.

Before displaying the results, let me add a general remark.

In all the models shown in this chapter, the conductivity of the top layer was kept constant in the inversion routine at 10^{-10} mho/m. This has little effect on the resulting model when only the poloidal H mode is used to invert the data, but it effectively renders the toroidal H magnetic field negligible, in harmony with the data.

4.3 Results from the Inversion of a Layered Sphere Without Thermal Constraints

Since we feel that the reader should get an overview of the results before the significance of some of the details can be appreciated, we shall limit ourselves here to their description, leaving a discussion of their common characteristics to the last section.

Figure 4.1: We show here a model obtained when a solar wind velocity of 200 km/sec is used to invert the data. Also shown are the standard deviation and resolution* of the parameter corrections when 2, 3, and 4 eigenvectors are used to form the resolution matrix R_K. We

---

*The elements of the resolution matrices were rounded to increments of 0.2 merely to facilitate their plotting. This does not, however, significantly alter their information.

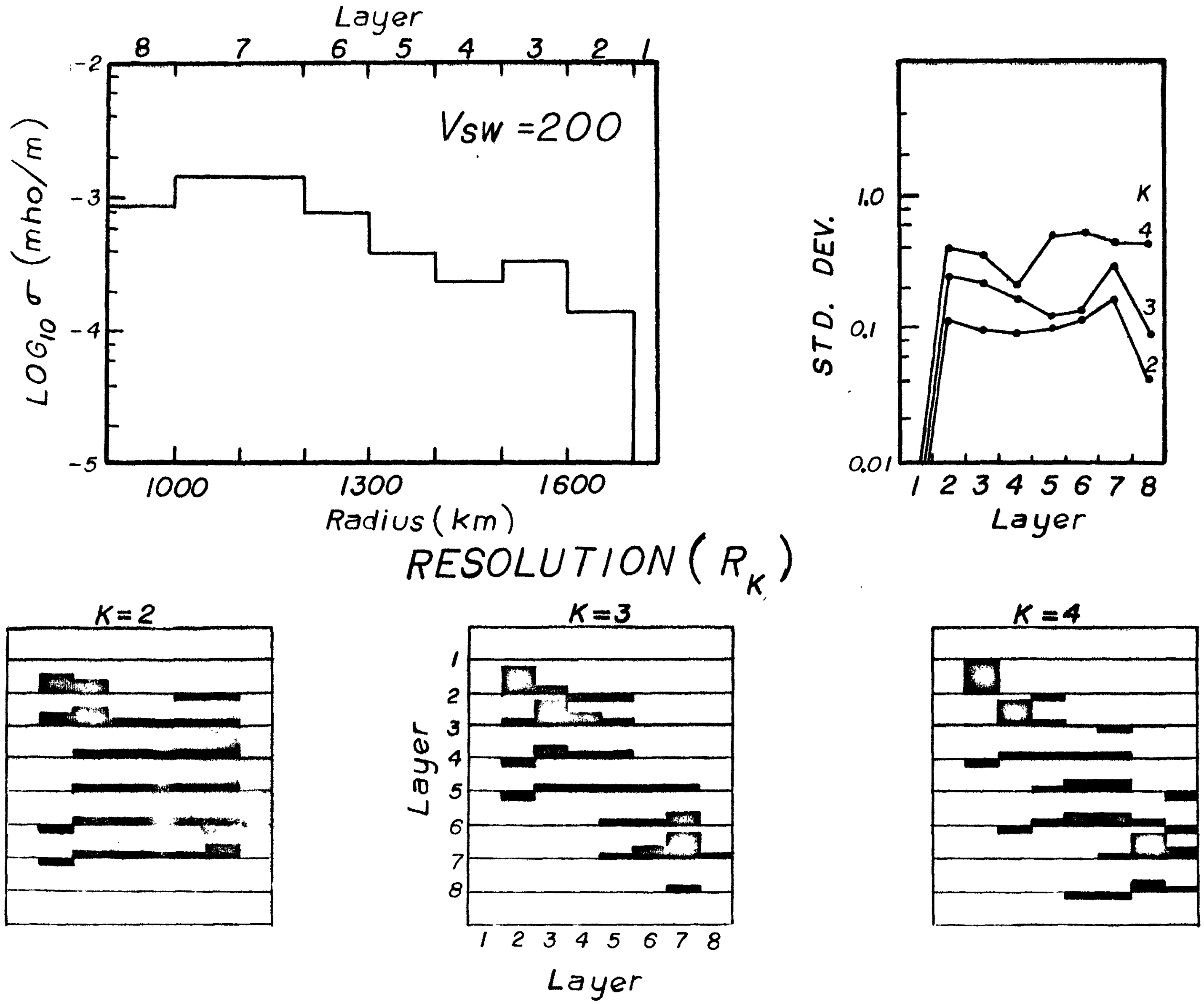
Layer
8 7 6 5 4 3 2 1
Vsw =200
LOG10 σ (mho/m)
-2
-3
-4
-5
1000
1300
1600
Radius (km)
STD. DEV.
1.0
0.1
0.01
K
4
3
2
1 2 3 4 5 6 7 8
Layer
RESOLUTION (R_K)
K=2
K=3
K=4
Layer
1
2
3
4
5
6
7
8
1 2 3 4 5 6 7 8
Layer

Figure 4.1

recall, however, that only 2 to 3 linear combinations of parameters were allowed to participate in the iteration in order to insure its stability. Perhaps we should not be surprised since 5% uncertainties in the data can result in a standard deviation of the parameter correction of 60% for four linear combinations of parameters.

We note that we have the good resolution at shallow (< 250 km), and moderate depths (from about 550 to 750 km), but a poorly resolved section between these two regions. Moreover, within the linear regime around our solution, the data practically are insensitive to the conductivity value at depths greater than about 750 km.

Figure 4.2: We show here the relatively good fit to the A_{min} data that occurs when the preceeding conductivity model is used to compute the response. The data resolution matrices D_K exhibits a more or less uniform distribution of information among the observations with somewhat higher resolution at the high and low frequency ends of the spectrum.

Figures 4.3 and 4.4: The results of a similar calculation using a solar wind velocity of 400 km/sec, are shown here. Again, a relatively good fit to the data

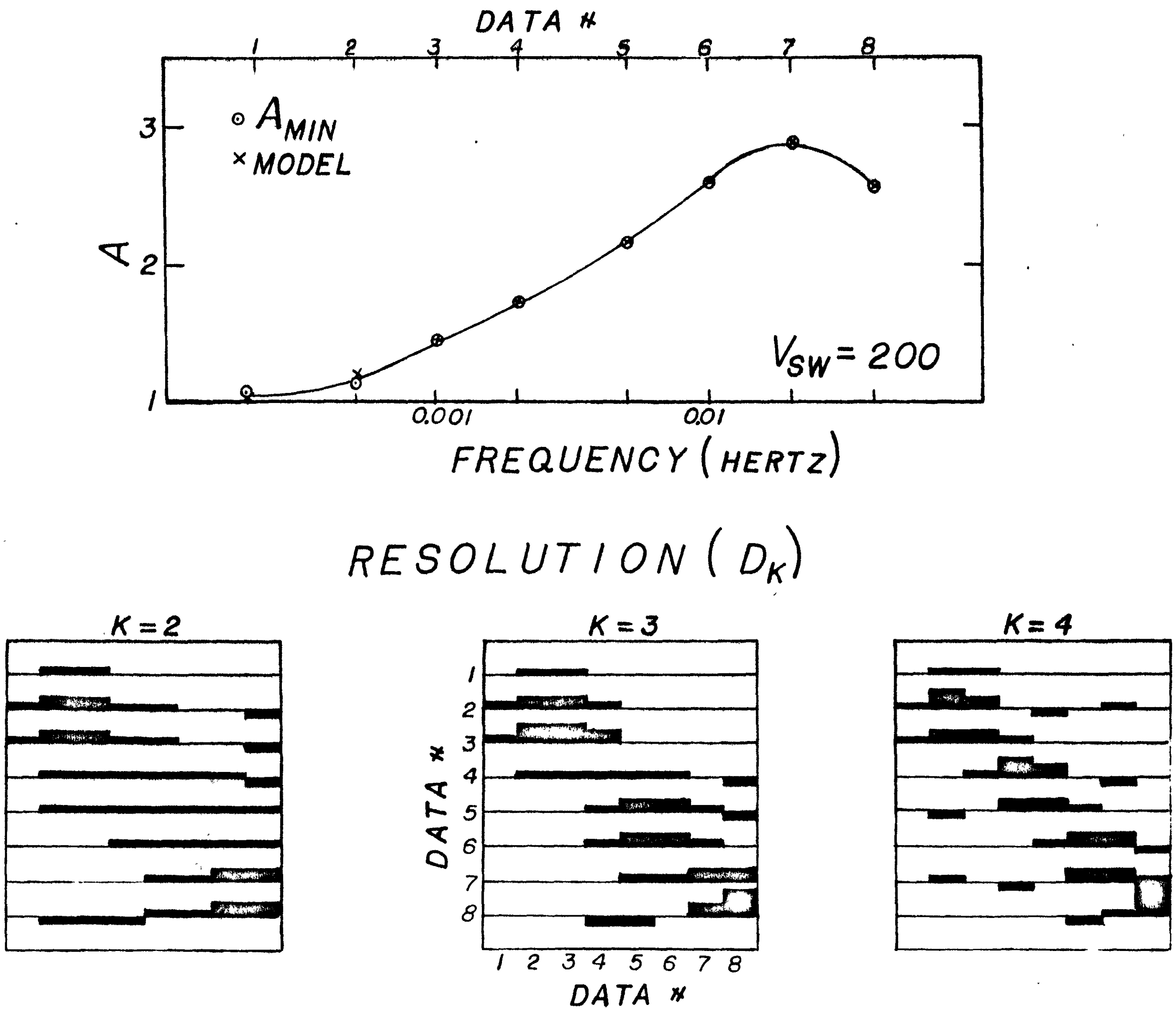
DATA #
1
2
3
4
5
6
7
8
A
3
2
1
⊙ A_{MIN}
× MODEL
V_{SW} = 200
0.001
0.01
FREQUENCY (HERTZ)
RESOLUTION (D_K)
K = 2
K = 3
K = 4
DATA #
1
2
3
4
5
6
7
8
1 2 3 4 5 6 7 8
DATA #

Figure 4.2

can be obtained but this higher solar wind velocity results in a substantial modification to the shallow conductivity structure of the model. The conductivity of the second layer was of such a low value that it was practically unresolved. A fairly well resolved section at a depth of 150 to 350 km was followed by a poorly resolved dip in the conductivity structure. Due to the possible importance of such a conductivity minimum, we examine its relevance in more detail in the next figure.

Figure 4.5: The middle diagram exhibits two models with different layer thicknesses than the preceeding ones, but computed with the same solar wind velocity. Their respective fit to the data is shown in the top diagram. Though the model with the more pronounced minimum does give a somewhat smaller least squares residual to the data, their computed responses differ only at the high frequency end of the spectrum. But since the response in the hihg frequency range is quite sensitive to the source parameters we can not consider one model more adequate than the other. This is emphasized by the 200 km/sec model shown in the bottom diagram which has a monotonously increasing conductivity with depth and actually gives an exact fit to the A_{min} data values.

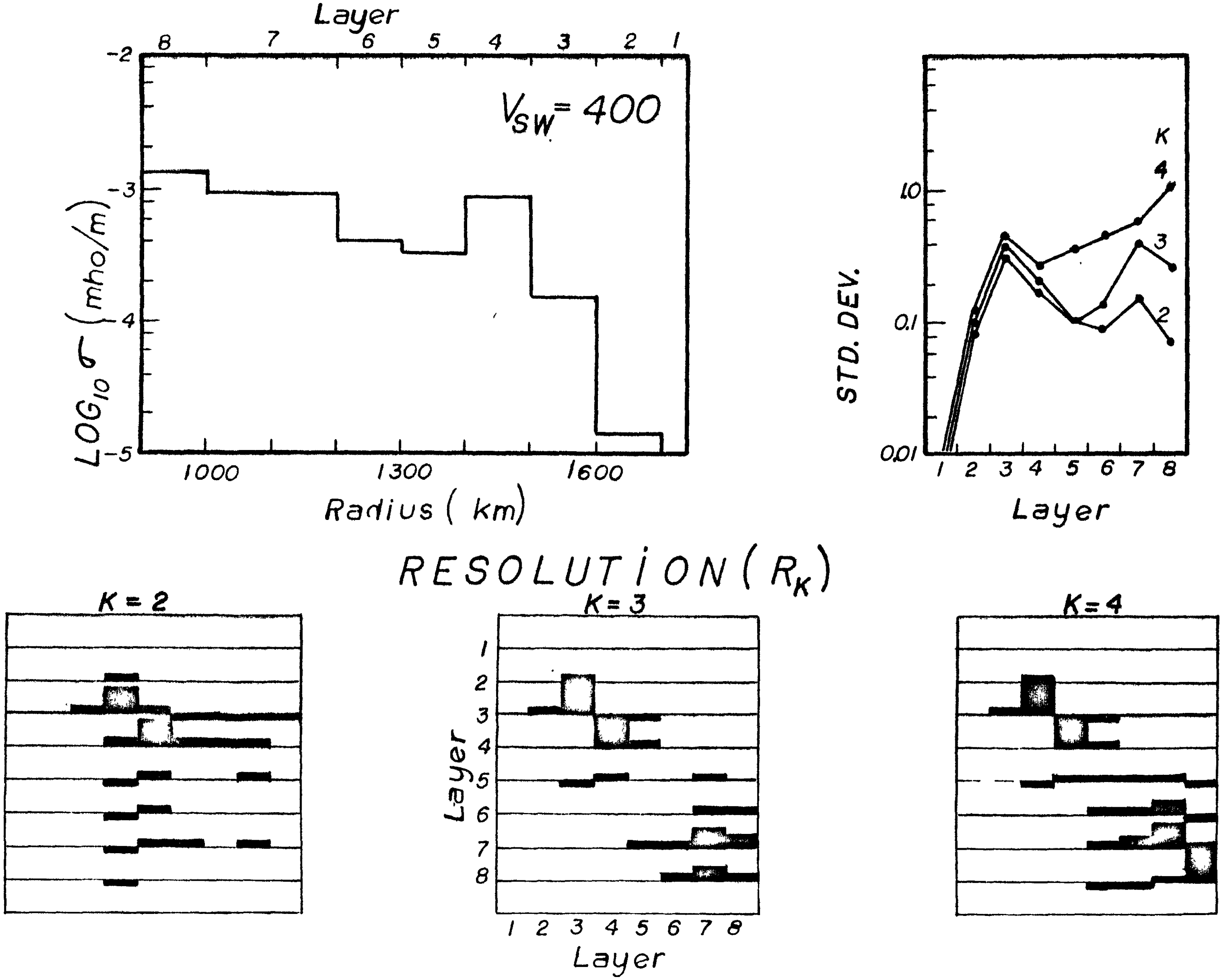
Layer
8
7
6
5
4
3
2
1
-2
-3
-4
-5
$V_{SW} = 400$
$LOG_{10}\, \sigma$ (mho/m)
1000
1300
1600
Radius (km)
STD. DEV.
K
4
3
2
1.0
0.1
0.01
1 2 3 4 5 6 7 8
Layer
RESOLUTION (R_K)
K = 2
K = 3
K = 4
1
2
3
4
5
6
7
8
Layer
1 2 3 4 5 6 7 8
Layer

Figure 4.3

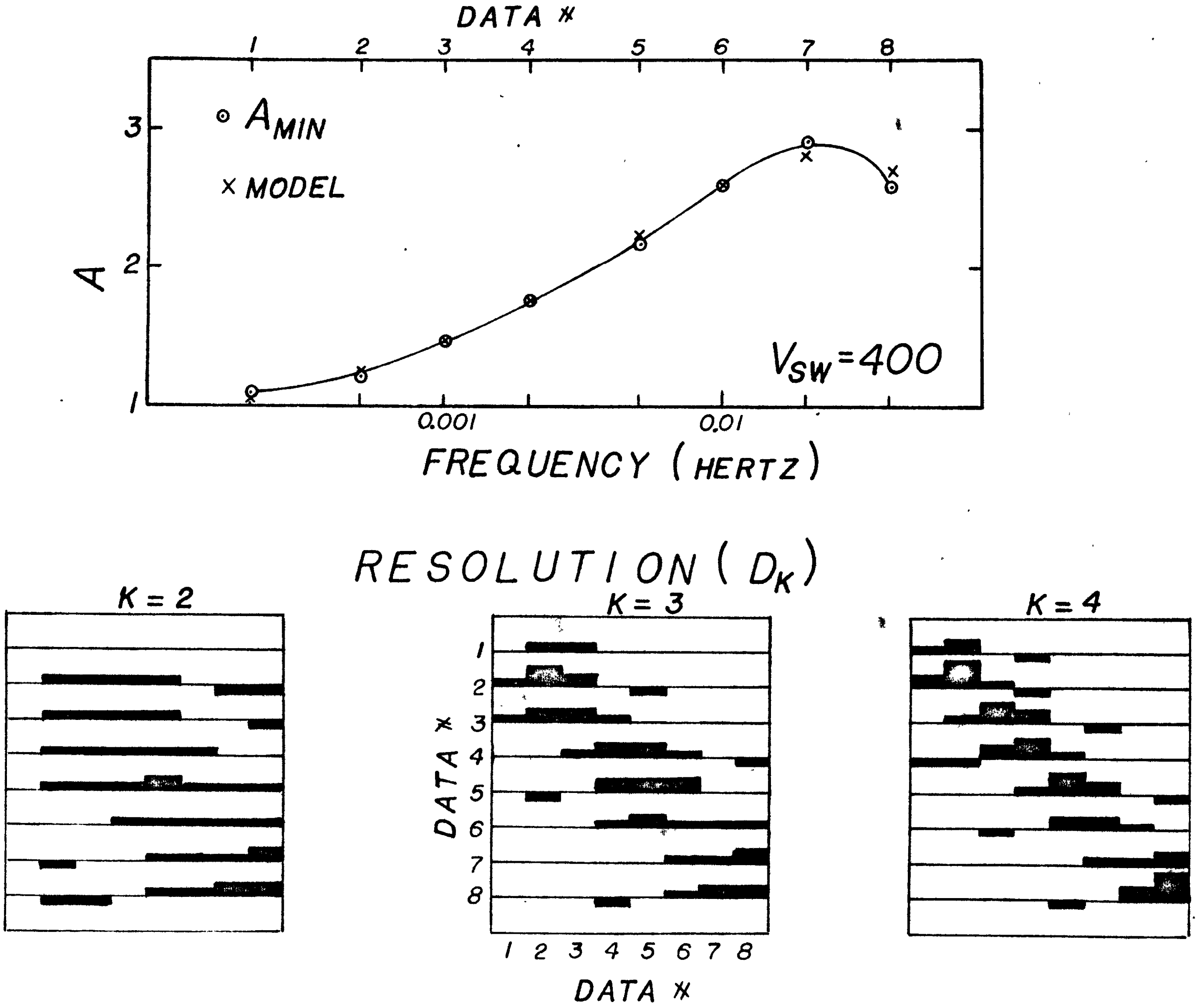
DATA ✗
1
2
3
4
5
6
7
8
A
3
2
1
A_{MIN}
× MODEL
$V_{SW}=400$
0.001
0.01
FREQUENCY (HERTZ)
RESOLUTION (D_K)
K = 2
K = 3
K = 4
DATA ✗
1
2
3
4
5
6
7
8
1 2 3 4 5 6 7 8
DATA ✗

Figure 4.4

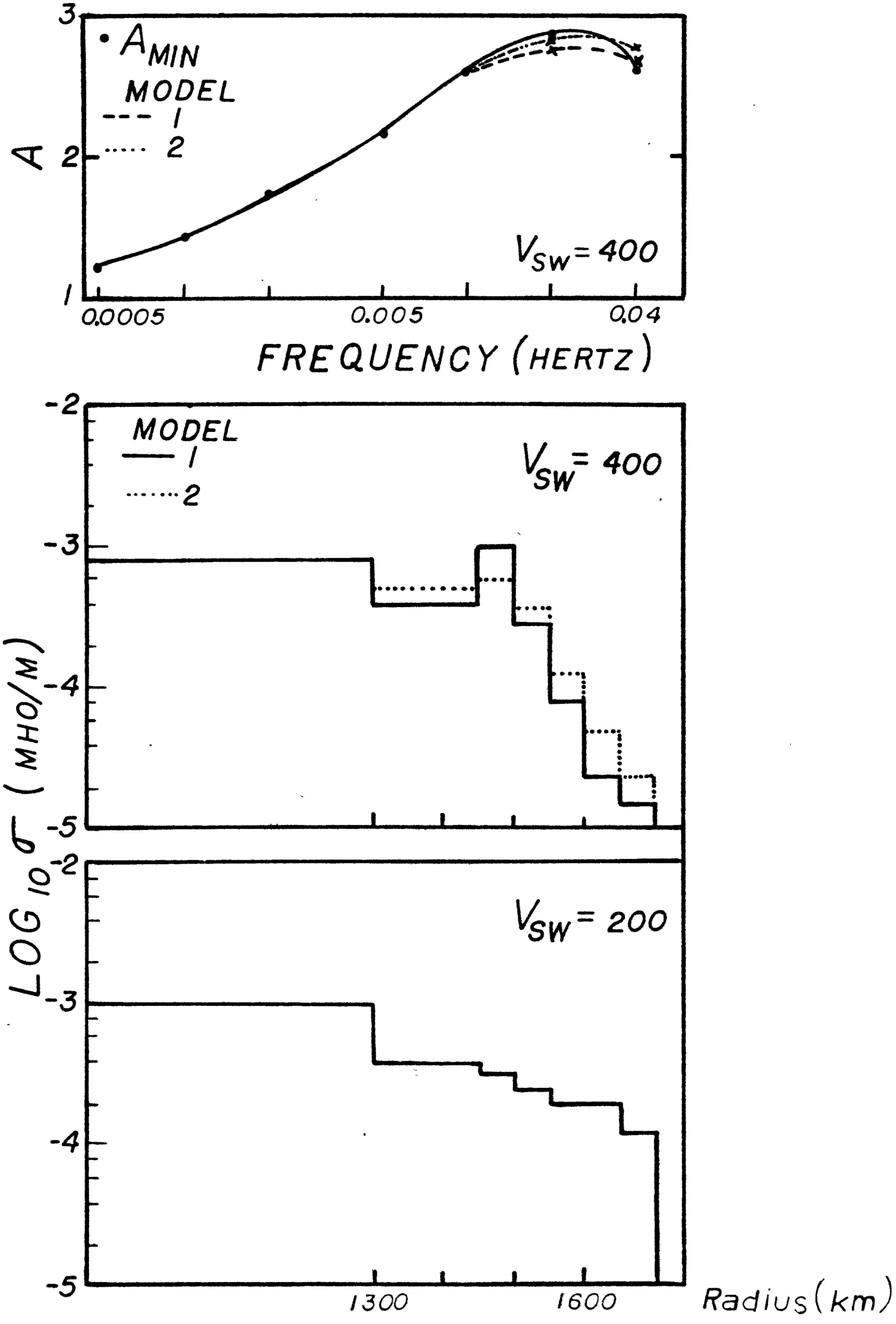
• A_{MIN}
MODEL
1
2
A
3
2
1
V_{SW} = 400
0.0005
0.005
0.04
FREQUENCY (HERTZ)
MODEL
1
2
V_{SW} = 400
-2
-3
-4
-5
$LOG_{10}\sigma$ (MHO/M)
-2
-3
-4
-5
V_{SW} = 200
1300
1600
Radius (km)

Figure 4.5

We recall that in the inversion we assume that the wave normal is parallel to the solar wind velocity. However, the average value of the data probably is determined from the superposition of a spectrum of fluctuations with significant power in waves with normals at substantial angles from the direction of the solar wind velocity. We recall from Figure 3.13 that an increase in this angle lessens the response at high frequencies and that a similar reduction occurs when response is computed for decreasing values of the solar wind velocity. Thus, even though 400 km/sec is near the observed average solar wind velocity of 350 km/sec, we cannot surmise that it is a more adequate value than 200 km/sec to use in an inversion which assumes the wave normal to be parallel to the solar wind velocity.

Figures 4.6 and 4.7: We show here three models, numbered 1, 2, and 3, with which we attempt to fit respectively the A_{min}, A_y, and A_z data values obtained at the Apollo 12 site. In all three cases, a solar wind velocity of 300 km/sec is used in the inversion. The resulting data fit the data shown in Figure 4.7. Notice in this last figure that the A_z value, though generally higher than the A_y value at most frequencies, is smaller than A_y at 0.04 Hz. As we have repeatedly stressed, the rollover in the response at high frequency is quite dependent on the parameters of the source. Thus, the relatively bad fit to the A_z data at high frequencies is probably symptomatic of our inadequate knowledge of the source parameters. Returning to Figure 4.6, we note that the conductivity model that attempts to fit these A_z values shows a conductivity level reaching nearly 10^{-2} mho/m at depths greater than 550 km. However, we shall show in the next section that if we tolerate a somewhat worse fit at high frequency, the low frequency data can be matched by a model having a substantially lesser conductivity at these depths. Since we are probably not justified with the data at hand to require a close fit to the high frequency response, the argument for a high conductivity at great depth becomes rather tenuous.

Before proceeding to our study of conductivity structures subject to a given temperature model, let us discuss the well resolved features of models 1 and 2. We note from Figure 4.6 that at depths between about 50 to 250 km the conductivity of model 2 is slightly larger than that of model 1. This conductivity difference is due to the higher values of the A_y data with respect to the A_{min} data at high frequencies. However, the approximate equality of A_{min} and A_y at low frequencies requires about

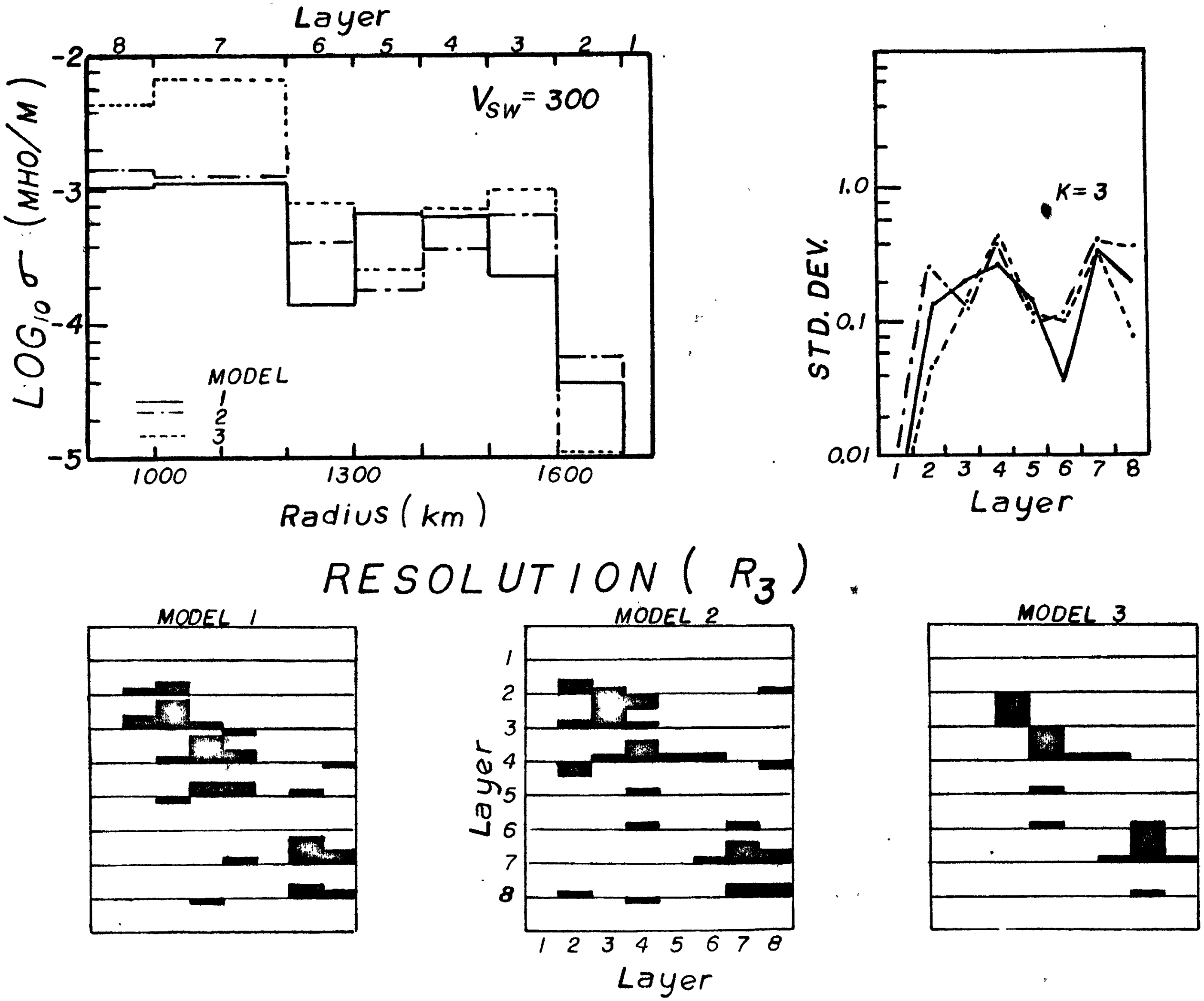
Layer
8
7
6
5
4
3
2
1
-2
-3
-4
-5
LOG₁₀ σ (MHO/M)
V_SW = 300
MODEL
1
2
3
1000
1300
1600
Radius (km)
1.0
0.1
0.01
K= 3
STD. DEV.
1 2 3 4 5 6 7 8
Layer
RESOLUTION (R₃)
MODEL 1
MODEL 2
MODEL 3
1
2
3
4
5
6
7
8
Layer
1 2 3 4 5 6 7 8
Layer

Figure 4.6

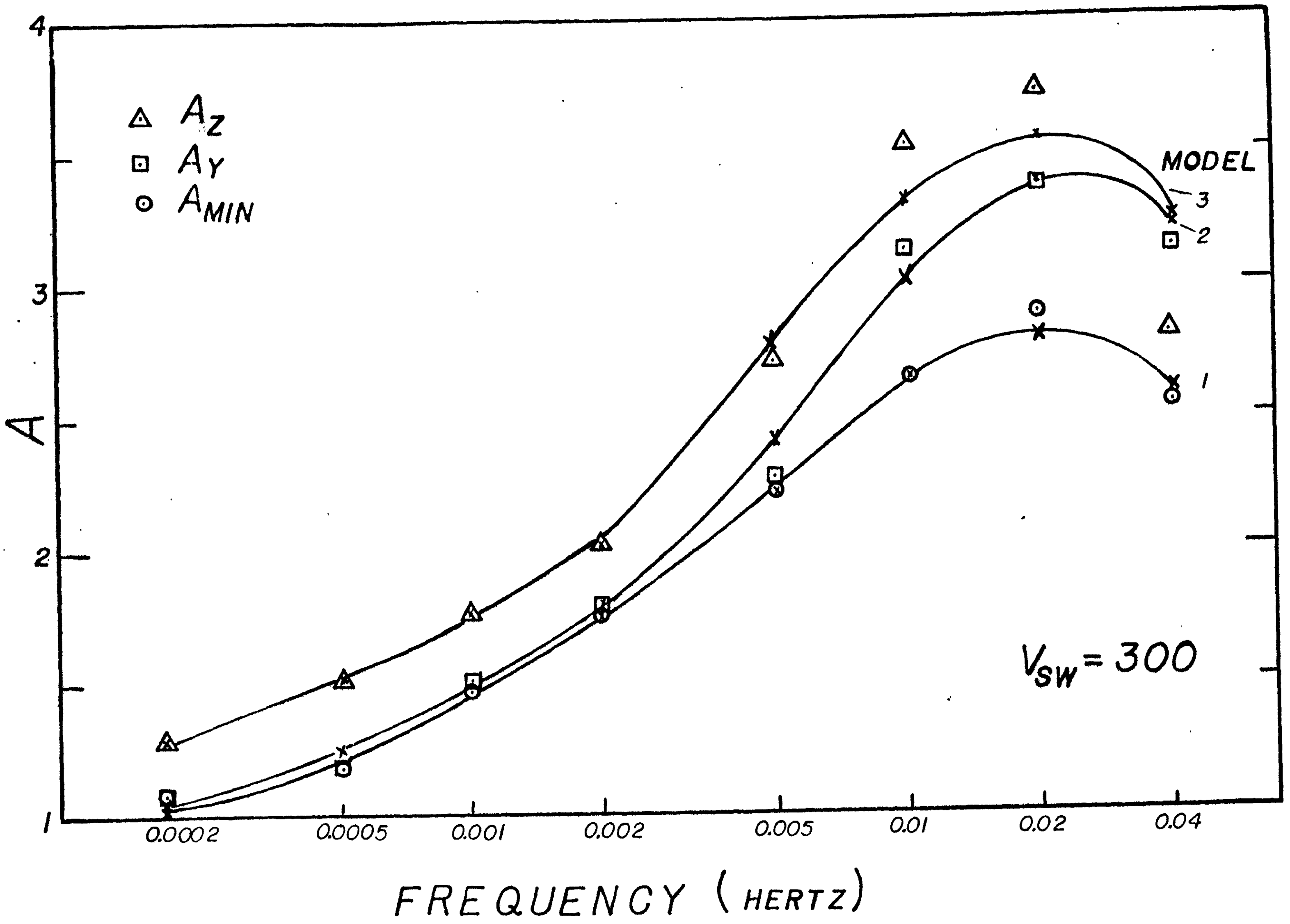

A
4
3
2
1
△ A_Z
□ A_Y
⊙ A_{MIN}
MODEL
3
2
1
$V_{SW} = 300$
0.0002
0.0005
0.001
0.002
0.005
0.01
0.02
0.04
FREQUENCY (HERTZ)

Figure 4.7

the same average conductivity-thickness product for both models. Consequently, at moderate depths (250 - 450 km) model 2 must exhibit a lower conductivity than model 1 to offset the higher conductivity of model 2 at shallow depths (50 - 250 km).

4.4 Inversion of a Layered Moon Constrained by a Temperature Model

We would like to know to what extent a given conductivity profile for the moon will constrain its composition and internal temperature distribution. A customary way to study this question is first to assume a composition based on independent geophysical and geochemical evidence. Then, from laboratory measurements of the conductivity-temperature relationship of the assumed mineral assemblage, deduce the temperature distribution from the electrical conductivity model.

For most types of common reocks and minerals, the conductivity-temperature relationship is depicted by a series of connected straight lines on a log σ versus the inverse of the absolute temperature. Each of these straight lines can be described conveniently by a relation of the type:

$$\sigma = \sigma_o \, e^{-E_o/kT} \tag{4.4.1}$$

where σ_o and E_o are called respectively the conductivity prefactor and activation energy and where k is the Boltzmann's constant, with the temperature T in degrees Kelvin.

Measurement of relations of the type 4.4.1 often are subject to large uncertainties, which arise for various reasons, such the fact that minor constituents of the mineral assemblage and the oxygen content in the atmosphere under which the conductivity of a rock sample is measured can disproportionately affect the bulk conductivity of the sample. Recent experimental investigators, especially Duba (1972a), have clarified this range of measurement uncertainties and some of their probable causes. By measuring the conductivity of different olivine samples, with essentially the same fayalite content, but with differing amounts of Fe^{3+} and under atmosphere with widely different oxygen content, Duba was able to show that the temperature estimate from the conductivity of the earth's upper mantle might be in error by as much as $700^{0}C$. Thus, any attempt to deduce an estimate of the temperature inside the moon is a hazardous process indeed. Nevertheless, several such attempts have been made recently and we listed some of them merely to emphasize the range of uncertainties involved. These temperature estimates were aimed especially at determining the maximum temperature reached in the lunar interior. Since these estimates were based on an assumed conductivity level of about 10^{-3}mho/m reached between 500 and 700 km inside the moon, we would deduce essentially the same maximum temperature range from the results of the last section.

Sonett et al. (1972), using essentially the conductivity-temperature relationship of olivine from England et al. (1968), have estimated that the maximum temperature reached is between 800 to 1000°C in the upper 700 km of the moon. But, based on measurements on olivine and pyroxyne in an atmosphere with very low oxygen content, a condition believed to occur in the lunar interior, Duba et al. (1972b, 1973) were able to raise the preceeding estimate to values in the range 1100 to 1500°C. However, Tolland (1974), following a suggestion by Ringwood et al. (1970) that pyroxenite might be a correct choice for the lunar mantle composition, conducted some measurements on a synthetic lunar pyroxenite sample and obtained temperatures in the range 550 to 680°C. We should point out that Duba et al. (1973) also measured the conductivity of a synthetic lunar pyroxenite in an atmosphere of very low oxygen content. The conductivity level of 10^{-3}mho/m was reached at about 1000°C but they considered the uncertainties in their measurements too large to warrant any inference to be based on them.

Some of the data usen in these estimates are shown in Figure 4.8. The Fe^{3+} free olivine data is from Duba et al. (1972b) and was measured under a pressure of 8kb. The synthetic lunar pyroxenite data is from Tolland (1974) and the olivine from England et al. (1968). Also shown are the conductivity-temperature relationships of a lunar crystalline rock from Schwerer et al. (1971) and two curves labelled H and L that will be discussed shortly.

Due to our present uncertainties in our knowledge of the conductivity-temperature relationship of the material likely to form the bulk of the moon it might be useful to inquire to what extent given temperature models for the moon constrain this relationship. One

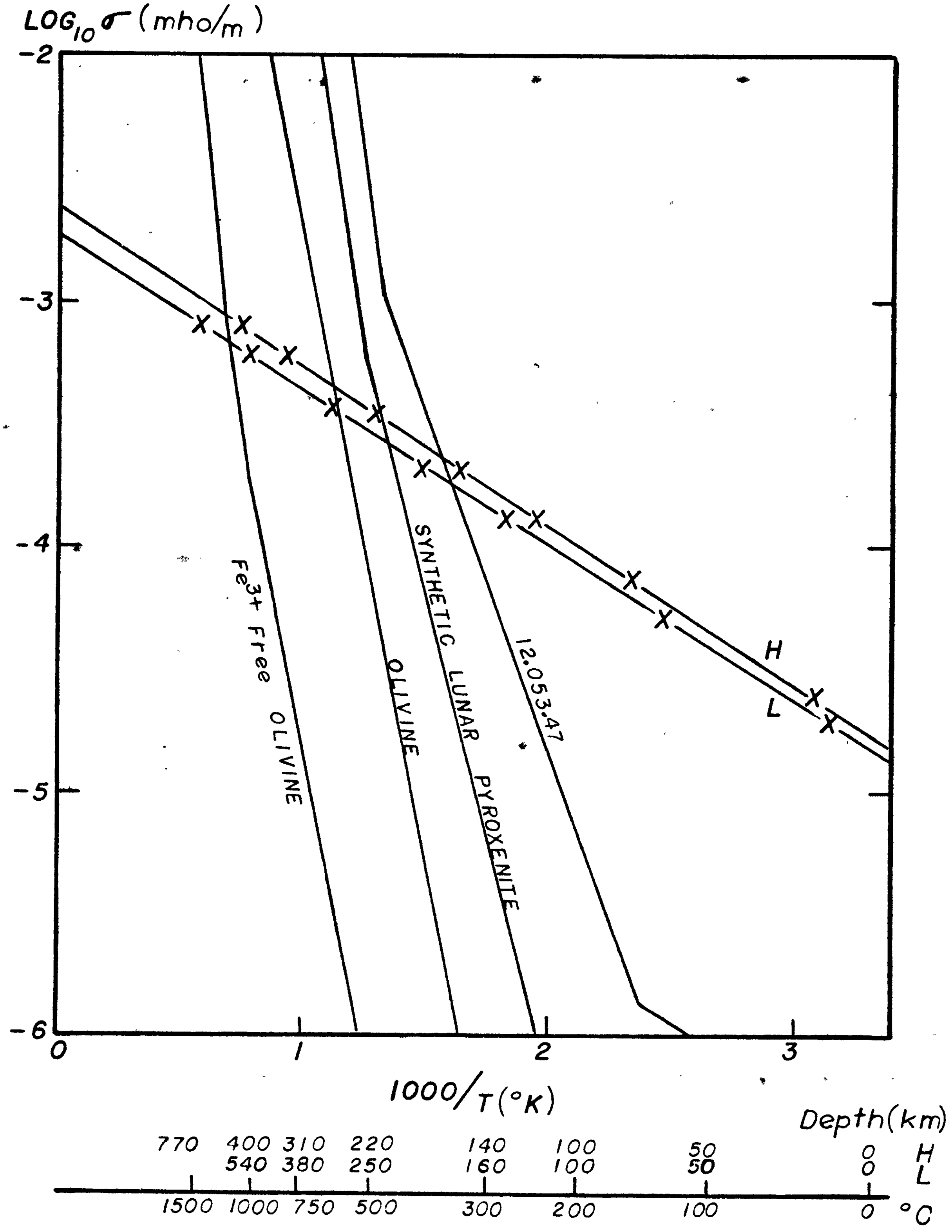
LOG10 σ (mho/m)
-2
-3
-4
-5
-6
0
1
2
3
1000/T(°K)
Fe3+ Free OLIVINE
OLIVINE
SYNTHETIC LUNAR PYROXENITE
12.053.47
H
L
Depth(km)
770
400 540
310 380
220 250
140 160
100 100
50 50
0 0
H
L
1500
1000
750
500
300
200
100
0
°C

Figure 4.8

idea behind this question is that the answer would automatically satisfy the impressive set of constraints that can be used in a calculation of the lunar thermal history. (see for example Solomon et al., 1973). Though these constaints help narrow the range of values that the temperature might attain in the lunar interior, there is still some controversy about the role of solid state convection in the lunar thermal history. This problem is still being investigated actively (Cassen et al., 1974). But,due to the uncertainties in the viscosity temperature relationship of the material inside the moon and the time scale associated with significant heat transfer by solid state convection, no definite conclusions have been reached yet. Nevertheless, some general conclusions can be reached for a rather wide family of temperature model. To get a qualitative idea on how this comes about, let us consider two temperature models proposed by Tokzöz et al. (1972) which were calculated using different uranium concentrations (U in Figure 4.9). We note that in these models that the temperature at depth 200 to 700 km increases by more than 600°C. Now let us assume

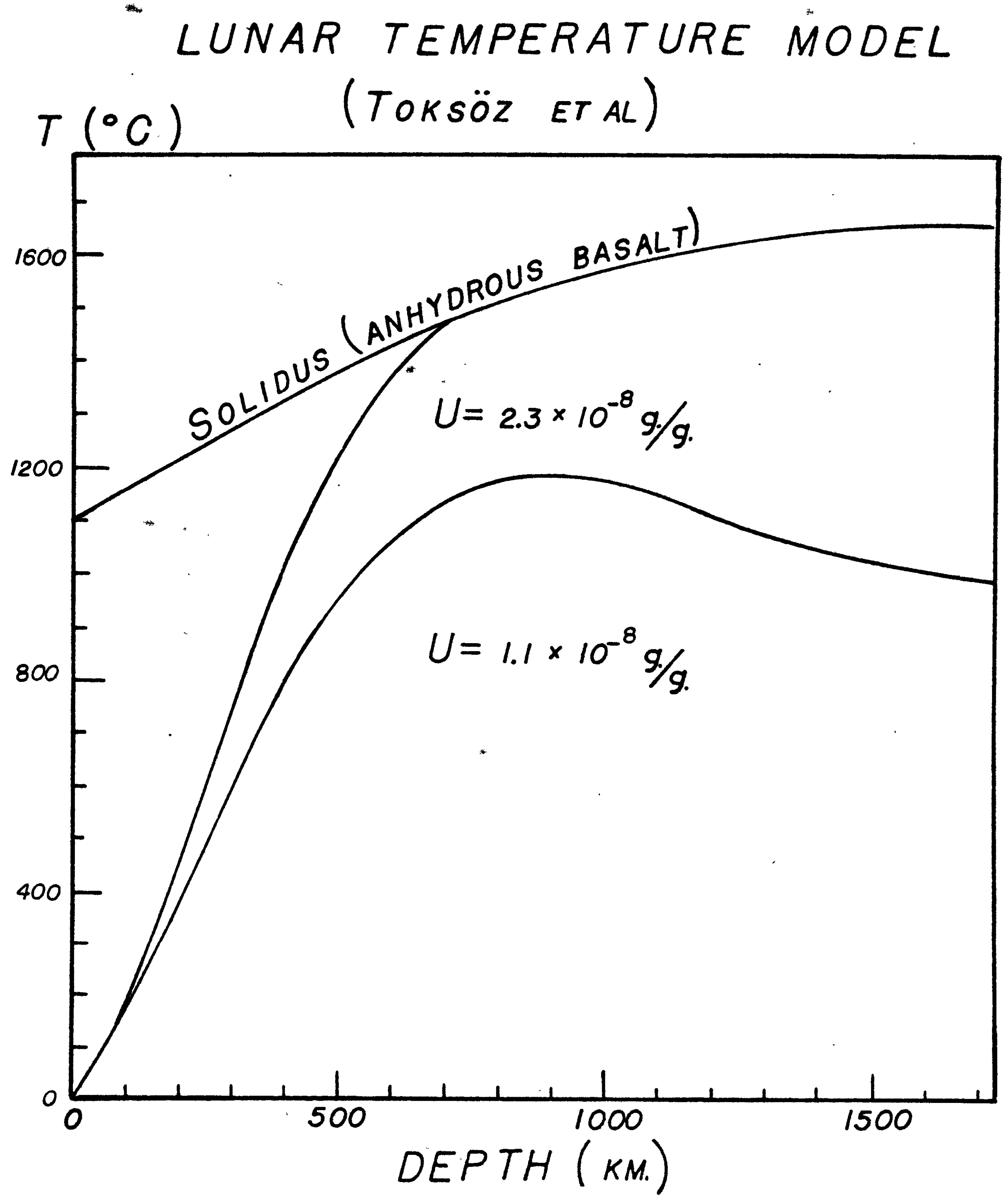
LUNAR TEMPERATURE MODEL
(TOKSÖZ ET AL)
T (°C)
1600
1200
800
400
0
SOLIDUS (ANHYDROUS BASALT)
U= 2.3 × 10^-8 g/g.
U= 1.1 × 10^-8 g/g.
0
500
1000
1500
DEPTH (KM.)

Figure 4.9

that the conductivity at these depths is characterized by a conduction mechanism with activation energy of 1 ev, an energy which is typical of the range of values for the materials shown in Figure 4.8. Then, the electrical conductivity would increase by more than 7 orders of magnitude between 200 and 700 km and this increase would flatly contradict our conductivity estimates of the last section.

Two simple models can explain this discrepancy. Either the activation energy is much lower than 1 ev or the temperature gradient at these depths is much smaller than the one shown in Figure 4.9. Although more complex explanations may exist, one of which shall be studied briefly later on, we shall concentrate mainly on the simpler alternatives since they might be of a more general interest.

In order to find the two parameters in Equation (4.4.1) that satisfy both the magnetic data and a given temperature model we can use an iteration similar to the one of the last section. This time, however, the logarithmic parameter correction must be found through the following matrix equation:

$$B \begin{vmatrix} 1 & -E_o/kT_1 \\ 1 & -E_o/kT_2 \\ \cdot & \cdot \\ \cdot & \cdot \\ \cdot & \cdot \end{vmatrix} \begin{vmatrix} \Delta\ln\sigma_o \\ \Delta\ln E_o \end{vmatrix} = p \qquad (4.4.2)$$

where B and p are given by Equation (4.2.4) and T_i is the temperature in the middle of layer i.

We proceed now to detail the results obtained reserving discussion for the last section.

We show first, in Table 4.1, the values of the parameters obtained for different values for the solar wind velocity when the moon is characterized by the low temperature model depicted in Figure 4.9. The corresponding conductivity models and the fits of their responses to the A_{min} data are shown in Figure 4.10.

Table 4.1

(Data: A_{min})

V_{sw} (km/sec)	σ_o (mho/m)	E_o (ev)
200	0.15×10^{-2}	0.093
300	0.31×10^{-2}	0.14
400	0.47×10^{-2}	0.18

The set of parameters shown in Table 4.2 were obtained again by using the low temperature model of Figure 4.9, but this time an attempt was made to match our different sets of data, keeping the solar wind velocity at a constant value of 300 km/sec.

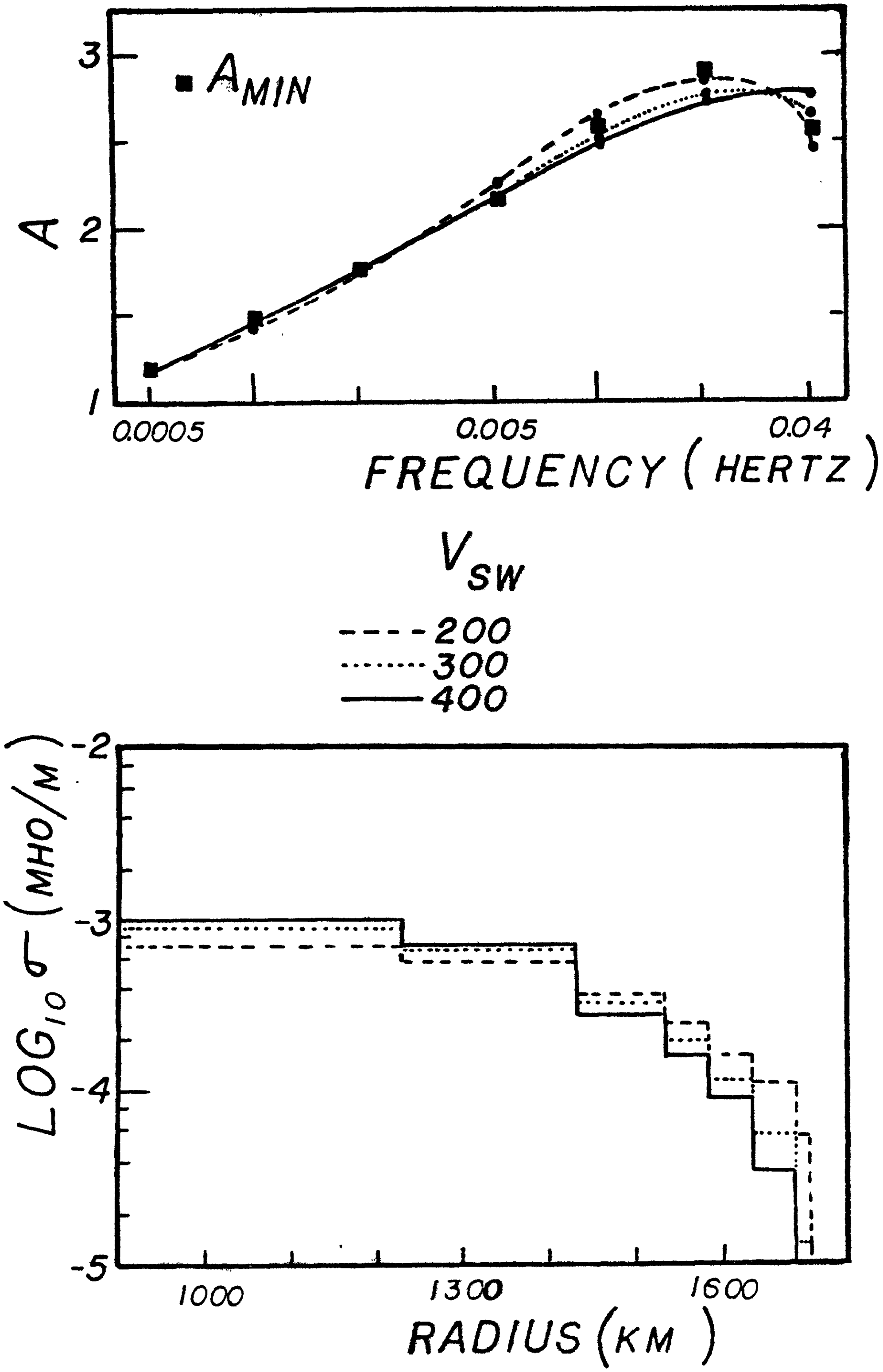
■ A_{MIN}
A
1
2
3
0.0005
0.005
0.04
FREQUENCY (HERTZ)
V_{SW}
200
300
400
$LOG_{10}\ \sigma$ (MHO/M)
-2
-3
-4
-5
1000
1300
1600
RADIUS (KM)

Figure 4.10

Table 4.2

(V_{sw} = 300 km/sec)

Data	σ_o^*	E_o
A_{min}	0.31×10^{-2}	0.14
A_y	0.17×10^{-2}	0.092
A_z	0.99×10^{-1}	0.16

We show on the bottom diagram of Figure 4.11 the conductivity models obtained when the A_{min}, A_y and A_z data values are used in the inversion. The fit to the A_y and A_z data is shown in the top diagram.

From the last two figures, we note that the computed responses do not give a very good fit to the data at the high frequency end of the spectrum. But, due to our uncertainties in the source parameters, we can hardly rule out any of these models on the basis of this misfit. Notice also that to fit the A_z data at low frequencies we require only a conductivity of the order of 10^{-3} mho/m.

We show in Figure 4.12 the standard deviation and resolution of the parameter corrections associated with the

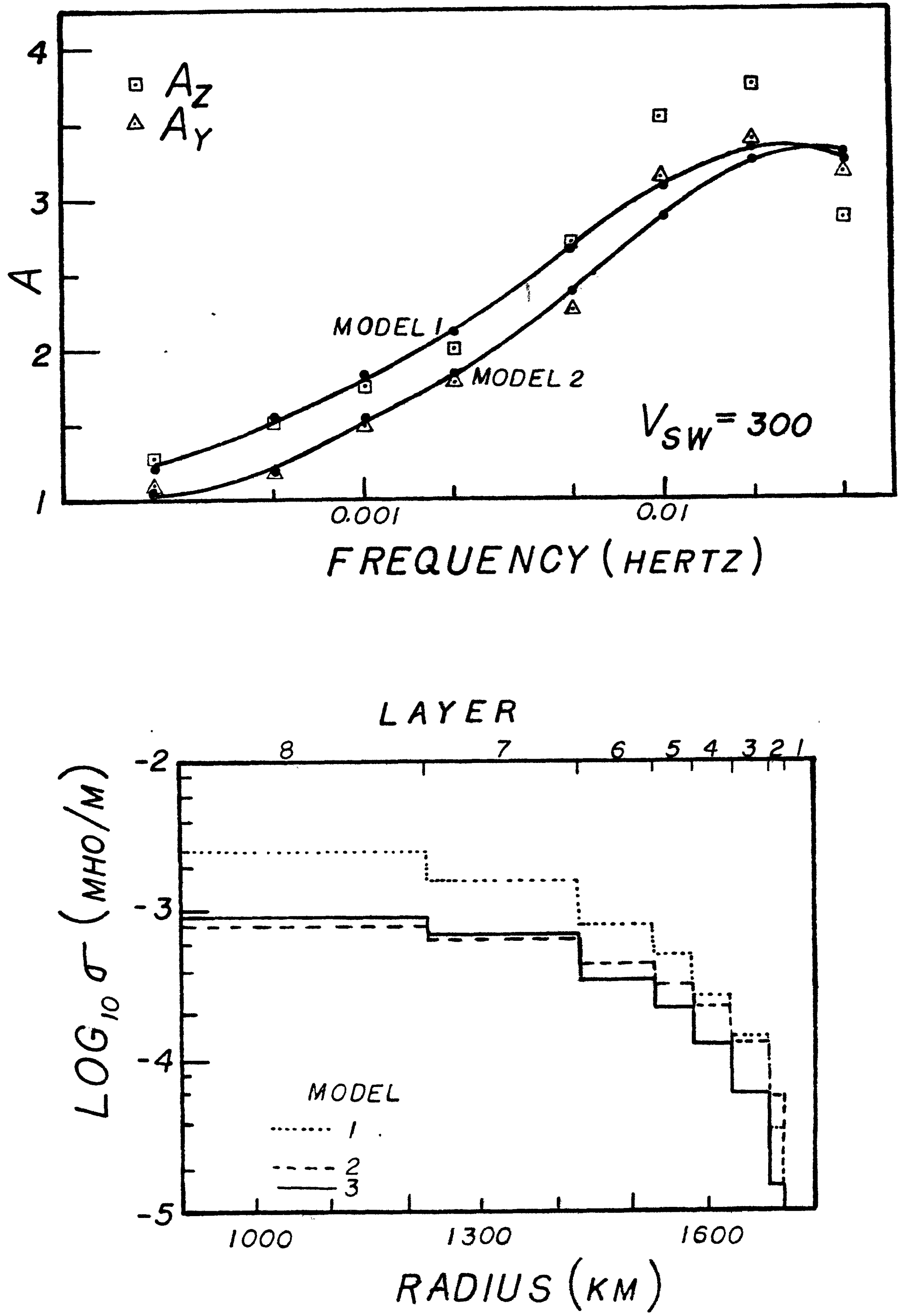
A_Z
A_Y
4
3
A
2
1
MODEL 1
MODEL 2
V_SW = 300
0.001
0.01
FREQUENCY (HERTZ)
LAYER
8
7
6
5
4
3
2
1
-2
-3
-4
-5
LOG10 σ (MHO/M)
MODEL
1
2
3
1000
1300
1600
RADIUS (KM)

Figure 4.11

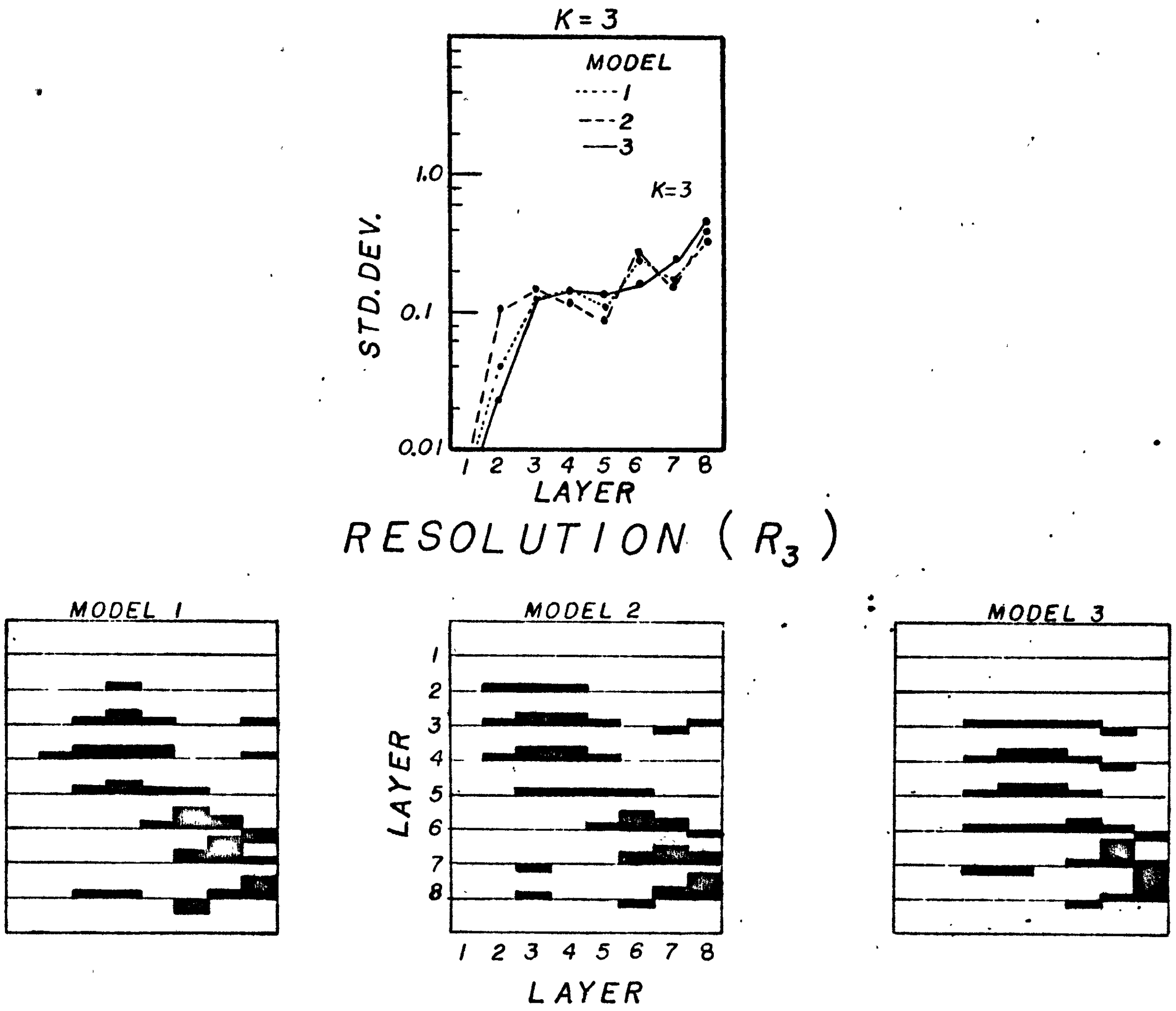

Figure 4.12 Resolution of Parameter Correction for Models Giving Best Fits to A_{min}, A_y, A_z Data

three models of Figure 4.11. If we compare these resolution matrices with the ones obtained in the preceeding section, we note a significant redistribution of the resolving power. The new distribution exhibits gradually increasing resolution with depth. This redistribution varies mainly because the temperature model forces a lower conductivity at shallow depth than that required for a better fit at the high frequency response. This constraint prevents these conductivities from shielding the lunar interior from induction over a substantial part of the frequency range of interest.

In order to study the dependence of our two parameters, σ_o and E_o on different temperature distributions, we considered first the high temperature model shown in Figure 4.9. The best fit to the A_{min} data, for V_{sw} = 300 km/sec, was obtained for $\sigma_o = 0.18 \times 10^{-2}$ mho/m and $E_o = 0.12$ ev. This pair of parameters pertains to the model labelled H in Figure 4.8 whereas the curve labelled L refers to the model obtained above using a lower temperature distribution but the same A_{min} data and source parameters. The bottom scales in Figure 4.8 indicate the depth at which a given temperature is reached in each model. Each set of crosses indicates the conductivity at depths common to both models. Thus, except at fairly shallow depths, where there is poor resolution, the conductivity of both models is essentially the same. However, somewhat different parameters are required to adjust for the difference in temperature.

A more comprehensive view of the dependence of our two parameters on the temperature distribution can be gained by considering the more complete though less structured set of models shown in Figure 4.13. In the inversions, we have assumed a solar wind velocity of 300 km/sec and used the A_{min} data. The values of σ_o and E_o obtained, except for models 1, 2, and 3, are shown in Table 4.3 and they give a fit to the data comparable to the ones above.

Table 4.3

Model	σ_o (mho/m)	E_o(ev)
4	0.45×10^{-2}	0.24
5	0.28x10-2	0.17
6	0.25×10^{-2}	0.13
7	0.31×10^{-2}	0.12
8	0.29×10^{-2}	0.14
9	0.36×10^{-2}	0.13
10	0.46×10^{-2}	0.13

Models 1, 2, and 3 are exceptions since the use of both σ_o and E_o in our inversions would lead to an unstable iteration. Instead we had to use a general inverse operation with a value of $\underline{\varepsilon}$ that essentially kept σ_o fixed in the iteration and forced the activation

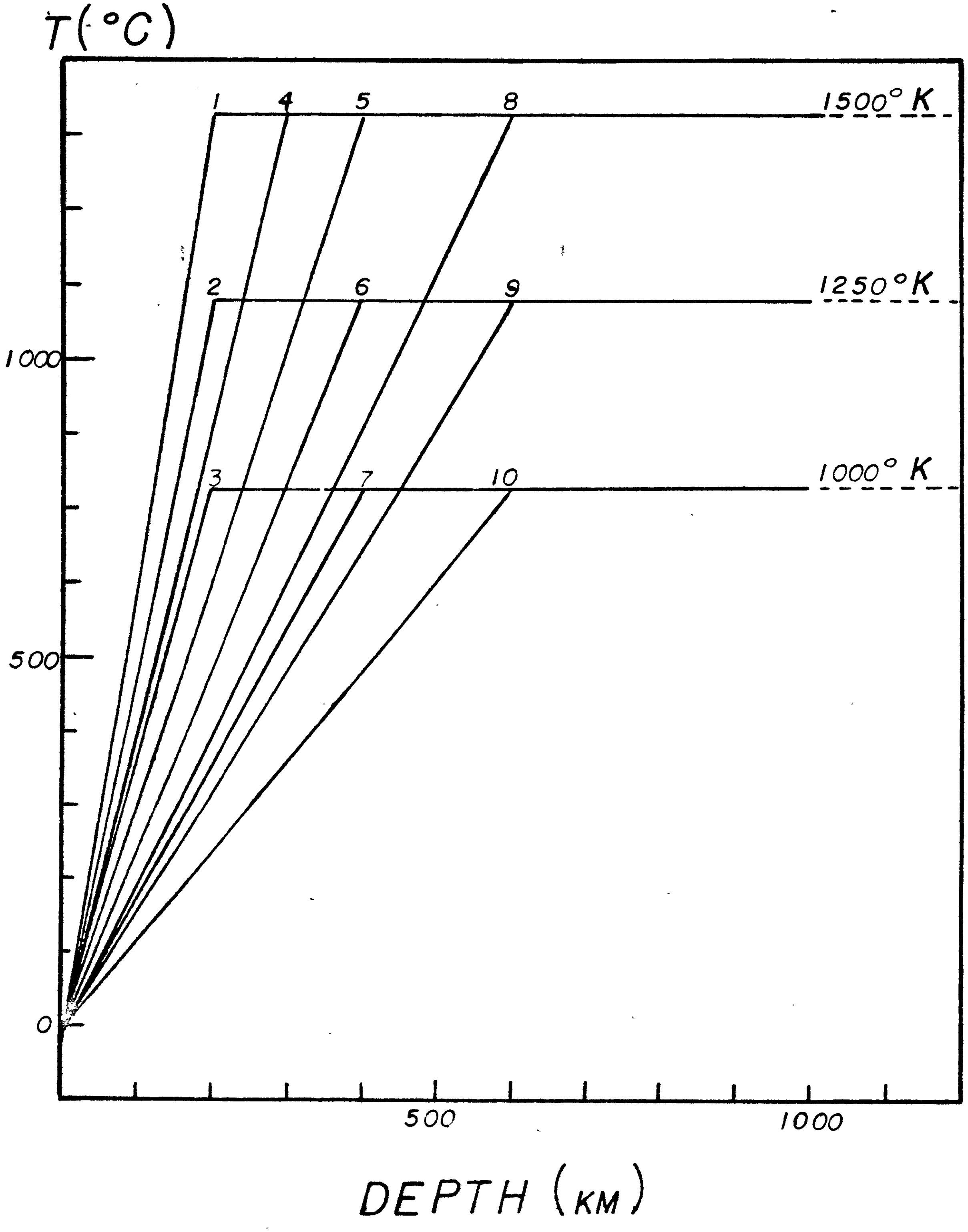
T(°C)
1
4
5
8
1500° K
2
6
9
1250°K
1000
3
7
10
1000° K
500
0
500
1000
DEPTH (KM)

Figure 4.13

energy to assume the value

$$E_o = kT_1 \ln \frac{\sigma_o}{\sigma_1} \qquad (4.4.3)$$

where T_1 is the temperature at depths greater than 200 km, σ_o the initial value of the conductivity prefactor used in the iteration, and σ_1 the average value of the conductivity that must be met at depth greater than 200 km in order for our response to fit the data. Clearly then, the only parameter that can be inferred from such results is σ_1 which had a value of $6.2\text{x}10^{-4}$ mho/m for model 2 and was within 5% of this value for models 1 and 3. The fit to the data for one of these conductivity models is shown in Figure 4.14 and is seen to be very good.

Before closing this section, let me add a final remark:

It is interesting to note that the conductivity obtained at relatively shallow depths inside the moon is of the same order of magnitude as the one found in the earth's crust. However, the conductivity in crustal regions of the earth is determined mainly by the water content in the rocks. Though the majority of the present geochemical and geophysical evidence from the Apollo mission points to a very anhydrous moon, we shall investigate vestigate how well the data can be fitted if the moon is

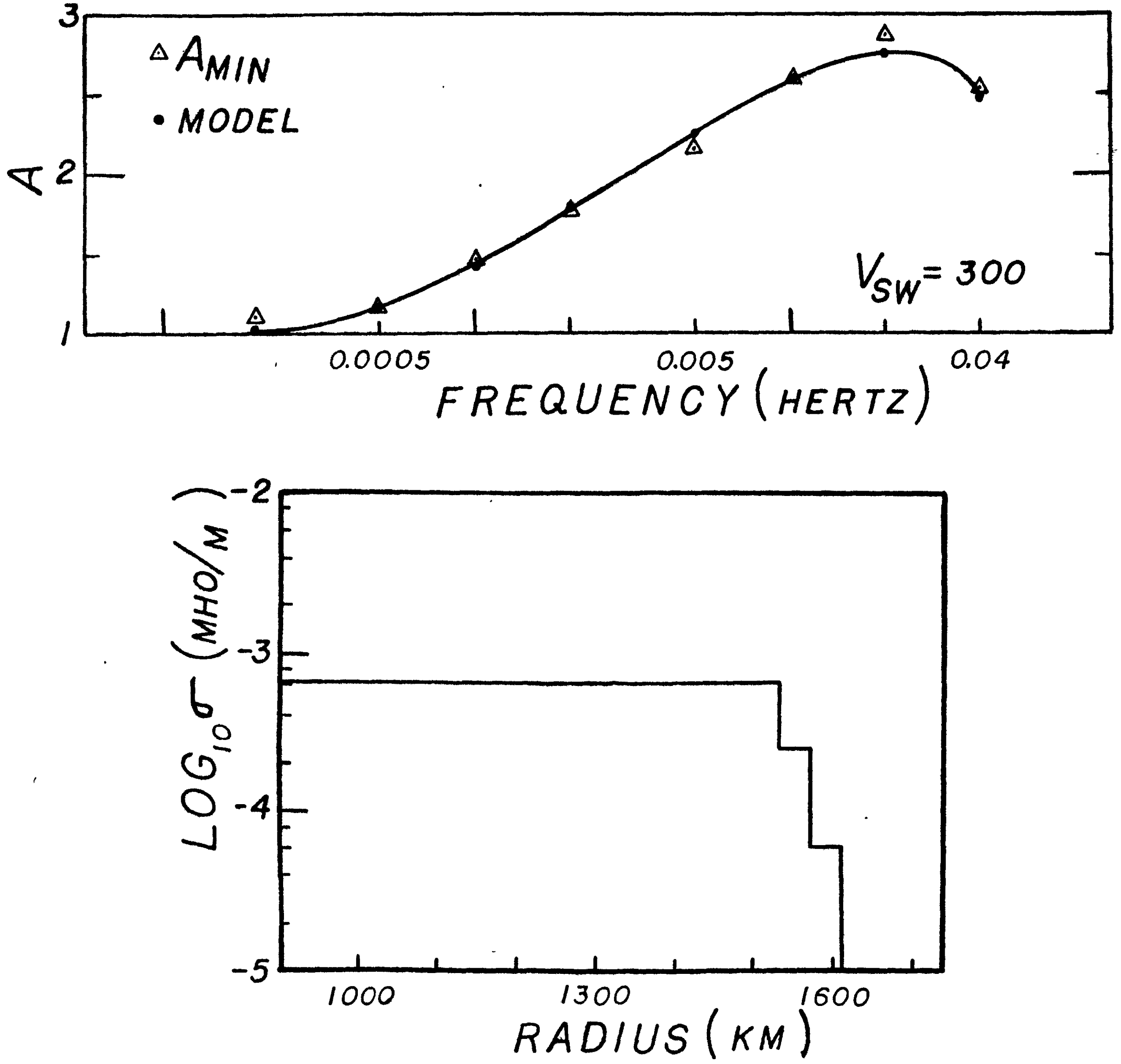

A_{MIN}
MODEL
A
3
2
1
V_{SW} = 300
0.0005
0.005
0.04
FREQUENCY (HERTZ)
$LOG_{10}\,\sigma$ (MHO/M)
-2
-3
-4
-5
1000
1300
1600
RADIUS (KM)

Figure 4.14

assumed saturated with water (except for a non-conducting crust of 60 km). To examine this model, we have assumed the conductivity inside the moon to be related to the temperature through a relation of the form

$$\sigma = \sigma_o e^{-E_o/kt} + \sigma_w e^{0.066/kT} \qquad (4.4.4)$$

The first piece of that expression represents the temperature dependence of the material that eventually dominates the conductivity at the high temperature presumably reached deep inside the moon. The second term accounts for the presence of water. The factor 0.066 ev in the exponent of this expression was determined as follows:

1. The temperature model inside the moon was assumed to be the high temperature model shown in Figure 4.9.

2. The pore pressure was assumed to be the lithostatic pressure and was calculated by assuming a uniform moon of density equal to its mean value.

3. To model the porosity dependence on pressure, we used the conductivity measurement made in the laboratory on a Westerly granite subjected to pressure up to 10 kb at 20°C.

4. The pressure and temperature dependence of the water solution was assumed to follow the laboratory

measurement on a 0.01 molar solution of NaCl.

This type of calculation is very similar to the one made by Brace (1971). who examines the conductivity that would be found deep in the earth's crust if it were saturated with water. The data used in our calculation can be found in this paper and the references quoted therein. The net result for the moon is a decrease of conductivity with depth and is modelled quantitatively by the factor 0.066 in Equation (4.4.4).

The Equation (4.4.2) can be easily extended to include the inversion of the three parameters σ_o, E_o and σ_w. However, in order to insure the stability of the iteration, we had to introduce a value of ε that would effectively permit only two linear combinations of these parameters to participate in the solution. Though most of the resolving power was concentrated in E_o and σ_w, the σ_o parameter had also some power and did vary in the iteration.

The model obtained together with its fit to the data are shown in Figure 4.15. The bottom scale represents the temperature and lithostatic pressure reached at a given depth for our assumed temperature model. The best fit to the data was obtained for $\sigma_o = 0.054$ mho/m, $E_o = 0.49$ ev and $\sigma_w = 0.35 \times 10^{-4}$ mho/m. We note that the match to the A_{min} data is rather poor for this set of parameters.

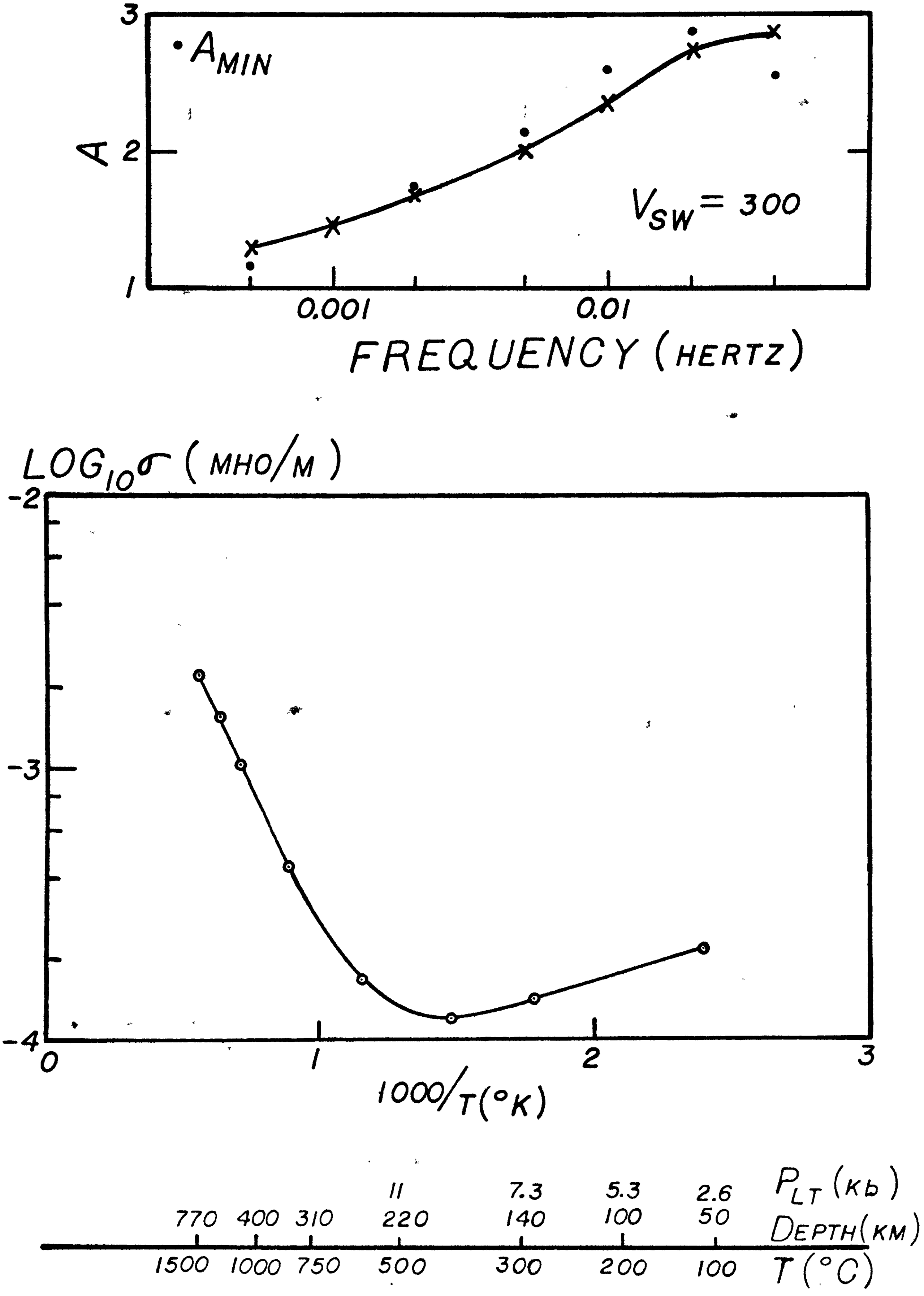
• A_MIN
A
3
2
1
V_SW = 300
0.001
0.01
FREQUENCY (HERTZ)
LOG10 σ (MHO/M)
-2
-3
-4
0
1
2
3
1000/T(°K)
P_LT (Kb)
11 7.3 5.3 2.6
DEPTH(KM)
770 400 310 220 140 100 50
T (°C)
1500 1000 750 500 300 200 100

Figure 4.15

In fact, a much better fit could be obtained if water were absent altogether and only σ_o and E_o were allowed to participate in the iteration. Our inability to obtain a good fit from a water saturated moon is indicative that the porosity decrease with pressure poorly met the variation of conductivity with depth required by the measured response.

4.5 Conclusion with Suggestions for Future Work

The various conductivity models obtained in the last two sections are representative of our present uncertainties arising from our lack of knowledge of the values of various parameters that influence the data. Yet all these models seem to possess some common characteristics.

We note first that a conductivity level of 10^{-4} mho/m seems to be consistently reached in the upper 150 to 200 km of the moon. Moreover, the conduction level does not generally increase by more than about one order of magnitude between 200 and 700 kilometers. Also, the conductivity below about 800 km is generally unresolved by the data. Though our studies of the A_z data from the Apollo 12 site does not rule out models in which a conduction level slightly less than 10^{-2} mho/m is reached in the top 700 km of the moon, we feel that a lower conduction level is more likely since the A_z component lies near the direction of the tangential component of the remanent field at this site. Moreover, the low frequency data at the Apollo 15 site tends to agree with the A_{min} and A_y values from the Apollo 12 LSM and these data yield a conduction level consistently less than 2×10^{-3} mho/m in the upper 700 km of the moon.

If we attempt to extract the maximum temperature reached in the moon from the conduction level, we face such large uncertainties that we cannot rule out a temperature either substantially higher or lower than 1000°C. To narrow the allowable temperature range, a great deal more work must be done to obtain and understand the conductivity-temperature relationship of mineral assemblages likely to form the bulk lunar composition.

Yet, the fact that the conduction level does not vary much between 200 and 700 km inside the moon seems to put a rather stringent constraint on either the conductivity-temperature relationship or the temperature structure at these depths. We have examined this question in the last section and found that if a sharp thermal gradient is maintained at these depths, a very low activation energy conduction mechanism is required. In fact, even if the sharp thermal gradient is maintained only in the top 300 km, an activation energy of only about 0.24 ev is required. For models more in accord with the one proposed by Toksöz et al. (1972) and in which the sharp thermal gradient extends to depths greater than 500 km, the activation energy required is generally smaller than 0.2 ev. A low of 0.09 ev can be reached depending upon the set of data and source parameters used in the inversion. Moreover, these results do not seem very sensitive to the maximum temperature reached in the lunar interior.

Low activation energy conduction mechanisms are often observed in terrestrial and lunar* rocks (see, for example the low temperature end of the lunar sample σ versus inverse T curve shown in Figure 4.8). For most common rocks, such conduction mechanisms are observed only at fairly low temperatures. Moreover, they have an associated conductivity prefactor generally much smaller than the level of a few times 10^{-3} mho/m that would be required for the rocks inside the moon. Thus, there are definite problems with our inferred model parameters

We note that low activation energy is often associated with impurities in the major mineral component of the rocks. Another possible interpretation is that

---

*Preliminary measurements of the conductivity-temperature relationship in lunar rocks by Schwerer et al. (1971) were plagued by thermal hysteresis that was subsequently attributed to a carbon contamination of the sample. The implication of these uncertainties is that, at the present stage, very few results can be relied on.

the rocks contain a small amount of a mineral whose conductivity is high with a weak dependence on the temperature. A fairly common terrestrial mineral that possesses these characteristics is magnetite. Above 119°K, its conductivity is of the metallic type and has a value of about 2×10^{-4} mho/m (Miles et al., 1957). The conductivity of hematite doped with a small amount of titanium can also exhibit a weak dependence on temperature and a fairly high conduction level (Morin, 1951).

The fact that our low values of E_o and moderate value of σ_o have not been observed in the Apollo samples might be the result of a significant differentiation that has occurred during the moon's history. This differentiation could have depleted the lunar surface rocks of a highly conducting yet minor mineral component. The enrichment of this component at moderate depth could account for our inferred characteristics.

If a minor mineral dominated the conductivity at moderate depth inside the moon we cannot determine from the magnetic data the major mineral component at these depths. We might even have difficulty predicting the concentration of the minor mineral since the bulk conductivity probably depends on the connectivity of its conduction paths, a factor over which we have little control.

The differentiation might partly explain a difficulty that could result if the near surface rocks have the same conductivity parameters that we inferred from the LSM data at moderate depth. From Figure 4.8 we note that the conductivity that we would extrapolate for rocks near the surface would be of the order of 10^{-5} mho/m. But, if such a high value were realized, a strong toroidal H magnetic field would be expected, contradicting our observations. However, differentiation might not be required to explain the absence of this field. All we need is that the moon be covered by a layer of resistivity-thickness product greater than about 5×10^{11} ohm-m-km. On the basis of high frequency electromagnetic data (136 Mhz to 75 Ghz), Strangway has inferred the existence of a powdered rock layer of conductivity in the range 10^{-13} to 10^{-16} mho/m near the lunar surface. Therefore, the thickness of this dust layer need only to be less than about 1 meter to explain the absence of perturbaion. Also the intense scattering of seismic waves that is observed on the moon has been widely interpreted to imply the existence of poorly consolidated material near the surface. Evidently, if the moon is dry, the increased porosity will break up the conduction path and might result in a greatly reduced conductivity, even if the rocks near the surface had the same composition as those at moderate depth.

An alternative explanation for the absence of strong variation in the electrical conductivity at depths below 200 km would be to assume that there is no significant thermal gradient at these depths. We have examined this possibility in the last section and we found that indeed a reasonably good fit to the data can be obtained in that case. Such thermal models do not pose any significant constraint on the activation energy of the material at these depths. Kuckes (1974) has also recently investigated this question. He assumed at the onset that the activation energy is higher than about 1 ev and searched for temperature model yielding a good fit to the magnetic data. He also found that only the top 200 km can maintain a strong thermal gradient in order to meet his constraint on the activation energy.

Temperature models with small thermal gradients below 200 km have been proposed by Tozer (1972). From consideration of material rheology under physical conditions likely to be found inside the moon, he concluded that a convecting core probably exists within 200-300 km of the surface. By assuming the Nabarro-Herring creep to be the dominant deformation mechanism and by inferring a viscosity of 10^{21} poise in the convection region, he was able to establish a lower bound of 5×10^{-5} mho/m on the electrical conductivity that would be permissible inside the moon. Since we deduce a conductivity level of about 6.2×10^{-4} mho/m when such a temperature model is assumed, we cannot reject his hypothesis on the basis of the magnetic data alone. However, the lower bound on the conductivity quoted by Tozer is not very well established in view of the fact that the Nabarro-Herring creep is only one member of a set of creep processes that could have participated in such a convection. Also, a viscosity of about 10^{21} poise is often associated with regions of the earth's upper mantle where creep is presumed to be an important deformation mechanism (see, for example, Weertman, 1970). But these regions of the upper mantle are characterized by values of the electrical conductivity several orders of magnitude greater than that we would infer for the moon. However, the different physical conditions in the earth from those in the moon might perhaps account for some of these discrepancies. Nevertheless, at this point, a widely recognized objection to the calculation of Tozer is the implication of a rapid cooling of the lunar interior after the moon's formation. This cooling rate would seem to contradict the substantial period of time (0.7 to 1.4 by) during which the basalt that flooded the maria was kept near its melting temperature in the early history of the moon (Ringwood et al., 1970). Until this objection can be countered, the results of Tozer will remain inconclusive

Thus, our results seem to lead to somewhat puzzling conclusions. A substantial effort should be devoted in the future to either confirm or deny their validity. We have pointed out in the text various directions that can be followed in order to assess the accuracy of the theory and the possible noise contribution to the data.

Let me just add one more suggestion. Future analysis should include in the inversion an accurate value for the position of the LSM, the solar wind velocity and the distribution of the wave normal to the incident fluctuations. The value of the solar wind velocity probably can be obtained from the various instruments aboard spacecrafts in the solar wind or from the solar wind spectrometer at the Apollo 15 site. The small remanent field at this site probably does not influence the velocity. The distribution of the wave normal may be more difficult to reconstruct. However, the situation is not completely hopeless in view of the preliminary results of Daily (1973) which tend to indicate that during a good Alfven wave regime, the wave normal tends to align along the ambient magnetic field direction. If this is the case, then, during such periods the problem would reduce to that of finding the average direction of the magnetic field over a period appropriate for the frequency range of interest. Alternatively, we might be able to extract some of this information from the strong dependence of the high frequency response in the downstream cavity on the value of these parameters. We visualize, for example, a situation where Explorer 35 and the LSM are on the upstream side of the moon when a subsatellite is in the downstream cavity. The high frequency response at the subsatellite possibly could be used to extract some of the required information which would in turn be fed to the inversion of the LSM data. However, it might be impractical to extract useful information from the subsatellite due to its relatively short orbital period and consequent short sampling time, coupled with our inferred strong dependence of the high frequency signal in the void on the distance from the plasma-vacuum interface.

Appendix I

The Noise from the Solar Wind Dynamic Pressure Fluctuation at the Apollo 12 Site

We can not estimate accurately the effect of the solar wind dynamic pressure fluctuation on the remanent field around the Apollo 12 site due to our incomplete knowledge of the structure of the remanent field itself. Moreover, the solar wind data necessary to back up such an estimate are generally not available. However, we may be able to extract the order of magnitude of the solar wind pressure effect from some empirical relations* that have appeared recently in the literature.

We note first that Dyal et al. (1972) induced an empirical relation between the change in the magnetic field at the site and the solar wind dynamic pressure.

They have expressed this relationship as follows:

---

* The cgs and Gaussian system of units is used in this note.

$$\frac{\Delta\vec{B}\cdot\Delta\vec{B}}{8\pi} = 0.01\ \rho\vec{V}_{sw}\cdot\vec{V}_{sw} \tag{AP-I.1}$$

where

$$\Delta\vec{B} = \vec{B} - \vec{B}_E - \vec{B}_s$$

and $\vec{B}$ is the total field at the site, $\vec{B}_E$ is the field measured by Explorer 35, $\vec{B}_s$ is the unperturbed remanent field and ρ is the solar wind density. Hourly averages of $\vec{B}$ and $\vec{B}_E$ were used to estimate $\Delta\vec{B}$ so little contamination from the induced field is expected. At first glance Equation (AP-I.1) appears to be an outgrowth of the conservation equations. However, we can make such an interpretation only if the square of difference of $|\vec{B} - \vec{B}_E|$ and $|\vec{B}_s|$ had been related to the dynamic pressure (see, for example, Siscoe et al., 1971).

During a period when the solar wind magnetic field fluctuations were predominantly Alfven wave, Belcher et al. (1971) found the following relation between the solar wind magnetic fluctuation, $\delta\vec{B}_{sw}$, and the fluctuation in the solar wind velocity, $\delta\vec{V}_{sw}$:

$$\delta\vec{B}_{sw} = \pm 4.6\ \rho^{1/2}\delta\vec{V}_{sw} \tag{AP-I.2}$$

In order to relate these two empirical equations, let us assume that the modulation in the dynamic pressure due to velocity fluctuations along the average direction of the solar wind velocity is associated with a perturbation

$\delta\vec{B}_{mod}$ of the remanent field. If we linearize Equation (AP-I.1), that is, we assume $\Delta\vec{B} = \Delta\vec{B}_o + \delta\vec{B}_{mod}$ and $\vec{V}_{sw} = \vec{V}^o_{sw} + \delta\vec{V}_{sw}$, and if we collect the first order terms we obtain

$$\frac{\Delta\vec{B}_o \cdot \delta\vec{B}_{mod}}{8\pi} = 0.01\ \rho\vec{V}_{sw}\cdot\delta\vec{V}_{sw} \qquad \text{(AP-I.3)}$$

If we define the direction of the unit vectors $\vec{a}_b$ and $\vec{a}_v$ parallel respectively to $\Delta\vec{B}_o$ and $\vec{V}^o_{sw}$ and using the equation obtained by collecting zero-order terms, we obtain

$$\vec{a}_b\cdot\delta\vec{B}_{mod} \simeq 0.5\ \rho^{1/2}\ \vec{a}_v\cdot\delta\vec{V}_{sw}$$

which, using Equation (AP-I.2), becomes (AP-I.4)

$$\approx 0.09\ \vec{a}_v\cdot\delta\vec{B}_{sw}$$

Consequently we expect a ratio of the maximum to minimum tangential amplification factor smaller than about 1.1. However, Sonett <u>et al</u>. (1972) have observed a ratio equal to about 1.5 at 0.005 Hz. It would seem difficult to interpret such a high value on the basis of our rough amplitude estimate. There are two observations that also seem inconsistent with an interpretation in terms of pressure fluctuation noise. One: Sonett et al. found that the direction of maxima in the amplification factor does not align with the direction of the tangential magnetic field component for frequencies below about 0.002 Hz. Second: they also found two directions of maxima in the amplification factor at 0.04 Hz. However, more experimental and theoretical work is needed before we can properly assess the contribution of pressure fluctuations in the anisotropic response observed at the Apollo 12 site.

Appendix II

The Field Inside the Moon

The solution of Maxwell's equations inside a layered sphere has been discussed frequently in the literature. We shall use here the results and notation of Stratton (1941) and shall content ourselves to describe the quantities L_n and T_n that permit us to write the field as in Equations (2.3.1).

If we assume the moon to be formed of s layers bounded by the radii $r_1, r_2, \ldots, r_s$ where $r_s = R_M$, then L_n and T_n can be expressed as follows:

$$L_n = 1 + D_2/D_1 \qquad \text{(Ap. II.1)}$$

where

$$\begin{vmatrix} D_1 \\ D_2 \end{vmatrix} = M_n(k_s r_s) M_n^{-1}(k_s r_{s-1}) M_n(k_{s-1} r_{s-1}) \cdots \begin{vmatrix} j_n(k_1 r_1) \\ k_1 r_1 j'_n(k_1 r_1) \end{vmatrix}$$

and where the 2 x 2 matrix $M_n(z)$ is given by

$$M_n(z) = \begin{vmatrix} j_n(z) & n_n(z) \\ z j'_n(z) & z n'_n(z) \end{vmatrix} .$$

Similarly we have

$$T_n = F_1/F_2 \qquad \text{(Ap. II.2)}$$

where

$$\begin{vmatrix} F_1 \\ F_2 \end{vmatrix} = N_n(k_s r_s) N_n^{-1}(k_s r_{s-1}) N_n(k_{s-1} r_{s-1}) \cdots \begin{vmatrix} k_1 r_1 j_n(k_1 r_1) \\ \frac{1}{k_1 r_1}[k_1 r_1 j_n(k_1 r_1)]' \end{vmatrix}$$

where the 2 x 2 matrix $N_n(z)$ is given by

$$N_n(z) = \begin{vmatrix} zj_n(z) & zn_n(z) \\ \frac{1}{z}[zj_n(z)]' & \frac{1}{z}[zn_n(z)]' \end{vmatrix}$$

where $k_i = (i\omega\mu_o\sigma_i)^{1/2}$ is the propagation constant of the i^{th} layer

and $n_n(z)$ and $j_n(z)$ are the spherical Bessel functions and the prime stands for the derivative with respect to the argument. The inverses of M_n and N_n can be found easily and simplified by using the Wronskian relationship for spherical Bessel functions.

APPENDIX II

Response in the Void Cavity to a Magnetic Discontinuity in the Solar Wind

We would like to calculate the field in the cylindrical void region when a magnetic discontinuity is convected in the polar wind and compare the result with the measurements exhibited in Figure 2.4. During these measurements, Explorer 35 was in the void region behind the moon and both the moon and Explorer 33 were in the free streaming solar wind. We shall assume that Explorer 35 was sufficiently far downstream that its magnetic field measurements were uninfluenced by the conductive lunar interior [see Sonett et al. (1970), for a discussion of this assumption]. We shall also assume the incident solar wind magnetic field to be homogeneous in planes subtending an angle ψ with the direction of the solar wind velocity. However, we have only one relation to determine ψ and V_{sw}, namely, the delay in arrival time of the discontinuity at both satellites ($\simeq$ 15 minutes). From the difference in the X and Y coordinates of each satellite, ($\Delta X \simeq 22R_E$, $\Delta Y \simeq 48R_E$), we obtain

$$\Delta T = 900 \text{ sec} = \frac{\Delta X + \Delta Y \tan\psi}{V_{sw}} \qquad \text{(AP.II. 1)}$$

If we assume $\psi = 0$, we obtain $V_{sw} = 150$ km/sec. This value is substantially lower than that of the solar wind velocity ($\simeq$350 km/sec). Nevertheless, first we make a calculation assuming this low solar wind velocity and then present a brief heuristic argument to show that even for very high solar wind velocities, the predicted dilatation in the rise time of the Z component remains of the same order of magnitude as the one observed.

If $\psi = 0$, then, in the XZ plane (see note, p. 53 and the table of Figure 2.4) field predicted by Equation (2.4.1) is

$$H_Z = H_\rho = \frac{H_{ox}(\omega) I_1'(k_{//}\rho) e^{ik_{//}z}}{I_1'(k_{//} a)}$$

$$H_Y = H_\phi = 0 \qquad \text{(AP.II.2)}$$

and

$$H_X = -H_z = \frac{-H_{ox}(\omega) I_1(k_{//}\rho) e^{ik_{//}z}}{I'_1(k_{//}a)}$$

where the Fourier transform of $H_{ox}(\omega)$ is assumed to be the signal observed at Explorer 33. The Fourier transform of these expressions have been evaluated and are presented graphically in Figure AP-III. The dilatation in the rise time of the Z is about the same as the one observed and the peak in the X is also along the same direction as observed.

Now, let us consider the case of a high solar wind velocity. From Equation (AP.I

$$\frac{\Delta T}{\Delta Y} \simeq \frac{\tan\psi}{V_{sw}} .$$

If the solar wind is allowed to reach very high values, but the above ratio is kept constant, we obtain from

Equation (2.4.1)

$$H_Z = H_\rho \simeq H_{ox}(\omega)e^{ik_{//}z} \sum_{m=1,3,\ldots} \frac{J_m(\alpha\omega)}{\alpha\omega}$$

where

$$\alpha = \frac{\Delta TR_M}{\Delta Y}$$

We can easily show that the main contribution to the dilatation in the rise time of the Z component will come from the term m = 1. This term has a Fourier transform given by

$$\frac{2}{\pi\alpha}\,[1 - (t/\alpha)^2]^{1/2} \qquad \text{for } |t| \leq \alpha$$

$$0 \qquad |t| \geq \alpha$$

The convolution of this Fourier transform with the source field adds about $2\alpha \simeq 10$ sec to the rise time of the Z component, thus yielding a total value for the rise time equal to about a third of what is observed.

Since actual values for ψ and V_{sw} for the discontinuity are probably between these two limits* described above, we conclude that the surface wave solution of the field in the void does predict, at least qualitatively at this time, the observed dilatation in the rise time of the Z component and the small peak in the X component.

---

*Negative value of ψ can render V_{sw} smaller than 150 km/sec, but such a case must be considered improbable.

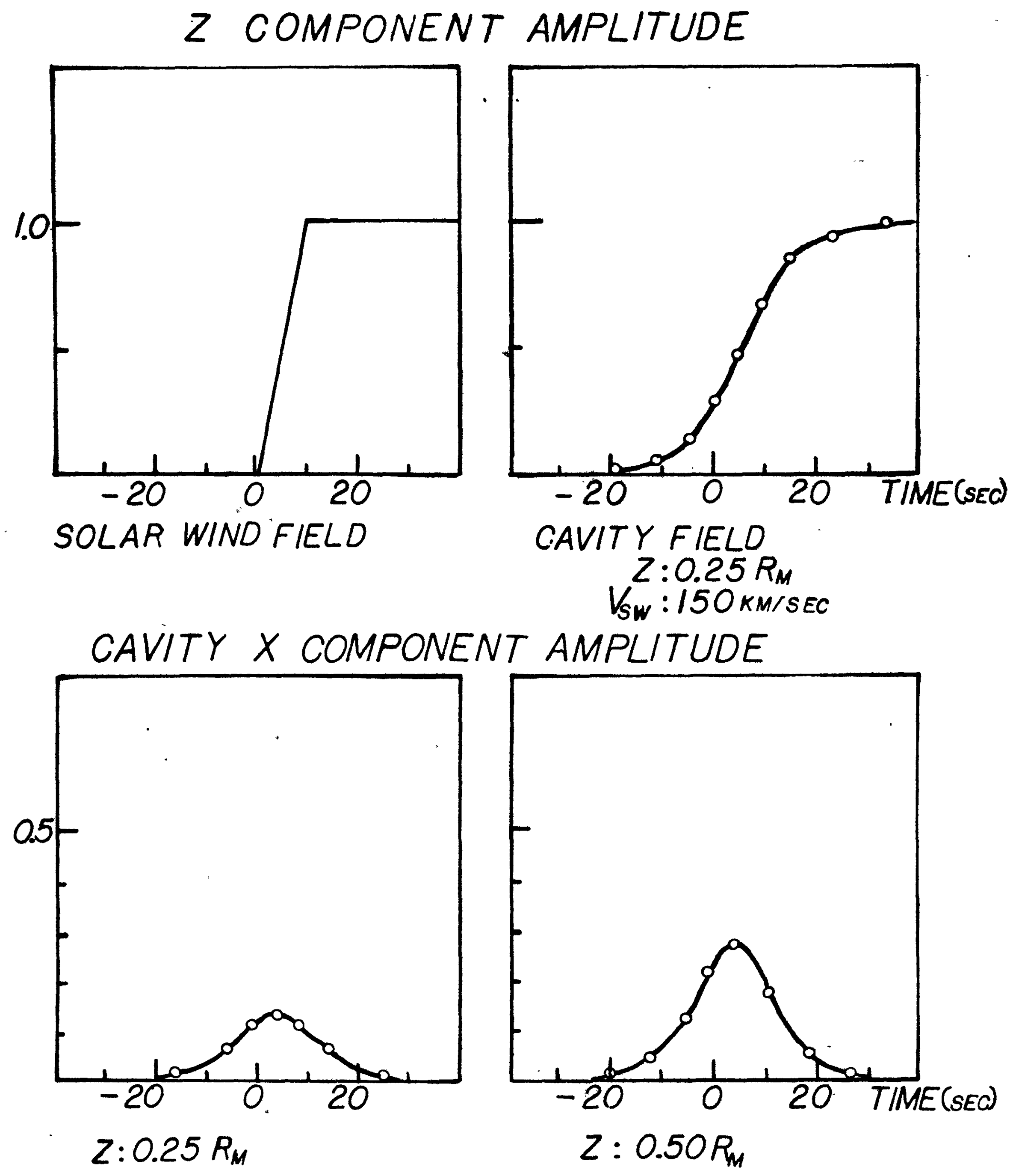

Figure AP-III

Appendix IV

The Multipole-cylindrical Waveguide Mode Representation of the End Effect Field

Let us consider the free space magnetic field of a magnetic multipole (neglecting displacement current). This field can be written as follows:

$$\vec{H}_M = \nabla \times \nabla \times [t^{\sigma}_{nm} \frac{R_M^{n+2}}{r^n} P_n^m(\cos\theta) \left\{ {\sin \atop \cos} \right\} m\phi \vec{a}_r] \qquad \text{(Ap. IV.1)}$$

In order to satisfy the condition that the magnetic field has a vanishing normal component at the boundary of the cylinder, we must find a series of spherical TF modes, regular at the origin such that the sum of the normal component of the magnetic field of the TE modes and that of the multipole add up to zero at the boundary. We can express this field representation as follows:

$$\vec{H}_C = \sum_{p=m}^{\infty} \nabla \times \nabla \times (a^{\sigma}_{nmp} \frac{r^{p+1}}{R_M^{p-1}} P_p^m(\cos\theta) \left\{ {\sin \atop \cos} \right\} m\phi \vec{a}_r \qquad \text{(Ap. IV.2)}$$

The coefficients in AP. IV. 2 can be found by using the following dual pair of identities:

$$\int_0^{\infty} t^{\ell} K_m(t\rho) \cos(tz) dt = i^{\ell-m} \frac{\pi}{2} (\ell-m)! \; r^{-\ell-1} P_{\ell}^m(\cos\theta) \qquad \text{(Ap. IV.3)}$$

if m + ℓ is even

$$\int_0^\infty t^\ell K_m(t\rho)\sin(tz)dt = i^{\ell-m-1}\,\frac{\pi}{2}(\ell-m)!\; r^{-\ell-1}P_\ell^m(\cos\theta)$$

if m + ℓ is odd

$$\cos tz\, I_m(t\rho) = \sum_{\ell=m}^{\infty} i^{\ell-m}\,\frac{(tr)^\ell}{(\ell+m)!}\,P_\ell^m(\cos\theta)$$

if ℓ + m is even

(Ap. IV.3)

$$\sin tz\, I_m(t\rho) = \sum_{\ell=m+1}^{\infty} i^{\ell-m-1}\,\frac{(tr)^\ell}{(\ell+m)!}\,P_\ell^m(\cos\theta)$$

if ℓ + m is odd

where I_m and K_m are the hyperbolic Bessel functions. These identities are consistent with the Morse et al. definition (p. 1325) of the Legendre functions and are derived by Cooke (1956, 1962).

Let us assume n + m is even in Equation (Ap. IV.1) and consider the following cylindrical TE magnetic field:

$$\vec{H}_1 = \nabla \times \nabla \times \psi\, \vec{a}_z \qquad \text{(Ap. IV.4)}$$

where

$$\psi = b_{nm}^\sigma \int_0^\infty t^{n-1}K_m(t\rho)\,\sin(tz)dt$$

$$b_{nm}^\sigma = \frac{2}{\pi}\,\frac{nt_{nm}^\sigma}{i^{n-m+2}}\,\frac{R_M^{n+2}}{(n-m)!}\left\{\begin{matrix}\sin\\ \cos\end{matrix}\right\} m\phi$$

By using the first pair of identities in Equation (Ap. IV.3) and making liberal use of Legendre function identities (in addition to applying the operator $\nabla \times \nabla \times$ to cancel some terms not contributing to the field), we can show that $\vec{H}_1 = \vec{H}_M$.

In order to cancel the normal component of the magnetic field at the boundary of the cylinder, we can add to $\vec{H}_1$, the following TE magnetic field:

$$\vec{H}_2 = \nabla \times \nabla \times \Phi \, \vec{a}_z \qquad \text{(Ap.IV.5)}$$

where

$$\Phi = -b^{\sigma}_{nm} \int_0^{\infty} t^{n-1} \frac{K'_m(tR_M)}{I'_m(tR_M)} I_m(t\rho)\sin(tz)dt$$

By following a process similar to the one described above but this time using the second pair of identities in Equation (Ap.IV.3) and integrating term by term, we can show that $\vec{H}_2 = \vec{H}_c$, provided that we set

$$a^{\sigma}_{nm} = -\gamma^{e}_{nm}\,\gamma^{e}_{mp}\,h_{nmp}\,N_m(n+p) \qquad \text{(Ap.IV.6)}$$

where

$$h_{nmp} = \frac{t^{\sigma}_{nm}\; n\; i^{p-m}}{(n-m)!\,(p+m)!\,(n+p+1)\,(p+1)} \left(\frac{n+p}{2}\right)! \; \left(\frac{n+p}{2}\right)!$$

The notation for γ^{e}_{ij} is explained in Equation (2.4.1) and the constants $N_m(2\ell)$ are defined in Appendix V.

The spherical TE electric field associated with $H_M + H_c$ does not have a vanishing tangential electric field component on the boundary of the cylinder. In order to meet this boundary condition, some spherical TM modes must be added. They are represented by the Φ^{σ}_{nm} potential in Equation (2.4.3), whereas the electric field associated with the electric multipole is represented by the Λ^{σ}_{nm} potentials in that equation. Since the technique used to find these potentials is very similar to the one described above, the details of the derivation are omitted.

An alternative representation of the field in terms of cylindrical waveguide modes can also be obtained. We note that the sum of the two cylindrical TE potentials can be given as follows:

$$\Psi^{\sigma}_{nm} = \psi + \Phi = \frac{b^{\sigma}_{nm}}{2}\int_{-\infty}^{\infty} t^{n-1}\frac{[K_m(tp)I'_m(tR_M)-K'_m(tR_M)I_m(tp)]}{I'_m(tp)} \cdot \sin tz \, dt \qquad \text{(Ap.IV.7)}$$

where we have used the definition of hyperbolic Bessel functions (Watson, 1966) to extend the integration from $-\infty$ to $+\infty$. The integrand is analytic and one-value and has simple poles at $\pm i\beta_{m\ell}$, $J'_m(\beta_{m\ell}) = 0$. Using the residue theorem and noting that the integral vanishes on the semi-circle at infinity, we obtain, for $z > 0$

$$\Psi^{\sigma}_{nm} = \frac{2n t^{\sigma}_{nm} R_M^2}{(n-m)!} \sum_{\ell} (\beta_{m\ell})^{n-2} \frac{J_m(\beta_{m\ell}\rho/R_M)\, e^{-\beta_{m\ell} z/R_M}}{(1-\frac{m^2}{\beta_{m\ell}^2}) J_m^2(\beta_{m\ell})} \left\{ \begin{matrix} \sin \\ \cos \end{matrix} \right\} m\phi \tag{Ap.IV.8}$$

The Wronskian relationship for Bessel functions was used to obtain this last expression. The electric field can also be treated in a similar way and the total field is expressed in Equation (2.4.4).

Appendix V.

The Constants $M_m(2p)$ and $N_m(2p)$

Several problems in potential theory, involving spheres inside cylinders, required the same set of definite integrals that we encountered in Chapter II (see, for example, Cooke, 1962, and Smythe, 1963, 1964, 1968). Due to the general usefulness of these integrals and since only a partial listing appears in the literature, we include here a more comprehensive table of their values. We define

$$M_m(2p) = \frac{2}{\pi p!p!} \int_0^\infty \frac{t^{2p}}{I_m^2(t)}\, dt \equiv \frac{2(2p+1)}{\pi p!p!} \int_0^\infty t^{2p} \frac{K_m(t)}{I_m(t)}\, dt$$

and

$$N_m(2p) = \frac{2}{\pi p!p!} \int_0^\infty \frac{t^{2p+1}}{(I_m')^2} \left(\frac{1}{t} + \frac{m^2}{t^3}\right) dt$$

$$\equiv \frac{-2(2p+1)}{\pi p!p!} \int_0^\infty \frac{t^{2p} K_m'(t)\, dt}{I_m'(t)}$$

The above identities can be derived by integrating the left hand side and then using the Wronskian relationship. To evaluate these integrals, we have proceeded as follows:

For $p \leq 30$, an analytical expression was used. Following a technique devised by Watson (1930), we can derive the following identities:

$$\int_0^\infty \frac{t^{2p}}{I_m^2}\, dt = \sigma \sum_{n=0}^{\infty} \frac{(n\sigma + 0.5\sigma)^{2p}}{I_m^2(n\sigma + 0.5\sigma)}$$

$$+ \pi(-1)^{p-m} \sum_{\ell}^{\infty} \frac{\alpha_{m\ell}^{2p-1}}{J_{m+1}^2(\alpha_{m\ell})} \left[\frac{\pi\alpha_{m\ell}/\sigma}{\cosh^2(\pi\alpha_{m\ell}/\sigma)}\right.$$

$$\left. - \frac{(2p+1)\, e^{-\pi\alpha_{m\ell}/\sigma}}{\cosh(\pi\alpha_{m\ell}/\sigma)} \right]$$

and

$$\int_0^\infty \frac{t^{2p}}{(I_m')^2}\, dt = \sigma \sum_{n=0}^{\infty} \frac{(n\sigma + 0.5\sigma)^{2p}}{[I_m'(n\sigma + 0.5\sigma)]^2}$$

$$- \pi(-1)^{p-m} \sum_{\ell=1}^{\infty} \frac{(\beta_{m\ell})^{2p+3}}{(\beta_{m\ell}^2 - m^2)^2 J_m^2(\beta_{m\ell})} \left[\frac{\beta_{m\ell}\pi/\sigma}{\cosh^2(\pi\beta_{m\ell}/\sigma}\right.$$

$$\left. - \left(2p + \frac{\beta_{m\ell}^2 - 3m^2}{\beta_{m\ell}^2 - m^2}\right) \frac{e^{-\pi\beta_{m\ell}/\sigma}}{\cosh(\pi\beta_{m\ell}/\sigma)} \right]$$

where $\alpha_{m\ell}$ and $\beta_{m\ell}$ are the roots of J_m and J_m' respectively and σ is an arbitrary positive number.

We used the Royal Society Mathematical Tables (1960) to find the roots of the Bessel functions and their associated values. The above series were evaluated numerically for different values of σ. The results agree to more than 8 digits. For $50 \geq p \geq 25$, we used the asymptotic formula for the product of hyperbolic Bessel functions (see, for example, Olver , 1965). In the overlapping domain $30 \geq p \geq 25$, the results were also found to agree to more than 8 digits.

Note: $N_o(2p) = M_1(2p)$, so the values of $N_o(2p)$ can be found from $M_1(2p)$

Table AP-V : Values of $M_m(2p)$

m p	0	1	2	3
0	0.87069013	-	-	-
1	1.2354675	4.7809450	-	-
2	1.6471421	3.0011759	23.091507	-
3	2.0014447	2.9004477	9.1317676	105.75794
4	2.3046888	3.0068912	6.7887287	30.338664
5	2.5708931	3.1638910	5.9624110	18.231357
6	2.8105215	3.3334854	5.6044969	13.777881
7	3.0303496	3.5038177	5.4447761	11.587752
8	3.2347572	3.6708310	5.3845295	10.336636
9	3.4266969	3.8331760	5.3798713	9.5556150
10	3.6082622	3.9905271	5.4086175	9.0401532
11	3.7810044	4.1429611	5.4584810	8.6879044
12	3.9461150	4.2907110	5.5221743	8.4423901
13	4.1045347	4.4340622	5.5951411	8.2700663
14	4.2570235	4.5733082	5.6744117	8.1498362
15	4.4042059	4.7087308	5.7579850	8.0678099
16	4.5466033	4.8405929	5.8444761	8.0144936
17	4.6846564	4.9691357	5.9329054	7.9831931
18	4.8187416	5.0945793	6.0225677	7.9690624
19	4.9491838	5.2171237	6.1129481	7.9685147
20	5.0762658	5.3369505	6.2036664	7.9788426
21	5.2002352	5.4542245	6.2944395	7.9979687
22	5.3213107	5.5690959	6.3850554	8.0242747
23	5.4396865	5.6817015	6.4753548	8.0564838
24	5.5555358	5.7921662	6.5652179	8.0935769
25	5.6690141	5.9006043	6.6545550	8.1347322
26	5.7802615	6.0071206	6.7432992	8.1792806
27	5.8894049	6.1118117	6.8314013	8.2266732
28	5.9965595	6.2147663	6.9188258	8.2764559
29	6.1018303	6.3160666	7.0055477	8.3282508
30	6.2053134	6.4157884	7.0915504	8.3817414
31	6.3070970	6.5140023	7.1768239	8.4366609
32	6.4072623	6.6107736	7.2613632	8.4927835
33	6.5058843	6.7061633	7.3451674	8.5499172
34	6.6030321	6.8002282	7.4282388	8.6078979
35	6.6987700	6.8930214	7.5105820	8.6665848
36	6.7931578	6.9845926	7.5922037	8.7258569
37	6.8862510	7.0749883	7.6731119	8.7856096
38	6.9781015	7.1642523	7.7533160	8.8457524
39	7.0687578	7.2524256	7.8328260	8.9062067
40	7.1582654	7.3395470	7.9116527	8.9669041
41	7.2466669	7.4256530	7.9898074	9.0277850
42	7.3340024	7.5107780	8.0673015	9.0887973
43	7.4203094	7.5949545	8.1441467	9.1498953
44	7.5056235	7.6782133	8.2203549	9.2110392
45	7.5899783	7.7605837	8.2959379	9.2721939
46	7.6734054	7.8420934	8.3709073	9.3333286
47	7.7559348	7.9227685	8.4452751	9.3944162
48	7.8375948	8.0026342	8.5190526	9.4554330
49	7.9184124	8.0817141	8.5922513	9.5163580
50	7.9984131	8.1600309	8.6648824	9.5771729

Table AP-V : Values of $M_m(2p)$ (continued)

m	4	5	6	7
p				
4	470.30450	-	-	-
5	105.56602	2052.4525	-	-
6	53.121319	377.86834	8840.6117	-
7	35.112697	163.37305	1378.4996	37714.041
8	26.603247	95.801312	522.12060	5097.6836
9	21.828804	65.888357	274.86722	1717.1999
10	18.847131	49.917485	172.85264	819.69548
11	16.845010	40.311179	121.43253	474.42728
12	15.429216	34.038063	91.938586	310.38676
13	14.388950	29.689158	73.423098	220.92138
14	13.602071	26.534852	61.001654	167.13928
15	12.993382	24.165146	52.235259	132.38598
16	12.514267	22.334390	45.797192	108.64531
17	12.132019	20.887607	40.915497	91.698935
18	11.823883	19.722789	37.115907	79.165126
19	11.573577	18.770360	34.093690	69.620176
20	11.369162	17.981421	31.645544	62.171984
21	11.201701	17.320699	29.631438	56.238971
22	11.064381	16.762177	27.952234	51.428997
23	10.951919	16.286283	26.536051	47.469861
24	10.860167	15.878035	25.329666	44.167782
25	10.785818	15.525790	24.292944	41.381717
26	10.726211	15.220373	23.395111	39.006973
27	10.679181	14.954462	22.612229	36.964477
28	10.642950	14.722154	21.925422	35.193561
29	10.616044	14.518634	21.319634	33.647023
30	10.597232	14.339943	20.782721	32.287668
31	10.585482	14.182799	20.304792	31.085845
32	10.579916	14.044455	19.877717	30.017667
33	10.579791	13.922602	19.494759	29.063704
34	10.584467	13.815280	19.150289	28.208011
35	10.593396	13.720820	18.839577	27.437396
36	10.606103	13.637789	18.558615	26.740860
37	10.622174	13.564954	18.303990	26.109171
38	10.641250	13.501245	18.072780	25.534527
39	10.663015	13.445731	17.862467	25.010296
40	10.687192	13.397599	17.670873	24.530809
41	10.713537	13.356135	17.496104	24.091191
42	10.741832	13.320711	17.336505	23.687235
43	10.771887	13.290770	17.190627	23.315287
44	10.803531	13.265820	17.057193	22.972165
45	10.836609	13.245421	16.935076	22.655083
46	10.870987	13.229183	16.823276	22.361592
47	10.906541	13.216754	16.720904	22.089534
48	10.943162	13.207819	16.627167	21.837000
49	10.980750	13.202097	16.541356	21.602294
50	11.019216	13.199331	16.462834	21.383906

Table AP-V : Values of $N_m(2p)$

m p	1	2	3	4
1	5.9937671	-	-	-
2	4.0668787	25.388848	-	-
3	3.8036566	10.733735	111.53052	-
4	3.7744891	8.0327134	33.608518	486.69676
5	3.8282347	6.9789396	20.480469	113.35747
6	3.9205355	6.4638932	15.477384	57.879120
7	4.0322344	6.1903803	12.947072	38.411860
8	4.1536961	6.0448087	11.467020	29.074994
9	4.2797371	5.9742794	10.522919	23.780132
10	4.4074630	5.9508685	9.8862942	20.447047
11	4.5352189	5.9585102	9.4410020	18.194926
12	4.6620474	5.9873603	9.1220915	16.593983
13	4.7873962	6.0310883	8.8905584	15.412127
14	4.9109539	6.0854647	8.7216496	14.514087
15	5.0325563	6.1475737	8.5989470	13.816190
16	5.1521295	6.2153529	8.5111607	13.264142
17	5.2696562	6.2873114	8.4502900	12.821307
18	5.3851541	6.3623516	8.4105192	12.462138
19	5.4986628	6.4396527	8.3875273	12.168323
20	5.6102348	6.5185930	8.3780431	11.926418
21	5.7199300	6.5986959	8.3795484	11.726346
22	5.8278120	6.6795928	8.3900771	11.560418
23	5.9339457	6.7609963	8.4080735	11.422671
24	6.0383956	6.8426808	8.4322930	11.308416
25	6.1412253	6.9244685	8.4617292	11.213919
26	6.2424962	7.0062182	8.4955611	11.136170
27	6.3422674	7.0878182	8.5331131	11.072720
28	6.4405958	7.1691793	8.5738251	11.021558
29	6.5375355	7.2502310	8.6172294	10.981017
30	6.6331381	7.3309170	8.6629333	10.949705
31	6.7274528	7.4111930	8.7106049	10.926452
32	6.8205261	7.4910241	8.7599623	10.910266
33	6.9124023	7.5703833	8.8107648	10.900305
34	7.0031236	7.6492496	8.8628062	10.895844
35	7.0927298	7.7276075	8.9159090	10.896263
36	7.1812587	7.8054455	8.9699197	10.901022
37	7.2687464	7.8827556	9.0247052	10.909655
38	7.3552271	7.9595327	9.0801499	10.921753
39	7.4407331	8.0357741	9.1361528	10.936957
40	7.5252955	8.1114789	9.1926256	10.954955
41	7.6089435	8.1866478	9.2494908	10.975468
42	7.6917052	8.2612829	9.3066804	10.998251
43	7.7736073	8.3353874	9.3641345	11.023086
44	7.8546750	8.0489653	9.4218000	11.049777
45	7.9349327	8.4820213	9.4796304	11.078153
46	8.0144035	8.5545607	9.5375841	11.108057
47	8.0931094	8.6265892	9.5956244	11.139351
48	8.1710717	8.6981129	9.6537189	11.171908
49	8.2483104	8.7691383	9.7118386	11.205616
50	8.3248449	8.8396720	9.7699578	11.240372

Table AP-V : Values of $N_m(2p)$ (continued)

m	5	6	7	8
p				
5	2102.3544	-	-	-
6	398.28563	8999.5604	-	-
7	174.53673	1435.5827	38236.779	-
8	102.91233	550.32429	5264.9805	161461.47
9	70.867697	291.43159	1792.5214	19552.206
10	53.636458	183.70287	860.66613	5984.7415
11	43.221713	129.09479	499.58665	2626.7294
12	36.397896	97.654760	327.19911	1411.8412
13	31.656067	77.869091	232.87672	865.00224
14	28.210889	64.574614	176.05489	580.69030
15	25.619289	55.182920	139.28851	416.88964
16	23.614981	48.281689	114.15301	314.98496
17	22.029565	43.047217	96.203858	247.69855
18	20.751990	38.972527	82.926624	201.11392
19	19.706414	35.731426	72.816049	167.59491
20	18.839470	33.106073	64.927862	142.69602
21	18.112641	30.946312	58.645964	123.69924
22	17.497498	29.145784	53.554692	108.87271
23	16.972648	27.627345	49.365398	97.073311
24	16.521712	26.333870	45.872543	87.523269
25	16.131961	25.222272	42.926505	79.679145
26	15.793363	24.259519	40.416223	73.152296
27	15.497913	23.419916	38.257813	67.658992
28	15.239157	22.683208	36.386929	62.988249
29	15.011834	22.033240	34.753512	58.980572
30	14.811617	21.456984	33.318124	55.513588
31	14.634920	20.943833	32.049334	52.492136
32	14.478744	20.485070	30.921827	49.841302
33	14.340564	20.073475	29.915018	47.501453
34	14.218244	19.703018	29.012018	45.424631
35	14.109959	19.368630	28.198859	43.571903
36	14.014148	19.066020	27.463899	41.911387
37	13.929463	18.791535	26.797367	40.416764
38	13.854738	18.542048	26.191010	39.066148
39	13.788959	18.314864	25.637816	37.841211
40	13.731238	18.107655	25.131790	36.726506
41	13.680796	17.918395	24.667782	35.708935
42	13.636950	17.745316	24.241344	34.777329
43	13.599093	17.586870	23.848620	33.922115
44	13.566688	17.441691	23.486247	33.135045
45	13.539257	17.308577	23.151285	32.408983
46	13.516373	17.186460	22.841152	31.737722
47	13.497654	17.074390	22.553569	31.115847
48	13.482758	16.971523	22.286524	30.538611
49	13.471377	16.877101	22.038227	30.001839
50	13.463232	16.790445	21.807086	29.501845

APPENDIX VI

The Normal Component of the Incident Magnetic Field on the Sunlit Side of the Moon

Our aim is first to express the normal component of the incident magnetic field on the sunlit side in a Fourier series of the ϕ coordinate and then to truncate this series according to a criterion which permits us to estimate the resulting error.

From Equation (2.2.1), we can express this component as follows:

$$\vec{H}\cdot\vec{a}_r = [H_o(\sin\theta\sin\phi\cos\psi - \cos\theta\sin\psi) + H_{ox}\sin\theta\cos\phi]\,e^{i(k_{//}R_M\cos\theta + \alpha\sin\phi)}$$

where

$$\alpha = k_{\perp}R_M\sin\theta$$

If we use the following identities (see, for example, Morse et al, p. 620)

$$e^{i\alpha\sin\phi} = \sum_{m=-\infty}^{\infty} e^{im\phi}\, J_m(\alpha)$$

We can rewrite the above expression as follows:

$$\vec{H}\cdot\vec{a}_r = H_o\Big(\sum_{m=0,2,4..} a_m\cos m\phi + \sum_{m=1,3,5..} b_m\sin m\phi\Big)e^{ik_{//}R_M\cos\theta}$$

$$+ H_{ox}\Big(\sum_{m=1,3.5..} c_m\cos m\phi + \sum_{m=2,4,6..} d_m\sin m\phi\Big)e^{ik_{//}R_M\cos\theta}$$

where

$$a_m = -ib_m = i\cos\theta\cos\psi\frac{\varepsilon_m}{2}[J_{m+1}(\alpha)-J_{m-1}(\alpha)]$$

$$-\varepsilon_m\cos\theta\cos\psi J_m(\alpha)$$

$$c_m = -id_m = \sin\theta[J_{m-1}(\alpha) + J_{m+1}(\alpha)]$$

and ε_m is the Neumann factor [see Equation (2.4.1)].

The following rules were used to truncate this series:

1. The terms characterized by $m = 1$ are always kept and if $H_o \neq 0$, the term $m = 0$ is also kept.

2. At a given frequency, we keep all the terms in the summation specified by a value of m such that

$$\frac{X^{m-1}}{(m-1)!} > 0.01$$

where

$$X = \frac{k_\perp R_M}{2}$$

It should be pointed out that in this work the parameters of the source were restricted to the following values: $V_{SW} \geq 200$ km/sec and $\psi \leq 60°$. Moreover, since the frequencies of interest are smaller than 0.04 Hz we obtain $X \leq 1.9 \equiv \mu$. This value of μ insures that the maximum value of m that can be kept in the summation is $m = 8$, and also that if an harmonic specified by m $(m > 1)$ is kept then the harmonic specified by m-1 is also kept.

Our criterion also permits us to establish an upper bound of a few percent on the relative mean square error resulting from the truncation. In order to show this, we first establish two useful inequalities:

1. Let M be the smallest value of m $(9 \geq m \geq 2)$ for which

$$\frac{X^{M-1}}{(M-1)!} \leq 0.01$$

Then

$$\frac{X}{M} \leq 0.235 \equiv \sigma$$

This result is established by evaluating $\frac{[0.01(M-1)!]^{1/(M-1)}}{M}$ for M = 2 to 9. We find that the maximum value of this quantity is reached for M = 9 and is given by the value of σ above.

2. From an inequality satisfied by cylindrical Bessel function (see Watson, 1966, p. 16) we have

$$J_{m-1}(\alpha) \leq \frac{(\alpha/2)^{m-1}}{(m-1)!} e^{\alpha^2/4m}$$

If $\alpha = 2X\sin\theta$ and $m = M + n$ (where M and X are defined above), we obtain

$$J_{m-1}(\alpha) \leq \frac{X^{M-1}}{(M-1)!} \sigma^n e^{\mu\sigma} = 0.016 \sigma^n$$

If we assume that $H_o = 0$ and used the above inequalities, the relative root mean square error can be bounded as follows:

$$\frac{1}{\sin\theta}\Big[\sum_{m=M}^{\infty}(c_m^2+d_m^2)\Big]^{1/2} = \Big[\sum_{m=M}^{\infty}\{J_{m-1}(\alpha)+J_{m+1}(\alpha)\}\Big]^{1/2}$$

$$\leq 0.016\Big[\sum_{n=0}^{\infty}(\sigma^{n}+\sigma^{n+2})^{2}\Big]^{1/2} = 0.016\,\frac{(1+\sigma^2)}{(1-\sigma^2)^{1/2}}$$

$$\simeq 0.017$$

So the truncation involves a relative error generally less than 2%. The same result can be obtained when $H_{ox} \neq 0$.

The above criteria were also used to truncate the representation of the field inside the moon and in the cylindrical void. The truncation errors in our calculation were of the same order as those derived above. A typical result is illustrated in Figure AP-VI. This is a plot of the absolute value of the partial field associated with each harmonic (m = 1 - 6) of the normal component of the poloidal H magnetic field at the lunar surface. The parameters of the source are $H_o = 0$, $H_{ox} = 1$, $\psi = 60°$, $V_{SW} = 300$ km/sec and the frequency is 0.04 Hz. In this case, our criteria require that only the harmonic m = 1 to 6 be kept in the summation. Actual calculation of the term m = 7 reveals that its inclusion would modify the total field by no more than 0.5%.

For given parameters of the source, the number of harmonics kept in our representation will depend on the frequency. An example of this is shown in Table AP-VI, where the source used was the same as the one discussed above.

Table AP-VI

Fourier Harmonic

Frequency (Hertz)	Number of Harmonics
0.0002	1
0.0005	2
0.005	3
0.02	4
0.04	6

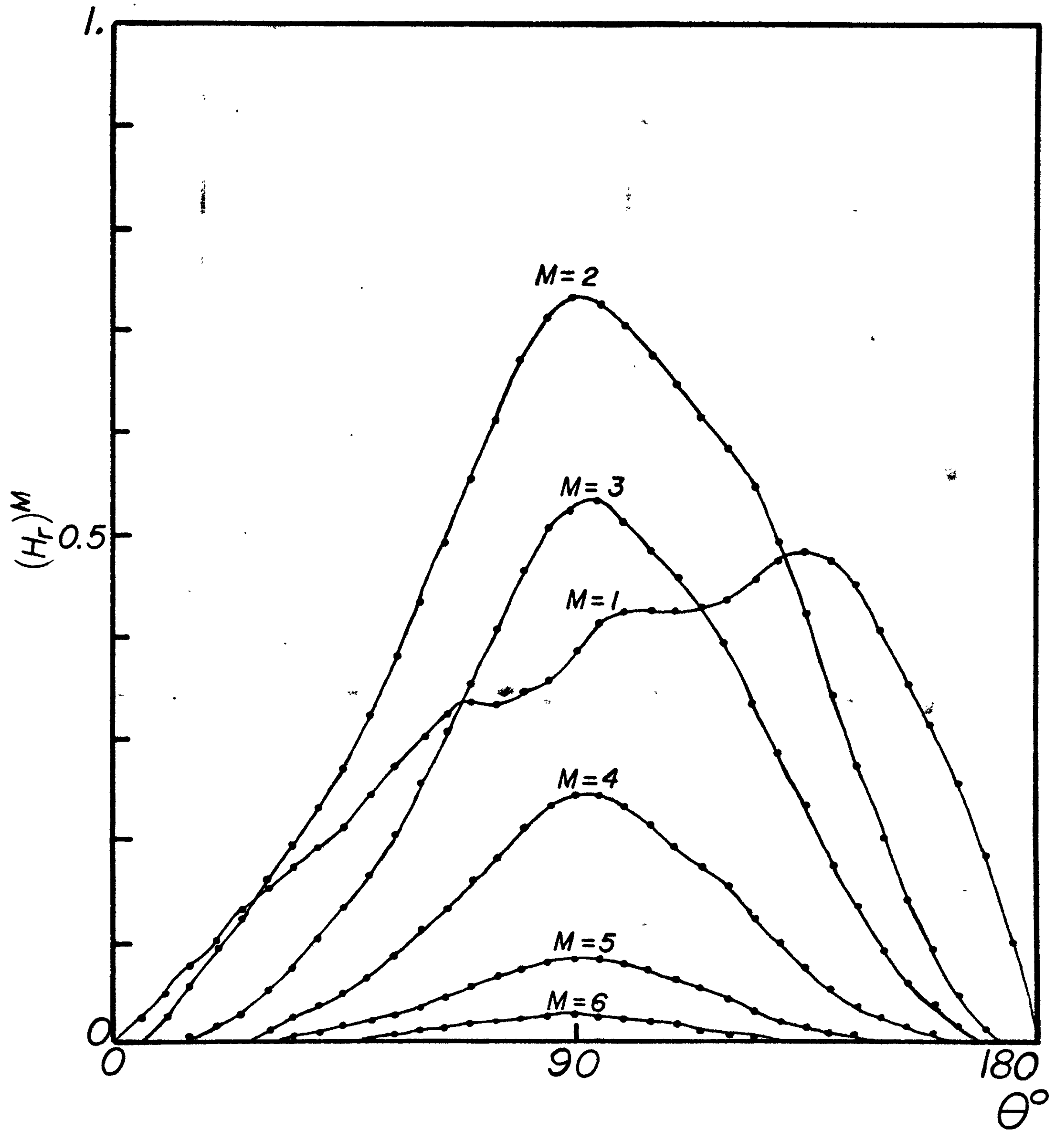

Figure AP-VI

Absolute value of the partial field associated with each Fourier Harmonic of the radial component of the magnetic field vs. Polar Angle, for m = 1, 6.

References

Barnes, A., Cassen, P., Mihalov, J.D. and Eviatar , A., "Permanent Lunar Surface Magnetism and its Deflection of the Solar Wind", *Science*, *172*, 716,1971.

Behannon, K. W., "Intrinsic Magnetic Properties of the Lunar Body", *J. Geophys. Res.*, *73*, 7257, 1968.

Belcher, J. W. and Davis, L., "Large Amplitude Alfven Waves in the Interplanetary Medium", *J. Geophys. Res.*, *76*, 3534, 1971.

Blank, J. L. and Sill, W. R., "Response of the Moon to the Time Varying Interplanetary Magnetic Field", *J. Geophys. Res.*, *74*, 736, 1969.

Brace, W. F., "Resistivity of Saturated Crustal Rocks to 40 km Based on Laboratory Measurements", *Geophys. Monogr. Ser.*, *AGU*, *14*, 243, 1971.

Burlaga, L. F., "Discontinuities and Shock Waves in the Interplanetary Medium and their Interaction with the Magnetosphere", *Solar-Terrestrial Phys.*/1970 (Dyer, Ed.), D. Reidel Publ. Co, II, 135, 1972.

Cassen, P. and Reynolds, R. T., "Convection in the Moon: Effect of Variable Viscosity", *J. Geophys. Res.*, *79*, 2937, 1974.

Chao, J.K., "Interplanetary Collisionless Shock Waves", M.I.T. Center for Space Res., CSR-TR-70-3.

Charles, R. W., Hewitt, D.A., and Wones, D. R., "H_2O in Lunar Processes", Proc. Second Lunar Conf., (Levinson, Ed.), M.I.T. Press, *1*, 645, 1971.

Coleman, P. J., Lichtenstein, B. R., Russel C. T., Sharp, L. R. and Shubert, G., "Magnetic Field near the Moon", Proc. Third Lunar Science Conf., M.I.T. Press, *3*, 2271, 1972.

Colburn, D. S., Currie, R. G., Mihalov, J. D. and Sonett, C.P., "Diamagnetic Solar Wind Cavity Discovered Behind the Moon", *Science*, *158*, 1040, 1967.

Cooke , J.C., "Some Relations Between Bessel and Legendre Functions", *Monatshefte Fur Math.*, *60*, 322, 1956.

Cooke, J.C., "On Potential Problem Involving Spheroids Inside a Cylinder", Z. Angew. Math. Mech., 42 305,1962.

Daily, W.D., "Alfven Wave Refraction by Interplanetary Inhomogeneities", J. Geophys. Res., 78, 2043, 1973.

Dolginov, Sh. Sh., Yeroshenko, Ye. G., Zhuzgov, L. N. and Pushkov, N. V., "Investigation of the Magnetic Field of the Moon", Geomagnetism and Aero., 1, 18, 1961.

Dolginov, Sh. Sh., Yeroshenko, Ye. G., Zhuzgov, L. N. and Pushkov, N.V., "Measurement of the Magnetic Field near the Moon by the Luna 10 Orbiter", Dokl. Akad. Nauk., USSR, 170, 18, 1966.

Dolginov, Sh. Sh., Yeroshenko, Ye. G., Zhuzgov, L. N. and Pushkov, N.V., "Possible Interpretation of the Results of Measurement on the Lunar Orbiter Luna 10", Geomagnetism and Aero., 1, 352, 1967.

Duba, A., "Electrical Conductivity of Olivine", J. Geophys. Res., 74,2483, 1972a.

Duba, A. Heard, H. C., and Schock, R. N., "The Lunar Temperature Profile", Earth and Planetary Sciences Letter, 15, 301, 1972b.

Duba, A. and Ringwood, A. E., "Electrical Conductivity, Internal Temperature and Thermal Evolution of the Moon", The Moon, 7, 356, 1973.

Dyal, P., Parkin, C. W., Cassen, P., "Surface Magnetometer Experiment: Internal Properties and Lunar Field Interaction with the Solar Plasma", Proc. Third Lunar Science Conf., M.I.T. Press, 3, 2287, 1972.

Dyal, P., Parkin, C. W. and Daily, W. D., "Surface Magnetometer Experiment: Internal Lunar Conductivity and Steady Field Measurements", Proc. Fourth Lunar Science Conf., M.I.T. Press, 3, 205, 1973a.

Dyal, P. and Parkin, C.W., "Global Electromagnetic Induction in the Moon and Planets", Phys. Earth and Plan. Int., 7, 251, 1973b.

England, A. W., Simmons, G. and Strangway, D., "Electrical Conductivity of the Moon", *J. Geophys. Res.*, *73*, 3219, 1986.

Fensler, W. E., Knott, E. F., Olte, A. and Siegel, K. M., "The Electromagnetic Parameters of Selected Terrestrial and Extraterrestrial Rocks and Glasses", Symp. #14 of the Int. Astro. Union (Kopal and Mihailov Ed.), Academic Press, 545, 1962.

Fricker, P. E., Reynolds, R. T. and Summers, A. L., "On the Thermal History of the Moon", *J. Geophys. Res.*, *72* , 2649, 1967.

Fuller, M., "Lunar Magnetism", *Rev. Geophys. and Space Physics*, *12*, 23, 1974.

Hobbs, B. A., "The Inverse Problem of the Moon's Electrical Conductivity", *Earth Plan. Science Lett.*, *17*, 380, 1973.

Hollweg, J. V., "Interaction of the Solar Wind with the Moon and the Formation of a Lunar Limb Shock Wave", *J. Geophys. Res.*, *73*, 7269, 1968.

Gold, T., "The Magnetosphere of the Moon", in *The Solar Wind* (Mackin and Neugebauer, Ed.), Pergamon Press, New York, 381, 1966.

Golub, G., "Numerical Methods for Solving Linear Least Square Problems", *Numerische Math.*, *7*, 206, 1965.

Krall, N. A. and Tidman, D. A., "Magnetic Fluctuation near the Moon", *J. Geophys. Res.*, *74*, 6439, 1969.

Kuckes, A. F., "Lunar Electrical Conductivity", *Nature*, *232*, 249, 1971.

Kuckes, A. F., paper submitted to *J. Geophys. Res.*, 1974.

Lanczos, C., *Linear Differential Operator*, Van Nostrand, 1961.

Lichtenstein, B. R., Russel, C. T., Coleman, P. J. and Schubert, G., "On the Occurrence of Compressional Disturbances over the Lunar Limbs", Abstract, 55th Annual Meeting, A.G.U., 1974.

Madden, T. R., "The Resolving Power of Geoelectric Measurement for Delineating Zones within the Crust", Geophys. Monogr. Ser., AGU, 14, 95, 1971.

Miles, P. A., Westphal, W. B. and von Hippel,A., "Dielectric Spectroscopy of Ferromagnetic Semiconductor", Rev. Mod. Phys., 29, 279, 1957.

Millar, R. F., "The Rayleigh Hypothesis and a Related Least-Square Solution to Scattering Problems for Periodic Surface and other Scatterers", Radio Science, 8, 785, 1973.

Morin, F. J., "Electrical Conductivity of Fe_2O_3 and Fe_2O_3 Containing Titanium", Phys. Rev., 83, 1005, 1951.

Morse, P. M. and Feshbach, H., Methods of Theoritical Physics, Mcgraw-Hill, 1953.

Müller, C., Foundation of the Mathematical Theory of Electromagnetic Waves, Springer-Verlag, 1969.

Ness, N. F., Behannon, K. W., Scearce, C. S. and Cantarano, S. C., "Early Result from the Magnetic Field Experiment on Explorer 35", J. Geophys. Res., 72, 5769, 1967.

Ness, N. F., Behannon, K. W., Taylor, H. E. and Whang, Y. C., "Pertubation of the Interplanetary Magnetic Field by the Lunar Wake", J. Geophys. Res., 73, 3421, 1968.

Ness, N. F. and Schatten, K. H., "Detection of Interplanetary Magnetic Field Fluctuation Stimulated by the Lunar Wake", J. Geophys. Res., 74, 6425, 1969.

Ness, N. F., "Interaction of the Solar Wind with the Moon", Solar Terrestrial Physics, (Dyer, Ed.), D. Reidel Publ. Co., II, 159, 1970.

Olver, F. W., "Bessel Functions of Integer Order", Handbook of Mathematical Functions, (Abramowitz and Segun, Ed.), Dover, 355, 1965.

Ogilvie, K. W. and Ness, N. F., "Dependence of the Lunar Wake on Solar Wind Plasma Characteristics", J. Geophys. Res., 74, 4123, 1969.

Parkin, C. W., Dyal, P. and Daily, W. D., "Magneto Permeability and Iron Abundance of the Moon from Magnetometer Measurements", Fourth Lunar Science Conf. (Chamberlain and Watkins, Ed.) 584, 1973.

Phillips, R. J., "The Lunar Conductivity Profile and the Nonuniqueness of Electromagnetic Data Inversion", Icarus, 17, 88, 1972.

Ringwood, A. E. and Essene, E., "Petrogenesis of Apollo 11 Basalts, Internal Constitution and Origin of the Moon", Geochem. Cosmochem. Acta 34, Suppl. 1, 769, 1970.

Royal Society Mathematical Tables, Bessel Function, 7, (Olver, Ed.), Cambridge Univ. Press, 1960.

Russel, C. T., Coleman, P. J., Lichtenstein, B. R., Schubert, G. and Sharp, L. R., "Apollo 15 and 16 Subsatellite Measurement of Lunar Magnetic Field", Fourth Lunar Science Conf., (Chamberlain and Watkins, Ed.), 645, 1973.

Sari, J. W. and Ness, N. F., "Power Spectra of the Interplanetary Magnetic Field", Solar Phys., 8, 155, 1969.

Schatten, K., "Large Scale Properties of the Interplanetary Magnetic Field", Rev. Geophys., 9, 773, 1971.

Schubert, G. and Schwartz, R., "A Theory for the Interpretation of Lunar Surface Magnetometer Data", The Moon, 1, 106, 1969.

Schubert, G., Colburn, D. S., "Thin Highly Conducting Layer in the Moon: Consistent Interpretation of Dayside and Nightside Electromagnetic Responses", J. Geophys. Res. 76, 8174, 1971.

Schubert, G. and Schwartz, K., "High Frequency Electromagnetic Response of the Moon", J. Geophys. Res., 77, 76, 1972.

Schubert, G., Smith, B. F., Sonett, C. P., Colburn, D. S. and Schwartz, K., "Nightside Electromagnetic Response of the Moon", J. Geophys. Res., 78, 3688, 1973a.

Schubert, G., Sonett, C. P., Schwartz, K. and Lee, H. J., "The Induced Magnetosphere of the Moon, 1. Theory", J. Geophys. Res.,78, 2094, 1973b.

Schubert, G., Schwartz, K., Sonett, C. P., Colburn, D. S. and Smith, B. F., "Lunar Electromagnetic Scattering: 2. Magnetic Fields and Transfer Functions for Parallel Propagation", Geochem. Cosmochem. Acta, 37, Suppl 4, 2907, 1973c.

Schubert, G., Lichtenstein , B. R., Coleman, P. J. and Russel, C. T., "Simultaneous Explorer 35 and Apollo 15 Orbital Magnetometer Observation; Implication for Lunar Conductivity Inversion", J. Geophys. Res., 79, 2007, 1974a.

Schubert, G., Lichtenstein, B. R., Russel, C. T., Coleman, P. J., Smith, B. F., Colburn, D. S. and Sonett, C. P., "Lunar Dayside Plasma Sheet Depletion: Inference from Magnetic Observations", Geophys. Res. Lett., 1, 97, 1974b.

Schubert, G., Smith, B. F., Sonett, C. P., Colburn, P. S., and Schwartz, K., "Polarized Magnetic Field Fluctuation at the Apollo 15 Site: Possible Regional Influence on Lunar Induction", Science, 183, 1184, 1974c.

Schwartz, K., Sonett, C. P. and Colburn, D. S., "Unipolar Induction in the Moon and a Lunar Shock Mechanism", The Moon, 1, 7, 1969.

Schwartz, K. and Schubert, G., "Time-dependent Lunar Electric and Magnetic Field Induced by a Spacially-Varying Interplanetary Magnetic Field", J. Geophys. Res., 74, 4777, 1969.

Schwartz, K. and Schubert, G., "Lunar Scattering, 1. Propagation Parallel to the Diamagnetic Cavity Axis", J. Geophys. Res., 74, 6496, 1973.

Schwerer, F. C., Nagata, T. and Fisher, R. M., "Electrical Conductivity of Lunar Surface Rock and Chondritic Meteorites", The Moon, 2, 408, 1971.

Schwerer, F. C., Huffman, G. P., Fisher, R. M. and Nagata, T., "Electrical Conductivity of Lunar Surface Rocks at Elevated Temperature", Fourth Lunar Sci. Conf., 663, 1973.

Sill, W. R. and Blank, J. L., "Method for Estimating the Electrical Conductivity of the Lunar Interior", J. Geophys. Res., 75, 201, 1970.

Siscoe, G. L., Lyon, E. F., Binsack, J. H. and Bridge, H. S., "Experimental Evidence for the Detached Lunar Compression Wave", J. Geophys. Res., 74, 59, 1969.

Siscoe, G. L. and Goldstein, B., "Solar Wind Interaction with Lunar Magnetic Field", J. Geophys. Res., 78, 6741, 1973.

Smith, B. F., Colburn, D. S., Schubert, G., Schwartz, K. and Sonett, C. P., "The Induced Magnetosphere of the Moon, 2. Experimental Results from Apollo 12 and Explorer 35", J. Geophys. Res., 78, 5437, 1973.

Smith, B. F., Schubert, G., Colburn, D. S., Sonett, C. P. and Schwartz, K., "Corroborative Apollo 15 and 12 Lunar Surface Magnetometer Measurement", Abstract, Fourth Lunar Science Conf., (Chamberlain and Watkins, Ed.), 683, 1973.

Smythe, W. R., "Charged Spheroid in a Cylinder", J. Math. Physics, 4, 833, 1963.

Smythe, W. R., "Flow Around a Spheroid in a Circular Tube", Phys. of Fluids, 7, 633, 1964.

Smythe, W. R., "Static and Dynamic Electricity", Third Ed., McGraw-Hill, 1968.

Solomon, S. C. and Toksöz, M. N., "Internal Constitution and Evolution of the Moon", Phys. Earth and Planetary Interiors, 7, 15, 1973.

Sonett, C. P. and Colburn, D. S., "Establishment of a Lunar Unipolar Generator and Associated Shock and Wake by Solar Wind", Nature, 216, 340, 1967.

Sonett, C. P., Dyal, P., Parkin, C. W., Colburn, D. S., Mihalov, J. D. and Smith, B. F., "Whole Body Response of the Moon to Electromagnetic Induction in the Solar Wind", Science, 172, 256, 1971a.

Sonett, C. P., Schubert, G., Smith, B. F., Schwartz, K. and Colburn, D. S., "Lunar Electrical Conductivity from Apollo 12 Magnetometer Measurements: Composition and Thermal Inference", Proc. Second Lunar Science Conf., (M.I.T. Press), 3, 2415, 1971b.

Sonett, C. P., Colburn, D. S., Dyal, P., Parkin, C. W., Smith, B. F., Schubert, G. and Schwartz, K., "Lunar Electrical Conductivity Profile", Nature, 30, 359, 1971c.

Sonett, C. P., Mihalov, J. D. and Ness, N. F., "Concerning the Electrical Conductivity of the Moon", J. Geophys. Res., 76, 5172, 1971d.

Sonett, C. P., Smith, B. F., Colburn, D. S., Schubert, G. and Schwartz, K., "The Induced Magnetic Field of the Moon: Conductivity Profiles and Inferred Temperature", Proc. Third Lunar Science Conf., (M.I.T. Press), 3, 2309, 1972.

Sonett, C. P., "Solar Wind Induction and Lunar Conductivity". To appear in Phys. Earth and Plan. Int., 1974.

Spreiter, J. R., Marsh, M. C. and Summers, A. L., "Hydromagnetic Aspect of the Solar Wind Flow Past the Moon", Cosmic Electrodynamics, 1, 5, 1970.

Strangway, D. W., "Moon: Electrical Properties of the Uppermost Layers", Science, 165, 1012, 1969.

Stratton, J., "Electromagnetic Theory", McGraw-Hill, 1941.

Taylor, H. E., Behannon, K. W. and Ness, N. F., "Measurement of the Perturbed Interplanetary Magnetic Field in the Lunar Wake", J. Geophys. Res., 73, 6723, 1968.

Toksöz, M. N., Solomon, S. C., Minear, J. W. and Johnston, D. H., "Thermal Evolution of the Moon", The Moon, 4, 190, 1972.

Tolland, H. G., "Electrical Properties of a Synthetic Lunar Pyroxenite and the Internal Temperature of the Moon", Phys. Earth and Plan. Int., 8, 292, 1974.

Tozer, D. C. and Wilson, J., III, "The Electrical Conductivity of the Moon", Proc. Roy. Soc, London, Ser. A, 296, 320, 1967.

Tozer, D. C., " The Moon's Thermal State and an Interpretation of the Lunar Electrical Conductivity Distribution", The Moon, 5, 90, 1972.

Turcotte, D. L., Hsui, A. T. and Torrance, K. E., "Thermal Structure of the Moon", J. Geophys. Res., 74, 6931, 1972.

Urey, H. C., "Origin and History of the Moon", Physics and Astronomy of the Moon (Kopal, Ed.), 481, 1962.

Ward, S. H., "Gross Estimate of the Conductivity, Dielectric Constant and Magnetic Permeability Distribution in the Moon", Radio Science, 4, 117, 1969.

Watson, G. N., "The Use of a Series of Bessel Functions in Problems Connected with a Cylindrical Wind-Tunnel", Proc. Roy. Soc. London, A130, 29, 1930.

Watson, G. N., "Theory of Bessel Functions", 2nd Ed., Cambridge University Press, 1966.

Weertman, J., "The Creep Strength of the Earth's Mantle" Rev. Geophys. and Space. Phys., 8, 145, 1970.

Whang, Y. C., "Field and Plasma in the Lunar Wake", Phys. Rev., 186, 143, 1969.

Whang, Y. C. and Ness, N.F., "Observation and Interpretation of Lunar Mach Cone", J. Geophys. Res., 75, 6002, 1970.

Wiggins, R. A., "The General Linear Inverse Problem Rev. Geophys. and Space Phys., 10, 251, 1972.

Willis, D. M., "Structure of the Magnetopause", Rev. Geophys., 9, 953, 1971.

Biographical Note

Donald Lucien Leavy was born on April 7, 1947, in Montreal, Canada. His undergraduate work was done at the University of Montreal where he majored in Physics and received a B. Sc. in 1968. He held research positions in geophysics in the industry and in the government during three summer recess periods. He joined the graduate school at M.I.T., where he received an M.Sc. degree from the Department of Earth and Planetary Sciences in 1972. The title of his Master's thesis was, "Scattering of Elastic Waves Around a Compressional Source". He has one publication to his credit:

Donald Leavy and Theodore Madden, "Lunar Electrical Conductivity", Nature 250, 553-555, 1974.